# Modelling the transport and dispersion of volcanic co-PDC ash clouds using NAME: an evaluation of source geometry and mass eruption rate

**M. Hagenbourger[1*], F. M. Beckett[2], T. J. Jones[1], S. L. Engwell[3]**

[1]Lancaster Environment Centre, Lancaster University, Lancaster, United Kingdom

[2]Met Office, Exeter, United Kingdom

[3]British Geological Survey, The Lyell Centre, Edinburgh, United Kingdom

*Corresponding author: Marie Hagenbourger, email: m.hagenbourger@lancaster.ac.uk

**Key Points:**

- We explored the range of source parameters suitable for a co-PDC plume and the sensitivity of transport and dispersion model simulations.
- Variations in the source geometry (area and aspect ratio) have negligible effects on ash transport, dispersion, and mass in the atmosphere.
- Ash cloud simulation results are sensitive to the co-PDC plume height and associated mass eruption rate.

## Abstract

Pyroclastic density currents (PDCs) are gravity currents that frequently form during explosive volcanic eruptions. These ground-hugging density currents consist of high-temperature mixtures of pyroclasts (e.g., ash, pumice), lithics, and gas. They have the potential to generate co-PDC plumes, which detach from the underlying PDC as they buoyantly rise into the atmosphere. Co-PDC plumes, composed of fine-grained ash particles and hot gas, can reach heights of tens of kilometres, potentially dispersing large volumes of ash over continental scale areas, impacting the environment, and posing a risk to aviation. Owing to their formation mechanism co-PDCs have unique characteristics, such as fine particle sizes (e.g., < 90 μm) and a high-aspect ratio, irregular-shaped, source geometry. Here, we consider how the release of ash into the atmosphere from a co-PDC plume may differ to that from a typical Plinian eruption column, and the implications for operational modelling of the resulting ash cloud for the provision of advice to the aviation industry. We use the atmospheric dispersion model, NAME, which is used by the London Volcanic Ash Advisory Centre. We performed a sensitivity analysis to determine which co-PDC source parameters are important for modelling the associated ash clouds. We show that variations in the source geometry, i.e., the total area and aspect ratio, have a minor impact after the first ~ 6 hours in the atmosphere.



## Plain language summary

During volcanic eruptions, fast-moving mixtures of hot gas and rock, called pyroclastic density currents (PDCs), can separate into a ground hugging dense current and a buoyant plume that rises into the atmosphere, potentially reaching heights of tens of kilometres. These plumes are called co-PDC plumes. Relative to typical, vent-derived, volcanic ash plumes, they have finer-grained particles and are sourced from irregularly shaped ground regions. Our study applied and analysed a selection of co-PDC source parameters (e.g., source area) to the atmospheric dispersion model, NAME, used by the London Volcanic Ash Advisory Centre. Changes in the source geometry, i.e. the ground shape and the area from where ash particles lift off, only show minor influences on the ash cloud shape, transport and dispersion, and mass of ash in the atmosphere. However, changes in the plume height and the rate at which ash particles are released into the atmosphere highly impact the ash cloud location, its areal coverage, and the mass of ash in the atmosphere. This improved understanding of input parameter importance could be used for future model forecasting of co-PDC ash dispersal.

## 1 Introduction

Pyroclastic density currents (PDCs) are ground-hugging gravity currents that can occur during an explosive volcanic eruption through eruption column collapse (R. J. Brown & Andrews, 2015; Dellino et al., 2021; Druitt, 1998; Dufek et al., 2015; Giordano & Cas, 2021; T. J. Jones et al., 2023; Lube et al., 2020) or from the collapse of lava dome or flow fronts (Bonadonna, Mayberry, et al., 2002; Calder et al., 1997; Charbonnier & Gertisser, 2008; Michol et al., 2008; Sigurdsson & Carey, 1989; Sulpizio et al., 2010; Ui et al., 1999). They are a multi-phase mixture composed of hot gas and solid particles (e.g., lithics, pumice, ash) that propagate downslope with flow paths that are largely controlled by topography (Andrews & Manga, 2011, 2012; R. J. Brown & Andrews, 2015; Druitt, 1998; Dufek et al., 2015; T. J. Jones et al., 2023; Lube et al., 2020). All PDCs have the potential to generate co-PDC plumes, also known as co-ignimbrites or phoenix clouds (Andrews & Manga, 2011; Bursik & Woods, 1996; Engwell & Eychenne, 2016; Rosi et al., 2006; Sigurdsson & Carey, 1989; Sparks et al., 1997). These secondary plumes are composed of fine-grained particles and gas, which detach from the underlying PDC current by air intrusion and rise vertically by buoyancy (Andrews & Manga, 2011, 2012; Engwell & Eychenne, 2016; T. J. Jones et al., 2023; Sparks et al., 1997). Within the PDC, particle sedimentation acts to lower the current density, particularly in its uppermost regions, and when below ambient atmospheric density, a plume can form (Andrews & Manga, 2012; Engwell et al., 2016; Woods & Kienle, 1994). These co-PDC plumes rise in the atmosphere until reaching a level of neutral buoyancy and disperse laterally like umbrella clouds, however co-PDCs clouds are typically much smaller (Constantinescu et al., 2021; Mastin & Van Eaton, 2020; Prata et al., 2025; Zidikheri et al., 2017). In some cases, co-PDCs can become inverted downwind and descend to the ground (Engwell & Eychenne, 2016), thus increasing the ground area impacted by the co-PDC. In this contribution, we use the term ‘plume’ to refer to the near-source behaviour of the buoyant column, whereas the downwind transport and dispersion of ash is referred to as the ‘ash cloud’.

Co-PDC plumes and clouds have unique characteristics and are different to typical Plinian eruption columns and their associated ash clouds. For example, co-PDCs typically have a narrower particle size distribution and are composed of smaller particles (< 90μm) (Engwell

& Eychenne, 2016; Sigurdsson & Carey, 1989). This is because during co-PDC formation and plume lift-off, the coarser (heavier) particles remain in the underlying pyroclastic density current (Andrews & Manga, 2012; Woods & Kienle, 1994). Similarly, their componentry is mostly juvenile-rich (i.e., composed mainly of volcanic ash) as the denser accessory components such as lithics preferentially remain in the main current (Engwell & Eychenne, 2016; Sigurdsson & Carey, 1989). The plumes lift off from a source geometry that is of high aspect ratio (i.e., an irregular, elongated, rectangular ground footprint and not a circular vent). Furthermore, the source area is not necessarily at the eruption vent location as co-PDCs can be generated and lift-off from all parts of the associated PDC, including its entire length (Andrews & Manga, 2011; Engwell & Eychenne, 2016; Sparks et al., 1986, 1997).

Some numerical 1D models have previously been used to model co-PDC plume rise (Calder et al., 1997; Woods & Kienle, 1994; Woods & Wohletz, 1991) and they assume a thermal equilibrium between particles and gas and a well-mixed, homogenous suspension (Engwell et al., 2016; Woods & Wohletz, 1991). Specifically, Calder et al. (1997), Engwell et al. (2016), Sparks et al. (1997) and Woods & Wohletz (1991) adapted steady state column models commonly used for vent-derived plumes to simulate the formation of a co-PDC plume from an underlying pyroclastic density current. Other studies such as Woods & Kienle (1994) applied a thermal model to simulate small plumes rising as a discrete, buoyant thermal rise. Multidimensional models have also been applied to co-PDC plumes. Neri et al. (2002, 2003) mainly investigated the material properties and the multiphase nature of the flow and Herzog & Graf (2010) used a 3D model to highlight the limits of 1D models for co-PDC plumes. Additionally, Engwell et al. (2016) used work from Bursik (2001) and Bursik & Woods (1996) to couple PDC and plume models to understand co-PDC plume formation requirements and the plume heights they can achieve.

Co-PDCs can be generated during an explosive eruption and disperse large volumes of ash over great distances (Engwell & Eychenne, 2016), impacting the environment and potentially aviation (Engwell et al., 2016; Folch et al., 2012; Pardini et al., 2024; Webster et al., 2012; Witham et al., 2012). Despite global applicability and potential impact, relatively little modelling has been performed to consider the implications of source parameters characteristic of co-PDCs on the downwind location, extent and concentrations of ash in the atmosphere. The Numerical Atmospheric-Dispersion Modelling Environment (NAME) is used operationally by the London Volcanic Ash Advisory Centre (VAAC). Here, we perform

a set of NAME model runs to systematically evaluate the impact of co-PDC source geometry, the mass eruption rate, and the associated plume height on the modelled transport and dispersion of the volcanic ash cloud. This allows us to determine which co-PDC eruption source parameters are most important for modelling these ash clouds using NAME in an operational setting.

## 2 Methods

Ash dispersion and transportation modelling were performed using the UK Met Office's NAME model in its Lagrangian configuration. Specifically, here, version NAME III v8.5 was used (Beckett et al., 2020; A. Jones et al., 2007). NAME simulates the transport and dispersion of particles (e.g., particulate matter, volcanic ash, wind-spread diseases, radionuclides, and pollen) in the atmosphere. In NAME, a large number of modelled particles are released into a model environment where they are advected by three-dimensional wind fields, provided by a Numerical Weather Prediction (NWP) model, and dispersed using random walk techniques which account for subgrid turbulent motion in the atmosphere.

In this study, a fictitious volcanic co-PDC plume and its generated ash cloud were modelled. We assumed that a volcanic eruption produced a PDC and generated an associated co-PDC plume. Our model started at the lateral ash injection at the level of neutral buoyancy into the atmosphere and, using NAME, we modelled the transport and dispersion of the ash cloud generated by the co-PDC plume. To understand which eruption source parameters (ESPs) control the atmospheric transport and dispersion of co-PDC ash clouds, we performed 63 systematic NAME model runs (and 231 additional runs for the supplementary information). The particle characteristics, eruption location, eruption start time, duration, and the field proportions (i.e., horizontal grid resolution of 0.1° in Lat and Long) were all kept constant. The source geometry and, thus indirectly, its area and location, were systematically varied. The specific ESPs used are detailed in the following subsections. In all cases, we assumed time homogeneity, meaning that for each model run the parameters did not vary as a function of time (i.e., the source area was a constant value within each run). We assumed an even vertical distribution of particles at source and no plume overshoot height and thus a reduced complexity, compared to real events observed in nature, e.g. for Mount St. Helens on May 18$^{th}$ 1980 (Mastin et al., 2022; Sparks et al., 1986), where the plume height and mass

distribution varied during the eruption. In all runs, we also used the wet and dry deposition schemes in NAME to replicate removal of ash from the atmosphere; for further information, see Dacre et al. (2011), Harvey et al. (2018) and Webster et al. (2012).

### 2.1. Eruption Timing, Location and Meteorology Data

In this study, we use pre-processed global configured NWP data from the Met Office Unified Model (UM) (Beckett et al., 2020; A. Brown et al., 2012; Davies et al., 2005; Walters et al., 2019). In addition to the weather and turbulence, unresolved mesoscale motions, which are not resolved by the NWP model, are also represented (Webster et al., 2018). We used the global configuration of the UM, which used a standard latitude-longitude coordinate system and provided a global dataset with a horizontal resolution with grid lengths of approximately 10 km at mid-latitudes. The vertical resolution decreases with increased altitude, for example near ground level datasets are available at ~ 0.03 km intervals, whereas at a 30 km altitude this interval reduces to ~ 1.9 km. However, it is also worth noting that the atmosphere tends to be more stable at higher altitudes. These meteorological datasets include the wind speed and direction, temperature, pressure, clouds, precipitation, and the ground topography for each grid cell.

For this project, Hekla volcano in Iceland was selected as the source location; however, our study is not unique to Hekla as we investigate the ash cloud and NAME model sensitivity, and the focus is not on any specific local topographic effects or unique volcano properties. Hekla is situated at 63.98 °N, and 19.67 °W (Global Volcanism Program, 2024) in the south of Iceland, has a vent elevation of 1490 m (Global Volcanism Program, 2024), and is 51 km away from the Atlantic Ocean, thus no interaction with seawater was considered. The release of modelled ash at a given height in the atmosphere was initialised at 09:00 UTC on the 31$^{st}$ of January 2022 and particles were emitted for 1 hour. This start time/day was chosen as the wind fields were not extreme and, in general, travelled in an SE direction, towards Europe. Figure 1 shows the wind fields on 31$^{st}$ of January 2022 at 09:00 UTC (the start of ash release) and one hour after, at 10:00 UTC (the end of ash release). The wind fields at 0.01 km, above ground level (agl), and at 8.5 km agl show large differences, as displayed in Figure 1. Near the surface (0.01 km agl; Figs. 1 a & b), the wind over Iceland was slower than over the ocean. Over Hekla, wind speeds were very low, with a slight orientation towards NE and NW. The wind field at 0.01 km agl was clearly impacted by the ground topography and the

coastline. Whereas at higher elevation (8.5 km agl (Figs. 1 c & d) westerly winds were present over Hekla. Although we focus on this date (31st of January 2022), as detailed in Section 2.5.1, we also performed a series of supplementary model runs across the eight weather regimes for the North Atlantic and European region (Neal et al., 2016) to ensure that any results we present are not unique to a specific day/time. These additional meteorological conditions are fully presented in the supplementary information (Figures S17 to S58).

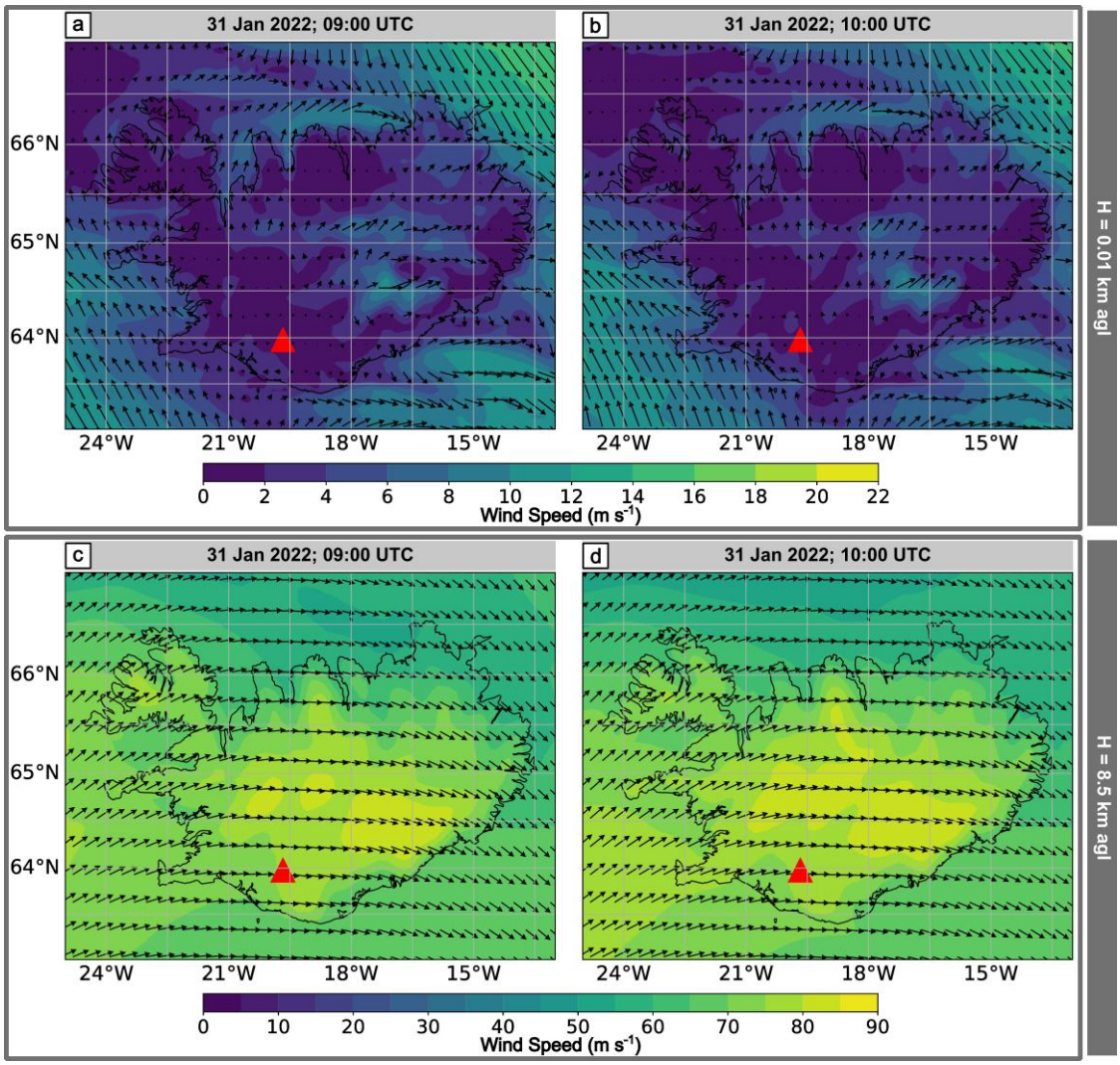


**Figure 1.** Meteorological data for Iceland on 31st of January 2022. The red triangle shows the location of Hekla, where the simulated co-PDC plume is sourced. The top two panels show the wind behaviour at 10 m agl elevation at times **(a)** 09:00 UTC, start of particle release and **(b)** 10:00 UTC, the end of particle release. The colour bar ranges between 0 and 22 m $s^{-1}$. The wind direction and speed were relatively constant over the two hours, although the field is impacted by topography and the coastline. The bottom two panels show the wind

195 field at 8.5 km agl elevation for **(c)** 09:00 UTC and **(d)** 10:00 UTC. Only every third arrow is
196 represented to facilitate a better overview. The colour bar ranges from 0 to 90 m $s^{-1}$, and the
197 wind field was relatively homogeneous.
198

199 **2.2. Source Geometry and Location**

200 As co-PDCs are derived from ground-hugging PDCs, the source of ash into the atmosphere
201 may not occur from the vent location. Here, the source was always positioned immediately to
202 the east of the volcanic vent in all runs, such that the meteorological conditions at the source
203 location remained constant between runs. The source geometry, in plan/map view, for the co-
204 PDC plumes simulated here has a rectangular shape with a width, *dx*, and length, *dy*, and
205 together these parameters define the source aspect ratio:

$$\alpha = \frac{dx}{dy} \qquad [1]$$

206

207 All PDCs have the potential to produce co-PDC plumes, which can lift off from the entire
208 underlying pyroclastic density current (Engwell & Eychenne, 2016; Sparks et al., 1997). To
209 bracket the range of co-PDC source areas likely in nature, we measured the source of the
210 largest and smallest well-documented co-PDCs. Specifically, the May 18$^{th}$, 1980 eruption of
211 Mount St. Helens (MSH) generated a large co-PDC with a lift-off from the entire blast area,
212 *A*, and the 1991 eruption of Unzen generated a relatively small co-PDC plume again, from
213 the entire PDC ground footprint (Engwell et al., 2016; Holasek & Self, 1995; Sparks et al.,
214 1986, 1997; Watanabe et al., 1999). These areas are shown in Figure 2. The area of the
215 blast/deposit and the area of the source geometry are highlighted in dark and light red,
216 respectively. Unzen had a total PDC deposit area of 0.4 $km^2$ and an aspect ratio of $\alpha$ = 0.2.
217 MSH had a blast/PDC deposit area of approximately 619 $km^2$ and an aspect ratio of $\alpha$ = 1.7.
218 The minimum (from Unzen) and maximum (from MSH) observed aspect ratios were used for
219 our numerical experiment as end-member parameters. The PDC flow/blast direction has been
220 defined as *dy*; therefore *dx* is perpendicular to the PDC flow direction. For each aspect ratio,
221 we varied the area logarithmically between the deposit area of Unzen and MSH.
222 The following describes how width and length are calculated using the area and
223 aspect ratio to initialise the model:

$$dx \cdot dy = A \qquad [2]$$

224

With Equation 1, *dx*: [3]

$$dx = \sqrt{A \cdot \alpha}$$

225

*dy* with Equation 1 becomes: [4]

$$dy = \sqrt{\frac{A}{\alpha}}$$

226

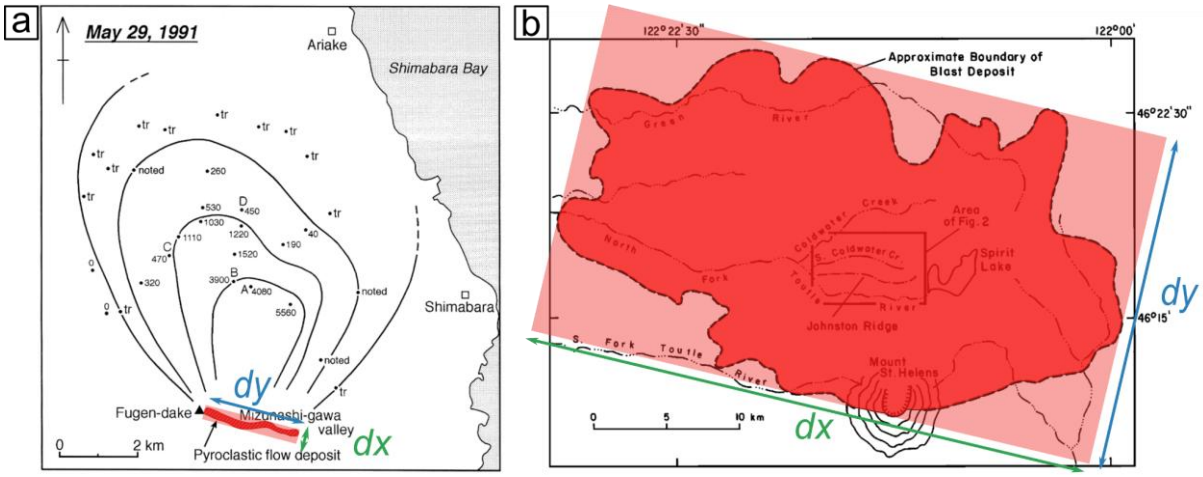


227

228 **Figure 2.** PDC deposit area shown in dark red for **(a)** the May 29th, 1991 eruption of Mount
229 Unzen, Japan and **(b)** the May 18th, 1980 eruption of Mount St. Helens, USA. Base maps
230 were taken from Watanabe et al. (1999) with permission from Elsevier and Fisher et al.
231 (1987) with permission from Wiley, respectively, and for (a) the associated co-PDC fallout is
232 shown by the isopach map. The numbers refer to a mass of ash in a unit area (g $m^{-2}$) where tr
233 = trace of ash-fall deposit. The aspect ratio defining the source geometry, i.e., the area of co-
234 PDC lift off, is highlighted in transparent, light red. The orientation of *dx* and *dy* was defined
235 by the volcano location (*dy* aligns with the PDC flow/blast direction; *dx* therefore is
236 perpendicular to the PDC flow direction).

237

238 **2.3. Eruption conditions**

239 To determine the maximum height of the co-PDC plumes, $H_T$, datasets from Aubry et al.
240 (2021), Eychenne & Engwell (2022), Mastin et al. (2009) and Pioli et al. (2019) were used
241 and are all reported in terms of the elevation above ground level (agl). The relationship
242 between the maximum plume height in km, $H_T$, and the mass eruption rate, MER, in g $h^{-1}$
243 follows an empirical power law (Aubry et al., 2023; Mastin et al., 2009; Morton et al., 1956;

Sparks, 1986; Wilson et al., 1978). The mass eruption rate, MER, also termed the source strength, describes the mass flux per total source area and is commonly derived from $H_T$ when atmospheric dispersion models, like NAME, are used operationally (Beckett et al., 2024). This is because the plume height is much easier to determine in real-time (e.g., radar, lidar measurements, or visual observation) compared to the MER (Dürig et al., 2018; Folch et al., 2012; Pioli & Harris, 2019). In this study, we used the following relationship based on Aubry et al. (2023), between $H_T$ and MER:

$$\mathrm{MER} = \sqrt[0.226]{\frac{H_T}{0.345}} \quad [5]$$

While the relationship of Aubry et al. (2023) has been defined predominantly using information from vent-derived plumes, due to a lack of erupted mass information for co-PDCs, the plume height and mass eruption rate from the MSH co-PDC plume fall within the confidence interval of the fit, and imply that, for at least the largest co-PDC events, this relationship is appropriate.

The ash plume spreads laterally at the neutral buoyancy level, where the density of the plume and the surrounding atmosphere are equal (Carey & Sparks, 1986). This constitutes the umbrella region of the plume and is characterised by a thickness, *dz*, which corresponds to the height interval of the ash release within the model (Fig. 3). The following equation by Carey & Sparks (1986), Morton et al. (1956) and Sparks (1986) describes the relationship between the thickness of the umbrella region and the total column height:

$$dz = H_T - H_B = x \cdot HT \quad [6]$$

Where $H_B$ is the base of the spreading cloud, and $x$ can take values in the range 0.25 to 3. Here, we use $x = 0.3$ due to the relationship $H_T = \frac{H_B}{0.7}$ provided by Bonadonna & Phillips (2003). This relationship holds true for all co-PDC plumes under the assumption of no umbrella overshoot.

For our model set up in NAME, we also define the mid-point, *z,* within the height interval of released ash. The relationships between $H_T$, $H_B$, *dz*, and *z* are shown visually in Figure 3 and are mathematically expressed as:

$$z = H_T - \frac{1}{2} \cdot dz \quad [7]$$

With substituting Equation 6 into Equation 7 we obtain the final expression for $z$:

$$z = 0.85 \cdot H_T \quad [8]$$

A full quantitative summary of the parameter ranges is presented in Table 1.

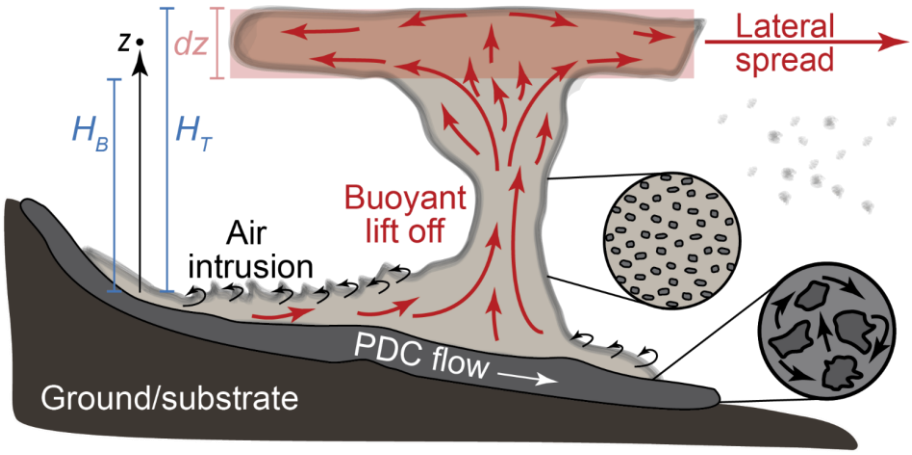


**Figure 3.** Characteristics of co-PDC plumes. Through air entrainment parts of the ground-hugging pyroclastic density current become buoyant, and a hot gas-ash mixture lifts off to form a co-PDC plume. The plume reaches a top height, $H_T$, and spreads laterally at the level of neutral buoyancy where the particles are dispersed over a vertical thickness, $dz$, (between $H_T$ and $H_B$; shaded in red) with a mid-point elevation, $z$.

**Table 1.** Co-PDC source parameters defined for historical PDC and co-PDC eruptions. The minimum data (referring to the 1991 eruption of Unzen) for $A$, $\alpha$ and $dx$ are taken from Watanabe et al. (1999), whereas the maximum data (referring to the May 18th, 1980 eruption of Mount St Helens (MSH)) for $A$, $\alpha$, and $dy$ are taken from Fisher et al. (1987). We used Unzen and MSH as end-members to describe potential co-PDC plume parameters and behaviour. $H_T$ is taken from data sets from Aubry et al. (2021), Eychenne & Engwell (2022), Mastin et al. (2009) and Pioli et al. (2019) and $dz$ from Bonadonna & Phillips (2003) and Carey & Sparks (1986).

| **Parameter** | **Symbol** | **Unit** | **Min** | **Max** |
|---|---|---|---|---|
| **Area** | $A$ | $km^2$ | 0.4 | 619 |
| **Aspect ratio** | α | - | 0.2 | 1.7 |
| **Width of source in plan view** | $dx$ | km | 0.3 | 32.4 |
| **Length of source in plan view** | $dy$ | km | 0.5 | 55.6 |

| | | | | |
|---|---|---|---|---|
| **Maximal plume height** | $H_T$ | km | 1 | 30 |
| **Thickness of ash release** | *dz* | km | 0.3 | 9.0 |

### 2.4. Particle Characteristics

Ash particles that comprise co-PDCs have been found to have densities between 2200 kg $m^{-3}$ and 2600 kg $m^{-3}$ (Bonadonna & Phillips, 2003; Watanabe et al., 1999). Given this narrow range and that Beckett et al. (2015) showed that differences in particle densities over this range have no significant impact on NAME output, we used 2500 kg $m^{-3}$ for all our experimental runs. We assumed no aggregation throughout this study.

The total grain size distribution (TGSD) of a co-PDC plume (modified from Marti et al. (2016)) was used for the particle size distribution (PSD) in NAME and thus specifies the diameter, *d*, of the particles. The range of particle diameters was split into nine bins with 1.5 $\varphi$ (phi) intervals between 11.25 $\varphi$ and -0.75 $\varphi$, where $\varphi$ is defined as $\varphi = -\log_2 d(\mathrm{mm})$. The calculated distribution used in this study is shown in Table 2 and all particles were treated as spheres. The mass distribution is further shown in Figure 4.

**Table 2.** Total grain size distribution (TGSD) modified from Marti et al. (2016). The particle diameters, *d*, were grouped into equal bins with 1.5 $\varphi$ intervals.

| ***d* ($\varphi$-scale)** | ***d* (µm)** | **Cumulative volume** |
|---|---|---|
| 11.25 | 0.41 | 0 |
| 9.75 | 1.16 | 0.0051 |
| 8.25 | 3.28 | 0.0415 |
| 6.75 | 9.29 | 0.1799 |
| 5.25 | 26.28 | 0.4882 |
| 3.75 | 74.33 | 0.8027 |
| 2.25 | 210.22 | 0.9433 |
| 0.75 | 594.60 | 0.9864 |
| - 0.75 | 1681.79 | 1 |

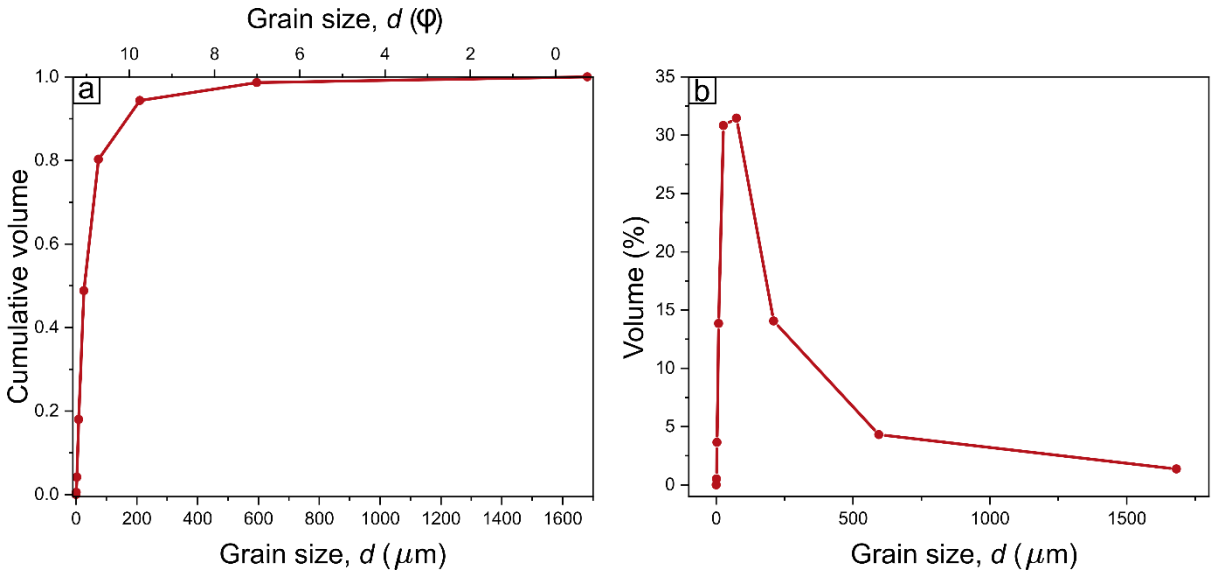


**Figure 4.** The total grain size distribution (modified) from Marti et al. (2016) for **(a)** cumulative volume distribution and **(b)** particle size fraction.

### 2.5. Numerical Experiments

We performed two numerical experiments. In the firstexperiment, we used a constant source strength and plume height but used three different source aspect ratios changing the source area, thus the width and length of the source geometry. Here, we assume that the area and shape of the ground footprint are the same as that at the level of neutral buoyancy where the particles were released. We neglect any plume widening. This allowed us to independently investigate the impact of the source geometric properties on the onwards transport and dispersion of the ash cloud. In the second numerical experiment, we appropriately coupled the plume height, height interval of ash release, and source strength for each run and modelled a range of source geometries and areas. This represents a more realistic set of eruption conditions and allows us to test the influence of MER/$H_T$ on the simulated location and mass loadings of ash in the downwind cloud.

#### 2.5.1. Numerical Experiment 1: Source Aspect Ratio and Area

This experimental set analysed the impact of the aspect ratio and total source area on the plume shape and position. The minimum and maximum aspect ratios were determined from the literature as 0.2 and 1.7, respectively and a mid-point value was calculated (0.95) to simply provide a third aspect ratio (cf. Table 1; Fig. 2). For each aspect ratio (0.2, 0.95, and

1.7), ten different source areas between 0.4 km$^2$ and 619 km$^2$ (Table 1) and the logarithmic mid-point were used. The full model set up conditions that comprise the numerical experiment 1 are displayed in Table 3. All other eruption source parameters were kept constant: $H_T$ was set to 10 km (agl) and thus yielded a *dz* of 3 km and *z*, the mid plume height, was 8.5 km. The source strength was set to 1.06 x $10^{13}$ g h$^{-1}$.

To ensure that any observations made also hold true for different weather patterns, we perform the same set of numerical experiments for the eight different weather patterns defined for the North Atlantic and surrounding European (Neal et al., 2016). The date commonly presented throughout this manuscript, 31$^{st}$ January 2022, is described best by weather pattern number 3. For detailed information on the other chosen dates, representative of the other weather patterns, the reader is referred to the supplementary information.

**Table 3.** Source parameters of numerical experiment 1. Three different aspect ratios were each used for eleven different source geometry areas. The width and length of the geometry were determined by Equations 3 and 4. Runs (1) to (11) used an aspect ratio of 0.2, runs (12) to (22) used an aspect ratio of 1.7, and runs (23) to (33) used the mid aspect ratio of 0.95. The source perimeter, $P = 2 \cdot dx + 2 \cdot dy$, is also indicated for comparison.

| **Run: $\alpha$ = 0.2** | (1) | (2) | (3) | (4) | (5) | (6) | (7) | (8) | (9) | (10) | (11) |
|---|---|---|---|---|---|---|---|---|---|---|---|
| ***A* (km$^2$)** | 0.4 | 1 | 2 | 5 | 10 | 16 | 24 | 50 | 121 | 274 | 619 |
| ***dx* (km)** | 0.3 | 0.4 | 0.6 | 1.0 | 1.4 | 1.8 | 2.2 | 3.2 | 4.9 | 7.4 | 11.1 |
| ***dy* (km)** | 1.4 | 2.1 | 3.2 | 4.8 | 7.2 | 8.9 | 10.9 | 15.9 | 24.6 | 37.0 | 55.6 |
| ***P* (km)** | 3.4 | 5.0 | 7.6 | 11.6 | 17.2 | 21.4 | 26.2 | 38.2 | 59.0 | 88.8 | 133.4 |
| | | | | | | | | | | | |
| **Run: $\alpha$ = 1.7** | (12) | (13) | (14) | (15) | (16) | (17) | (18) | (19) | (20) | (21) | (22) |
| ***A* (km$^2$)** | 0.4 | 1 | 2 | 5 | 10 | 16 | 24 | 50 | 121 | 274 | 619 |
| ***dx* (km)** | 0.8 | 1.2 | 1.9 | 2.8 | 4.2 | 5.2 | 6.3 | 9.3 | 14.3 | 21.6 | 32.4 |
| ***dy* (km)** | 0.5 | 0.7 | 1.1 | 1.6 | 2.5 | 3.1 | 3.7 | 5.4 | 8.4 | 12.7 | 19.1 |
| ***P* (km)** | 2.6 | 3.8 | 6.0 | 8.8 | 13.4 | 16.6 | 20.0 | 29.4 | 45.4 | 68.6 | 103.0 |
| | | | | | | | | | | | |
| **Run: $\alpha$ = 0.95** | (23) | (24) | (25) | (26) | (27) | (28) | (29) | (30) | (31) | (32) | (33) |
| ***A* (km$^2$)** | 0.4 | 1 | 2 | 5 | 10 | 16 | 24 | 50 | 121 | 274 | 619 |
| ***dx* (km)** | 0.6 | 0.9 | 1.4 | 2.1 | 3.2 | 3.9 | 4.7 | 6.9 | 10.7 | 16.1 | 24.2 |
| ***dy* (km)** | 0.6 | 1.0 | 1.5 | 2.2 | 3.3 | 4.1 | 5.0 | 7.3 | 11.3 | 17.0 | 25.5 |
| ***P* (km)** | 2.4 | 3.8 | 5.8 | 8.6 | 13.0 | 16.0 | 19.4 | 28.4 | 44.0 | 66.2 | 99.4 |

### 2.5.2. Numerical Experiment 2: coupled $H_T$ and MER for different $A$ and $\alpha$

This numerical experiment better represents the natural case, by the appropriate coupling of the plume height $H_T$, the vertical thickness of ash release $dz$, and the MER. Specifically, five different plume heights were chosen following Table 1, covering the full range of heights expected for natural co-PDC plumes.

For each plume height, the associated source strength (MER) was calculated using Equation 5 and the thickness of ash release by Equation 6. All other parameters, such as the particle size distribution, the eruption start time (thus meteorological conditions), and the emission duration, were kept constant and are the same as in experiment 1. These different cases have all been modelled by using two different aspect ratios and the minimum, middle, and maximum source geometry areas with both wet and dry deposition included. Table 4 provides the full model set-up conditions of numerical experiment 2, indicating the plume height $dz$, MER, $\alpha$, $A$, $dx$, $dy$, and the run number for each model run.

**Table 4.** Source parameters for numerical experiment 2. Different total plume heights define the thickness of ash release and source strength (MER), which were tested for different source geometries (aspect ratios and areas). The designated reference number of each model run is given in brackets and highlighted in grey. The source perimeter, $P = 2 \cdot dx + 2 \cdot dy$, is also indicated for comparison.

| $H_T$ (km) | $z$ (km) | $dz$ (km) | MER | $\alpha$ | Run | (1) | (2) | (3) |
|---|---|---|---|---|---|---|---|---|
| 1 | 0.85 | 0.3 | 1.41E+02 (kg s$^{-1}$) = 5.07E+08 (g h$^{-1}$) | 0.2 | $A$ (km$^2$) | 0.4 | 16 | 619 |
| | | | | | $dx$ (km) | 0.3 | 1.8 | 11.1 |
| | | | | | $dy$ (km) | 1.4 | 8.9 | 55.6 |
| | | | | | $P$ (km) | 3.4 | 12.5 | 133.4 |
| | | | | 1.7 | Run | (4) | (5) | (6) |
| | | | | | $A$ (km$^2$) | 0.4 | 16 | 619 |
| | | | | | $dx$ (km) | 0.8 | 5.2 | 32.4 |
| | | | | | $dy$ (km) | 0.5 | 3.1 | 19.1 |
| | | | | | $P$ (km) | 2.6 | 16.6 | 103.0 |
| 5 | 4.25 | 1.5 | 1.12E+05 (kg s$^{-1}$) = 4.03E+11 (g h$^{-1}$) | 0.2 | Run | (7) | (8) | (9) |
| | | | | | $A$ (km$^2$) | 0.4 | 16 | 619 |
| | | | | | $dx$ (km) | 0.3 | 1.8 | 11.1 |
| | | | | | $dy$ (km) | 1.4 | 8.9 | 55.6 |
| | | | | | $P$ (km) | 3.4 | 12.5 | 133.4 |
| | | | | 1.7 | Run | (10) | (11) | (12) |
| | | | | | $A$ (km$^2$) | 0.4 | 16 | 619 |
| | | | | | $dx$ (km) | 0.8 | 5.2 | 32.4 |
| | | | | | $dy$ (km) | 0.5 | 3.1 | 19.1 |
| | | | | | $P$ (km) | 2.6 | 16.6 | 103.0 |
| 10 | 8.5 | 3.0 | 1.99E+06 (kg s$^{-1}$) = 7.15E+12 (g h$^{-1}$) | 0.2 | Run | (13) | (14) | (15) |
| | | | | | $A$ (km$^2$) | 0.4 | 16 | 619 |
| | | | | | $dx$ (km) | 0.3 | 1.8 | 11.1 |
| | | | | | $dy$ (km) | 1.4 | 8.9 | 55.6 |
| | | | | | $P$ (km) | 3.4 | 12.5 | 133.4 |
| | | | | 1.7 | Run | (16) | (17) | (18) |
| | | | | | $A$ (km$^2$) | 0.4 | 16 | 619 |

| | | | | | | | | |
|---|---|---|---|---|---|---|---|---|
| | | | | | ***dx* (km)** | 0.8 | 5.2 | 32.4 |
| | | | | | ***dy* (km)** | 0.5 | 3.1 | 19.1 |
| | | | | | ***P* (km)** | 2.6 | 16.6 | 103.0 |
| 20 | 17.0 | 6.0 | 3.53E+07 (kg $s^{-1}$) = 1.27E+14 (g $h^{-1}$) | 0.2 | **Run** | **(19)** | **(20)** | **(21)** |
| | | | | | ***A* ($km^2$)** | 0.4 | 16 | 619 |
| | | | | | ***dx* (km)** | 0.3 | 1.8 | 11.1 |
| | | | | | ***dy* (km)** | 1.4 | 8.9 | 55.6 |
| | | | | | ***P* (km)** | 3.4 | 12.5 | 133.4 |
| | | | | 1.7 | **Run** | **(22)** | **(23)** | **(24)** |
| | | | | | ***A* ($km^2$)** | 0.4 | 16 | 619 |
| | | | | | ***dx* (km)** | 0.8 | 5.2 | 32.4 |
| | | | | | ***dy* (km)** | 0.5 | 3.1 | 19.1 |
| | | | | | ***P* (km)** | 2.6 | 16.6 | 103.0 |
| 27 | 22.95 | 8.1 | 1.22E+08 (kg $s^{-1}$) = 4.41E+14 (g $h^{-1}$) | 0.2 | **Run** | **(25)** | **(26)** | **(27)** |
| | | | | | ***A* ($km^2$)** | 0.4 | 16 | 619 |
| | | | | | ***dx* (km)** | 0.3 | 1.8 | 11.1 |
| | | | | | ***dy* (km)** | 1.4 | 8.9 | 55.6 |
| | | | | | ***P* (km)** | 3.4 | 12.5 | 133.4 |
| | | | | 1.7 | **Run** | **(28)** | **(29)** | **(30)** |
| | | | | | ***A* ($km^2$)** | 0.4 | 16 | 619 |
| | | | | | ***dx* (km)** | 0.8 | 5.2 | 32.4 |
| | | | | | ***dy* (km)** | 0.5 | 3.1 | 19.1 |
| | | | | | ***P* (km)** | 2.6 | 16.6 | 103.0 |

## 3 Results & Discussion

In this section, we will show the results from our systematic NAME model runs (as outlined in Tables 3 & 4) and consider the individual impact of different source parameters on the transport and dispersion of the co-PDC ash cloud. To do this, and to provide a common comparison across all runs, we use the horizontal position and extent of the whole ash cloud and the total column mass loading. Where the total column mass loading is the sum of all ash vertically above the ground at a given location and thus has units of g $m^{-2}$. These data are extracted every hour after the emission/eruption started ($t_0$) up until 24 hours later. We

applied a threshold of 0.2 g $m^{-2}$ as it aligns to the threshold which satellite instruments can typically detect and retrieve volcanic ash (Saint et al., 2024). Furthermore, it is the lowest concentration threshold required for VAAC forecasts, if we assume the ash cloud has a 1 km thickness (Beckett et al., 2020).

### 3.1. Impact of source area, *A*

First, let us consider the impact of the source area, *A*, for a constant source aspect ratio, $\alpha$. Figure 5 provides an overview of the size and orientation of all source geometries used in this study. They are shown in their true locations with respect to Hekla volcano (black triangle) and to Iceland. For context, Iceland has a total land area of approximately 104,000 $km^2$ and the minimum and maximum co-PDC plume source areas were 0.4 $km^2$ and 619 $km^2$, respectively.

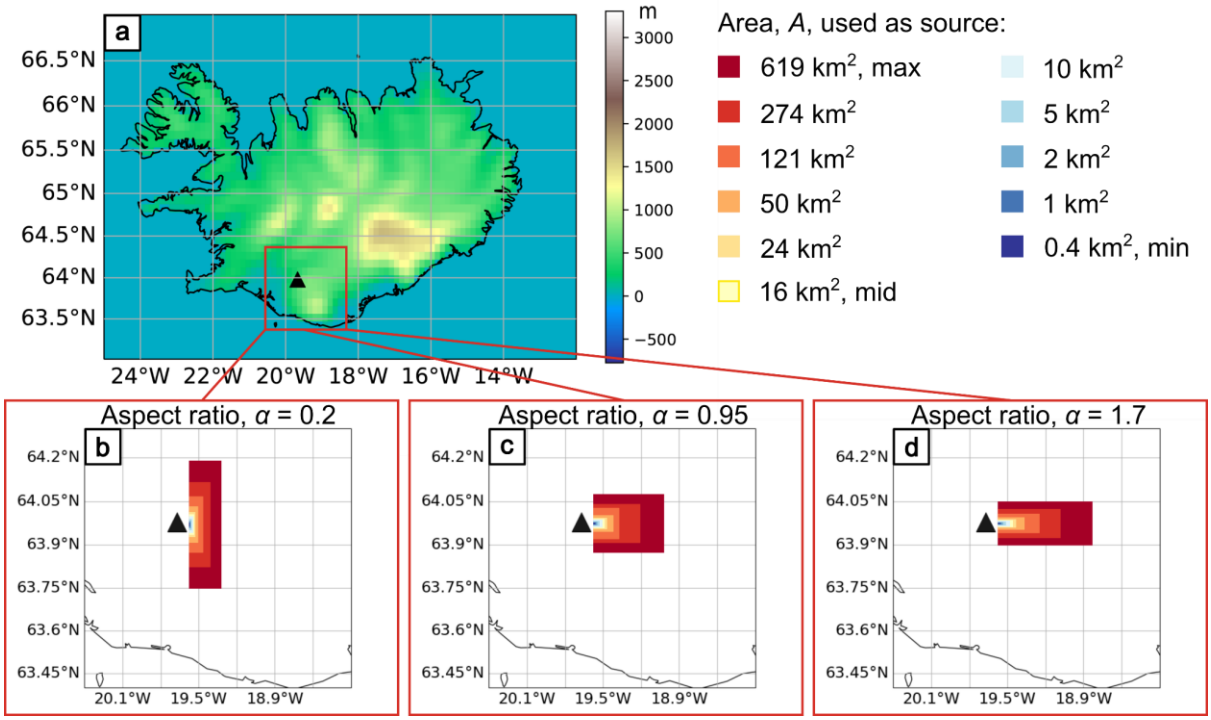


**Figure 5:** Orientation and size of the source for the different aspect ratios and areas used in our model runs. **(a)** A map of Iceland, showing the ground elevation using the global 10 km resolution topography data used with the NAME simulations. The colour bar shows the ground elevation in meters above sea level. The lower panels show the range of source areas for aspect ratios, **(b)** $\alpha_{min}$ = 0.2, **(c)** $\alpha_{mid}$ = 0.95, and **(d)** $\alpha_{max}$ = 1.7 used in this study.

397

398 To compare the ash cloud generated by different source geometry areas, we plot the ash
399 clouds from a 0.4 km$^2$ (min) and 619 km$^2$ (max) source area, both with aspect ratio, $\alpha_{min}$ =
400 0.2. These results are shown in Figure 6. The simulated ash clouds grow with time, following
401 the wind field towards the east and show similar downwind shapes. The initial latitudinal
402 extent of the ash clouds close to the source location shows the most deviation; however, as
403 the age of the cloud increases and it becomes more dispersed, the differences between the
404 simulations initialised with minimum and maximum source area are insignificant.
405 Quantitatively, the difference in cloud position was compared between these two end-member
406 cases using the Figure of Merit in Space, FMS (Rolph et al., 2014; Warner et al., 2004):

$$\mathrm{FMS} = \frac{A_1 \cap A_2}{A_1 \cup A_2} \cdot 100 \qquad [9]$$

407 where $A_1$ is the cloud area within one model output and $A_2$ the cloud area in another model
408 output. The intersection is compared with the union of these areas. The areas correspond to
409 the forecasted cloud areas with mass loading ≥ 0.2 g m$^{-2}$. High FMS values correspond to
410 high agreement between the models. These results are shown in Figure 7a.

411

412

413

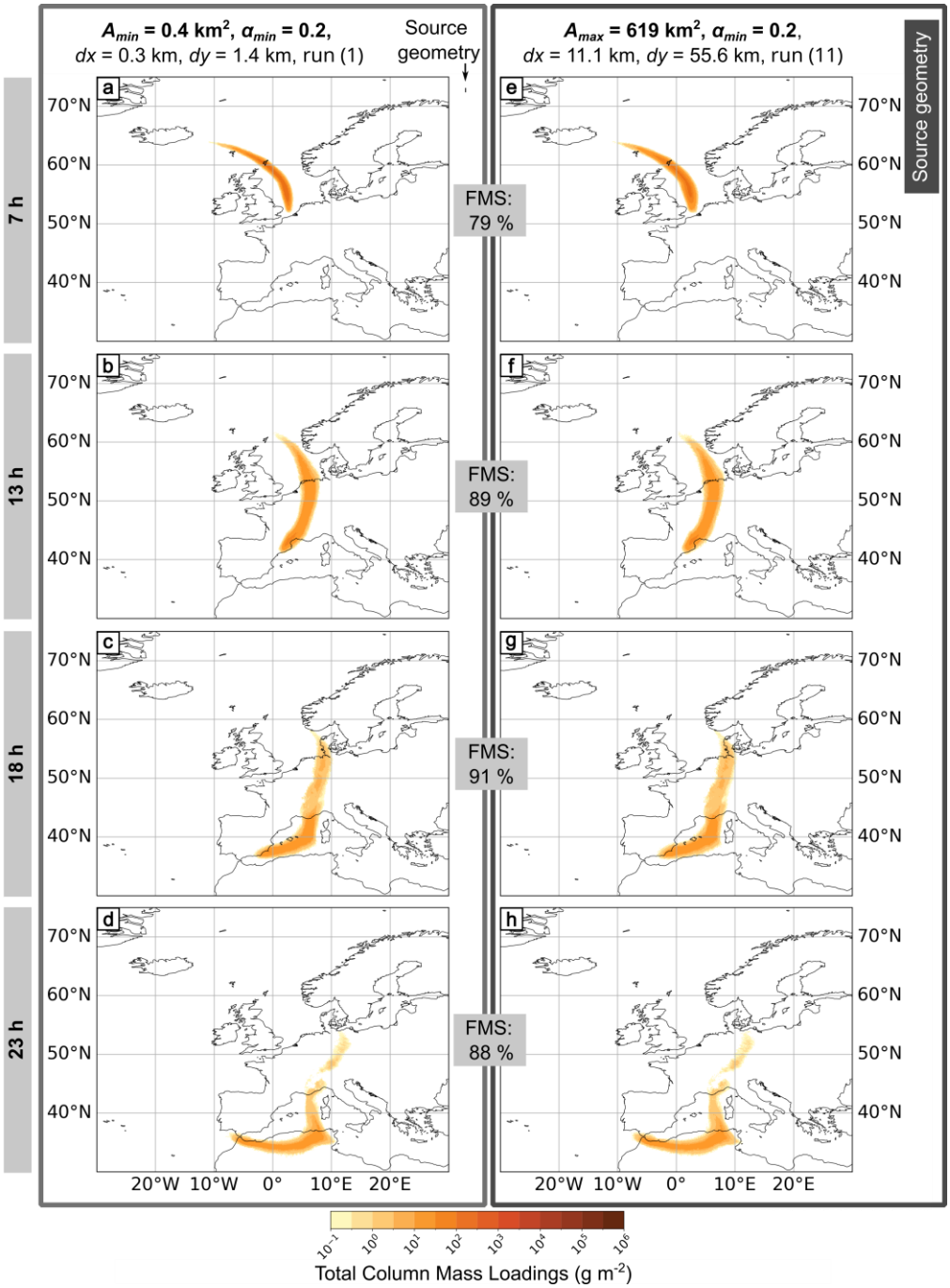


414

415 **Figure 6.** NAME outputs for numerical experiment 1, all using $\alpha_{min}$ = 0.2, a 1 h particle
416 release, $z$ = 8.5 km, $dz$ = 3 km and MER = 1.06 x $10^{13}$ g $h^{-1}$. The panels on the left are for the
417 minimum source area, and the panels on the right are for the maximum. The area and
418 orientation of the two source geometries are compared in relation to each other next to the
419 parameter list at the top of the figure. For each area, four outputs are presented at different
420 times after the eruption start *to*: **(a & e)** 7 h, **(b & f)** 13 h, **(c & g)** 18 h, and **(d & h)** 23 h.
421 Total column mass loadings are averaged over the previous hour, and we applied a threshold
422 of 0.2 g $m^{-2}$.

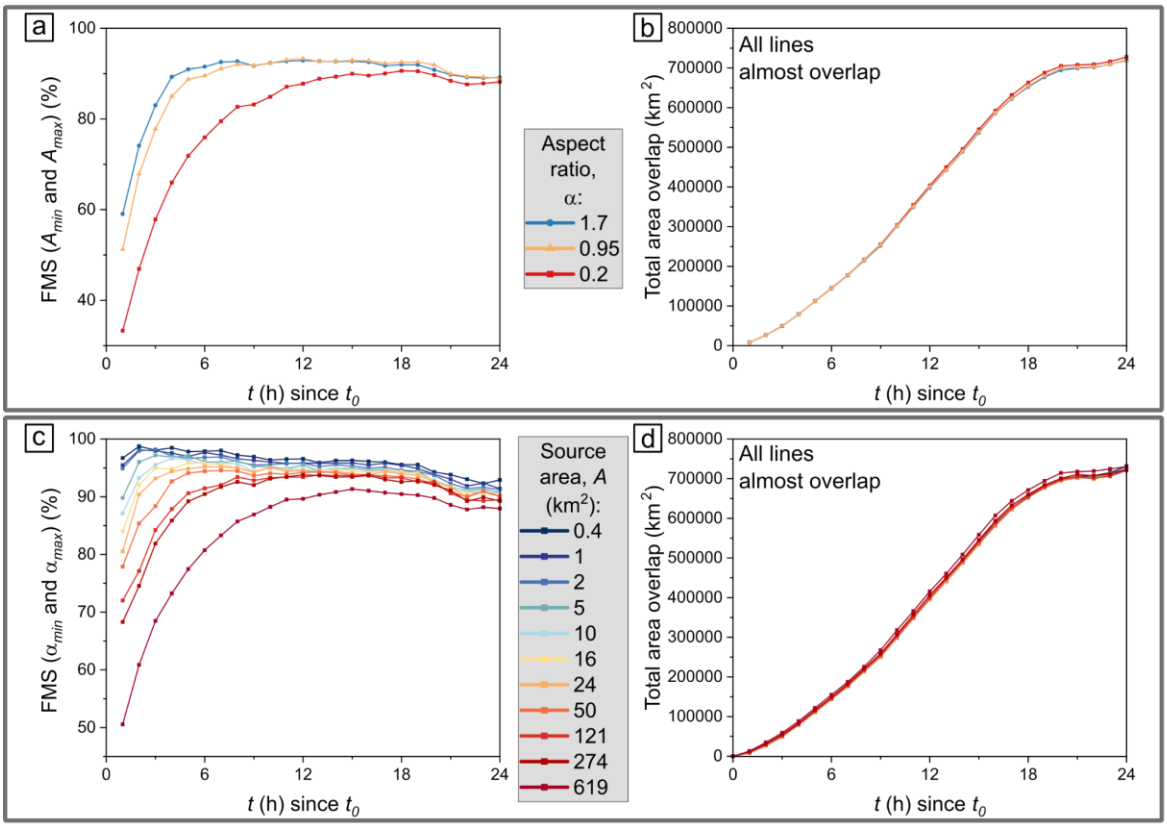


**Figure 7.** The Figure of Merit in space (FMS) and total cloud area overlap within numerical experiment 1. **(a)** FMS between the plumes generated using minimum ($A_{min}$) and maximum ($A_{max}$) source area. The different coloured data points correspond to different aspect ratios. **(b)** Actual area overlap between $A_{min}$ and $A_{max}$. **(c)** FMS between the plumes generated with the minimum ($\alpha_{min}$) and maximum ($\alpha_{max}$) aspect ratio. The different coloured data points correspond to different source areas. **(d)** Actual area of overlap between $\alpha_{min}$ and $\alpha_{max}$. The lines between data points are not model fits and are just used to guide the eye.

For all aspect ratios, the FMS, calculated between the ash clouds generated by model runs using the minimum ($A_{min}$) and maximum ($A_{max}$) source area, increases with time after $t_0$ until a plateau is reached. The near-source variations are more pronounced as there is less cloud area to compare with. The plateau occurs at ~ 90% FMS for all aspect ratios but is achieved faster for the larger aspect ratios (Figure 7a). Additionally, in all cases, there is a slight decrease in the FMS after ~ 20 h. We also find that generally $\alpha_{min}$ = 0.2 has the lowest FMS values. However, the actual overlapping cloud area is still the largest for $\alpha_{min}$ = 0.2 with values up to 728,000 km$^2$ (Figure 7b). Although, it must be stressed that this is not strictly related to the value of the aspect ratio but to the applied weather conditions. This can be

441 visualised in Figure 5 as the larger areas with $\alpha = 0.2$ show a larger longitudinal extension.
442 The extension in source geometry is perpendicular to the wind direction, and thus there is
443 more variability in the particle trajectories (especially in the first few hours since $t_0$). If the
444 source geometry is elongated with its long axis in the dominant wind direction (i.e., the larger
445 of *dx* or *dy* is parallel to the wind direction), there is a lower impact on differences in particle
446 trajectories.
447
448 The differences can also be evaluated in terms of total column mass loadings. For all cases,
449 higher total column mass loadings are found closer to the source location and at times closer
450 to the start of the release (e.g., Figure 6). Between the model runs with different source areas,
451 small changes in total column mass loadings towards the tip of the ash cloud are noticeable.
452 However, these are only identified within the first ~ 7 hours and at later times differences
453 become indistinguishable. In general, even when changing the source area by three orders of
454 magnitude, only small differences in downwind cloud shape and column mass loading are
455 observed. This is true for the full range of aspect ratios tested and the supporting plots for $\alpha$ =
456 0.95 and $\alpha = 1.7$ are shown in Figures S1 and S2.
457

458 **3.2. Impact of the aspect ratio of the source, $\alpha$**

459 To evaluate the impact of changing the aspect ratio of the source, $\alpha$, we present the results
460 from model runs for $\alpha_{min}$ and $\alpha_{max}$ at a common source area. The definition of the aspect ratio
461 (Equation 1) as the ratio between *dx* and *dy* was chosen here to quantitatively describe the
462 relationship between the width and the length of the source area. However, this enables
463 aspect ratios to range between almost zero to infinity. Other definitions of the source
464 geometry are possible, such as taking the ratio between the minimum and maximum
465 dimension, thus quantifying how equant the source area is.
466
467 Simulated total column mass loadings are shown in Figure 8 for $A_{max} = 619$ km$^2$. There are
468 only very small differences in the shape of the modelled cloud. After 7 hours since $t_0$, the tip
469 of the ash cloud appears thinner for $\alpha_{max} = 1.7$ (Figure 8e), compared to $\alpha_{min} = 0.2$ (Figure
470 8a). The FMS of the cloud area ranges from 83% to 90%. We consider these differences to be
471 small given the order of magnitude change in source aspect ratio (0.2 vs. 1.7). Similar results
472 are shown when comparing $\alpha_{min}$ and $\alpha_{max}$ for $A_{min} = 0.4$ km$^2$ and the related plots are shown in

Figure S3. Here, the FMS in the cloud areas is greater, and ranges from 98% to 92% from 7 h to 23 h since $t_0$, and thus slightly decreases with time during this 7 to 23 h period. Figure 7c compares the FMS of the ash cloud area between the minimum ($\alpha_{min}$) and maximum ($\alpha_{max}$) aspect ratio. In general, greater FMS values correspond to model runs with smaller source areas, whereas the actual area overlap is almost the same for all source areas (Figure 7d). Small source areas ($A < 5$ km$^2$) have large FMS (> 95%) until 4h after $t_0$ and slowly decreases with increased time after. However, at 24 h since $t_0$ the FMS is still > 90%. For the other source areas, $A \geq 5$ km$^2$, the FMS increases until (at least) 8 h, plateaus around 90% and then slightly decreases. The largest source area tested, $A = 619$ km$^2$, has the lowest FMS overall and is 51% at 1 h since $t_0$ and 88% at 24 h since $t_0$ (Figure 7c).

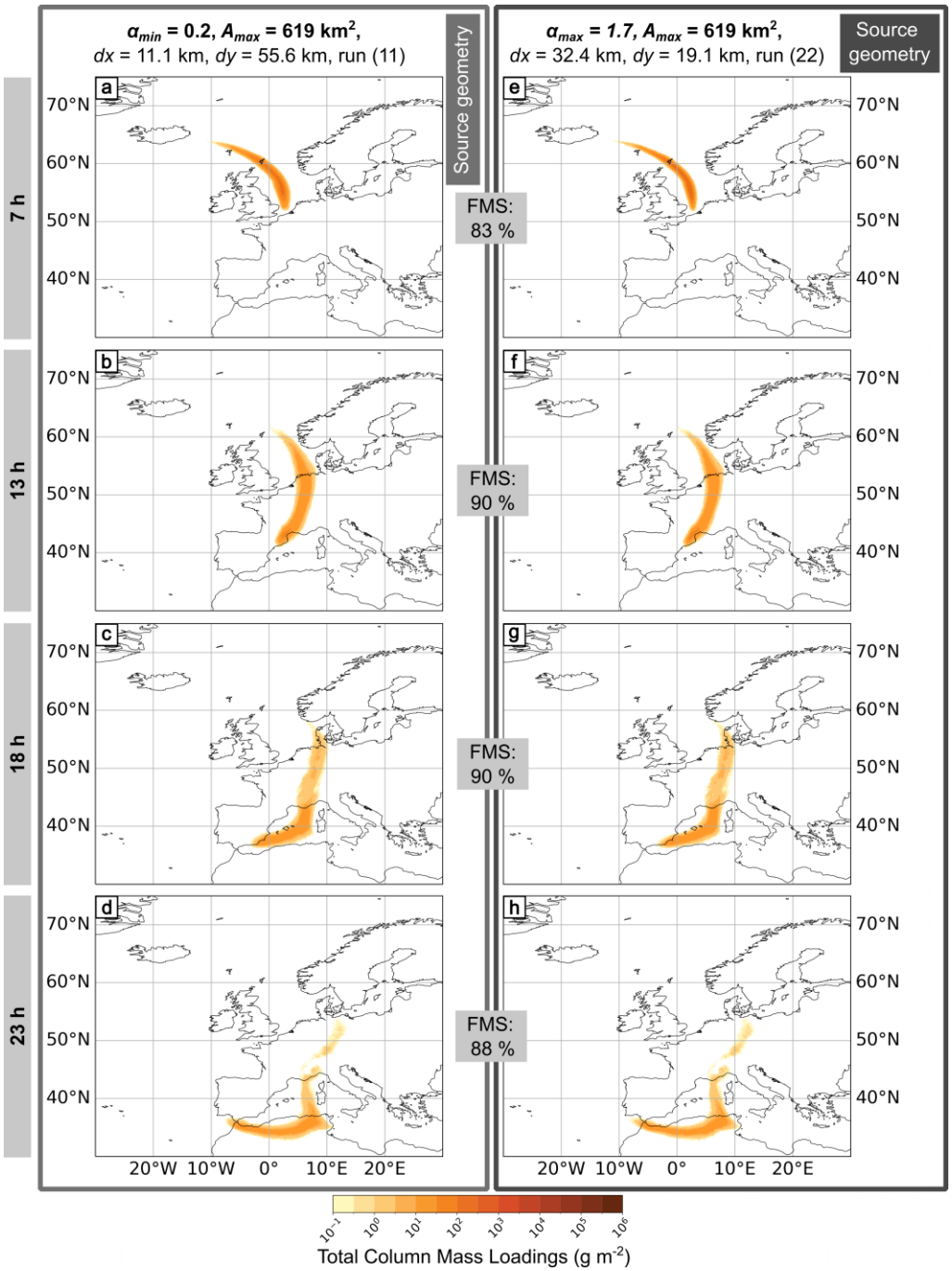


**Figure 8.** NAME model outputs for numerical experiment 1, all using $A_{max}$ = 619 km$^2$, a 1 h particle release, $z$ = 8.5 km, $dz$ = 3 km and MER = 1.06 x $10^{13}$ g h$^{-1}$. The left figure panels **(a-d)** show results from the minimum aspect ratio $\alpha_{min}$ = 0.2, and the right panels **(e-h)** show the maximum aspect ratio $\alpha_{max}$ = 1.7. The area and orientation of the two source geometries are compared in relation to each other next to the parameter list at the top of the figure. For each aspect ratio, four outputs at different times after eruption start $t_0$ are shown: **(a & e)** 7 h, **(b & f)** 13 h, **(c & g)** 18 h and **(d & h)** 23 h. Total column mass loadings are averaged over the previous hour, and we applied a threshold of 0.2 g m$^{-2}$.

### 3.3. Evaluation of geometric source properties ($A$ and $\alpha$) on co-PDC ash transport and dispersion

We now synthesise the results of the previous sections, that compared the impact of source area and aspect ratio, respectively. To supplement the visual comparisons between the NAME model outputs (cf. Figs. 6 and 8), we introduce the use of the relative standard deviation, %RSD:

$$\%\text{RSD} = \frac{\sigma}{\bar{x}} \cdot 100 \qquad [10]$$

where $\sigma$ is the standard deviation of the data set under study (e.g., cloud area at each hour after eruption start for all cloud areas) and $\bar{x}$ is the average of the data set (i.e., the ash cloud area generated throughout experiment 1 per given modelled time).

Due to the ~10 km horizontal resolution of the meteorological data used with our NAME simulations, source areas approximately $A \geq 10$ km$^2$ can have, in at least one dimension, a source geometry that is larger than the grid resolution and therefore crosses multiple meteorological grid cells. However, despite this, the total ash mass in the atmosphere is remarkably similar for all runs in experiment 1and the data almost overlap (Fig. S4). The total mass in the atmosphere has been studied for both the total data set and with the threshold of 0.2 g m$^{-2}$ applied. There are only minor differences between these datasets and therefore most larger particles (in particle sizes of co-PDCs) remain within the ash cloud. The total mass in the atmosphere reaches a maximum after 1 h (the total time of particle emission) and then decays as ash is removed through wet and dry deposition (including sedimentation) . Across all model outputs of experiment 1, the maximum %RSD is 0.4%, thus we can say, the total mass in the atmosphere is not affected by changing source aspect ratio or source area.

Overall, like the total mass in the atmosphere, the total cloud area, $A_c$, shows minor variation across all the source areas and aspect ratios investigated (Fig. 9). The only exception is at times close to the start of particle emission, $t_0$ and thus at cloud locations close to the source. Comparing all runs in experiment 1 (grey dotted line in Figure 9a & b), close to the start time (1 h since $t_0$), the relative standard deviation is 33%. However, these high %RSD values rapidly reduce to 9.5% after 4 h since $t_0$ and reach a low plateau of ~ 2% after 13 h. Furthermore, the total cloud area increases and shows little deviation between the different applied aspect ratios (Fig. 9a). By further analysing the cloud area, $A_c$, for a set plume height (here, $H_T$ = 10 km), the influence of aspect ratio (Fig. 9b) and area of the source geometry

(Fig. 9c) can be quantitatively investigated. Firstly, comparing different aspect ratios $\alpha_{min}$ = 0.2 has a maximum %RSD of 41% and reduces to < 10% after 6 h, whereas $\alpha_{mid}$ = 0.95 shows a maximum %RSD of 24% and becomes insignificant (≤ 9%) after 3 h, and $\alpha$ = 1.7 shows a maximum %RSD of 19% and becomes insignificant (≤ 6.5%) after 3 h.

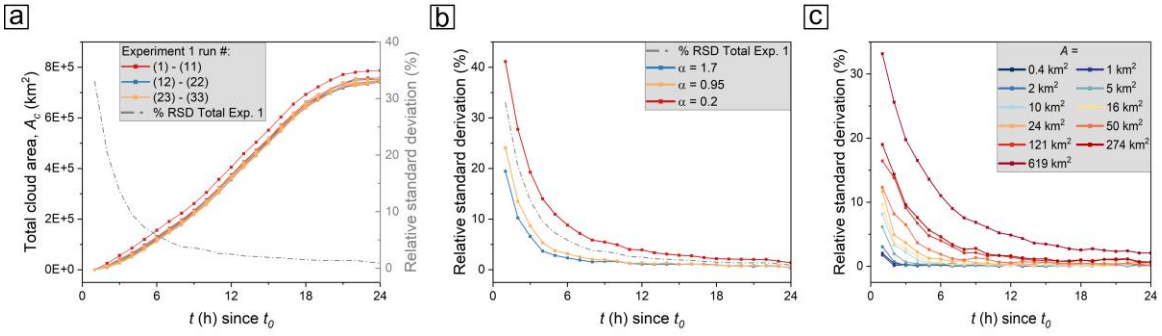


**Figure 9.** Total cloud area, $A_c$, for numerical experiment 1. **(a)** The total cloud area, $A_c$, for all model runs across Experiment 1. Although all lines (1) to (33) are represented, they mostly overlap. The %RSD is indicated by the grey dotted line. **(b)** Experiment 1 separated per aspect ratio, taking all source areas into account. $\alpha_{min}$ = 0.2 has a larger %RSD, as the longitudinal distance becomes more important with the specific applied weather conditions. There is no linear relationship between %RSD and $\alpha$. **(c)** Experiment 1 separated per source area $A$, where one line represents three runs each ($\alpha_{min}$ = 0.2, $\alpha$ = 0.95$_{mid}$ and $\alpha_{max}$ = 1.7). The larger the source area, the larger the %RSD. In all panels, the lines between data points are not model fits and are just used to guide the eye.

Furthermore, comparing the different source areas (each averaged over all three aspect ratios) used in experiment 1 (Fig. 9c), we find that the larger the source area, the higher the %RSD. The %RSD decays with time for all source areas. $A_{max}$ = 619 km$^2$ shows the largest %RSD of 33% at 1 h after particle release, whereas $A$ = 1 km$^2$ is only 1.8% RSD at the same time. Additionally, for a given time $t$, the %RSD is lower for smaller source areas. Only $A_{min}$ = 0.4 km$^2$ and $A$ = 1 km$^2$ do not exactly follow this observation until reaching 5 h since $t_0$, however, the %RSD is always ≤ 2%. For all source areas at 6 h since particle release, the %RSD is < 10 %.

Our observations that the cloud area growth is little impacted by the source geometry and aspect ratio can be explained mathematically. The cloud area can be described as

$$A(t) = A_0 + \int_0^t \left( \oint_{\partial A(\tau)} v_n(x,\tau)\, ds \right) d\tau \quad [11]$$

where $A_0$ is the source area at origin, $\partial A(\tau)$ is the boundary of the cloud at time $\tau$, and $v_n(x, \tau)$ is the normal expansion rate at point $x$ on the boundary. The derivative, describing the rate of change of the area,

$$\frac{dA(t)}{dt} = \oint_{\partial A(\tau)} v_n(x,\tau)\, ds \quad [12]$$

can be studied under the assumption of a rectangular source geometry with width $l_{xo}$ and length $l_{yo}$ expanding at constant rates $v_x$ *and* $v_y$ (uniform wind field). The area as a function of time, therefore, describes: $A(t) = l_{xo}l_{yo} + t(v_x l_{yo} + v_y l_{xo}) + v_x v_y t^2$ [13]

The quadratic term $v_x v_y t^2$, being of leading order at $t >> 0$, is not impacted by the initial source geometry at the source location. This therefore explains both the decrease in the %RSD (Fig. 9) and the convergence in total cloud area between all the runs with time as shown by the FMS (Fig. 7). For $t \sim 0$ h and times close to the eruption start, the ash cloud expands dominantly in the wind direction ($v_x$ for our specific date here). The extent of the perpendicular dimension, with respect to the wind ($l_{yo}$ here), is therefore of greater influence than the parallel dimension ($l_{xo}$ here). The linear term $l_{xo}l_{yo}$ is proportional to the perimeter (of the rectangular shape) and this therefore explains the high relative standard deviation between different aspect ratios.

For typical vent-derived plumes Mastin & Van Eaton (2020) have shown that considering the associated umbrella cloud growth is crucial for accurate modelling of the ash cloud area and downwind extent. They also show, as in this study, that the difference between cloud areas decrease with time after eruption. However, umbrella cloud areas typically range between 50 km$^2$ and 1,600,000 km$^2$ (Constantinescu et al., 2021; Mastin & Van Eaton, 2020; Prata et al., 2025; Zidikheri et al., 2017) and thus are larger than typical co-PDC clouds (e.g., 0.4 km$^2$ to 619 km$^2$). This further supports our observations that co-PDC cloud transport and dispersal (across the range of meteorological conditions tested here) is not impacted by the source area (due to the smaller contribution of the linear term in Equation 13).

### 3.4. The impact of co-PDC plume $H_T$ and MER

The modelled ash cloud shows completely different transport and dispersion patterns when changing $H_T$, and thus MER and $dz$. To illustrate this, in Figure 10 we show NAME outputs at 12 h (left side of figure) and 23 h since $t_0$ (right side of figure) initialised using a range of

plume heights ($H_T$) for $A_{max}$ = 619 km$^2$ with $\alpha_{min}$ = 0.2. In general, modelled total column mass loadings increase with $H_T$ and the larger $H_T$ and MER are, the larger the ash cloud becomes. For $H_T$ = 1 km (Figs. 10a & f), the total column mass loading threshold of 0.2 g m$^{-2}$ is not reached. The cloud generated by $H_T$ = 5 km has mass loadings ≥ 0.2 g m$^{-2}$ at 12 h (Fig. 10b) and 23 h since $t_0$ (Fig. 10g) but beyond 23 h, mass loadings are relatively low. The ash clouds generated by $H_T$ = 20 km (Fig. 10d) and $H_T$ = 27 km (Fig. 10e) form a relatively compact area at 12 h after particle release, however they become more elongated and stretched over wider areas for 23 h (Fig. 10i & j). For consistency, a set of model runs using $A_{max}$ = 619 km$^2$ with $\alpha_{max}$ = 1.7 and $A_{min}$ = 0.4 km$^2$ with $\alpha_{min}$ = 0.2 and $\alpha_{max}$ = 1.7 are shown in supplementary Figures S5 to S7. These combinations bracket the extremes in natural parameter space and still follow the general relationships described here. As shown in Figure 11, all ash cloud areas increase with time after the beginning of particle emission ($t_0$) and larger initial plume heights ($H_T$), thus larger mass eruption rates, correspond to larger cloud areas.

591

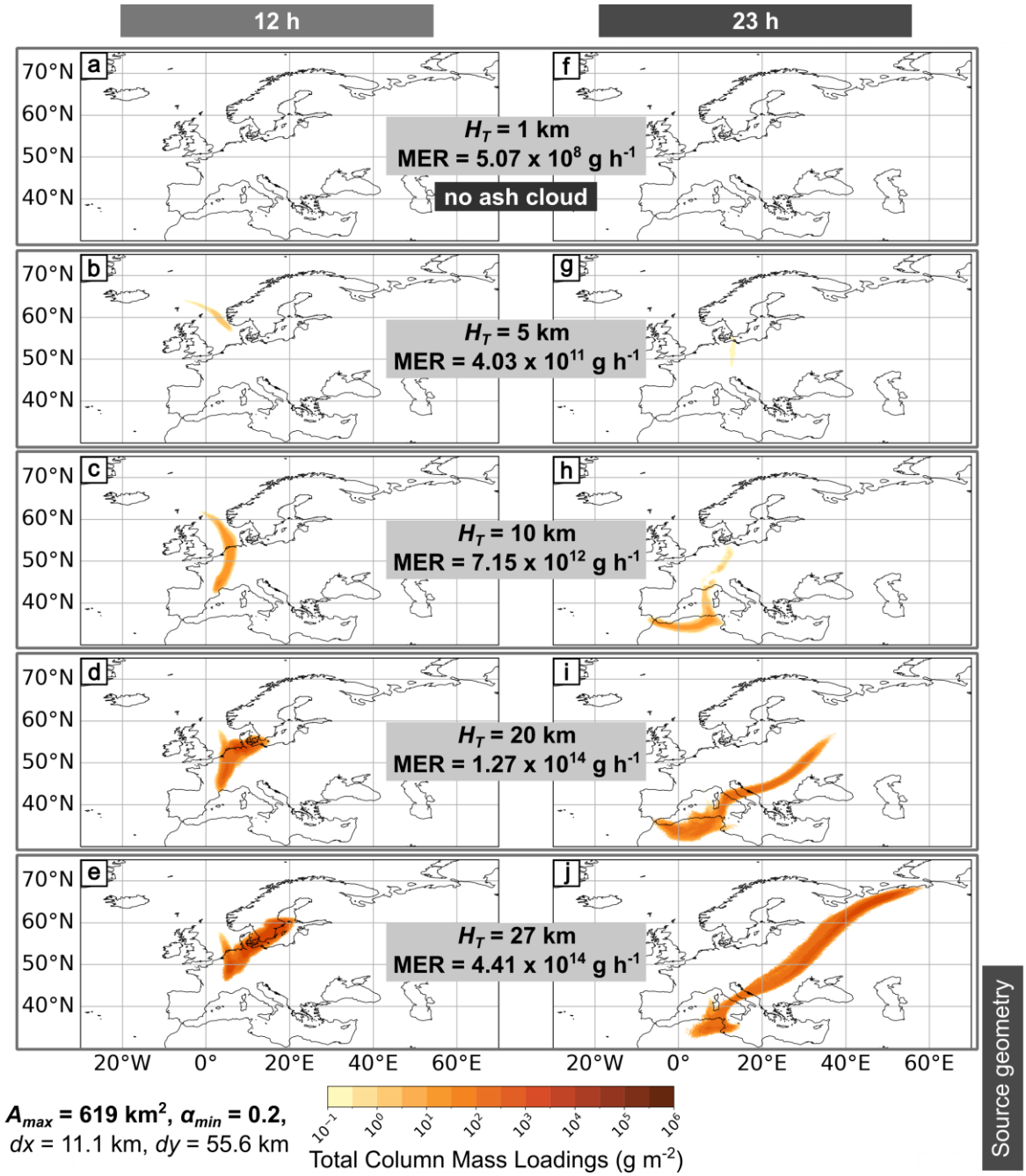


592 **Figure 10.** NAME model outputs for numerical experiment 2, all using a 1 h particle release
593 with different $H_T$, MER, and $dz$. The figure panels on the left **(a-d)** are for 12 h after eruption
594 start $t_0$, and the panels on the right **(e-h)** show 23 h after eruption start $t_0$. The outputs here are
595 for $A_{max}$ = 619 km$^2$ with $\alpha_{min}$ = 0.2. With increasing $H_T$ and $t_0 + t$ (h), the plume size grows.
596 Total column mass loadings are averaged over the previous hour, and we applied a threshold
597 of 0.2 g m$^{-2}$. The subplots (a & f) show no ash cloud (i.e., mass loading < 0.2 g m$^{-2}$).

598

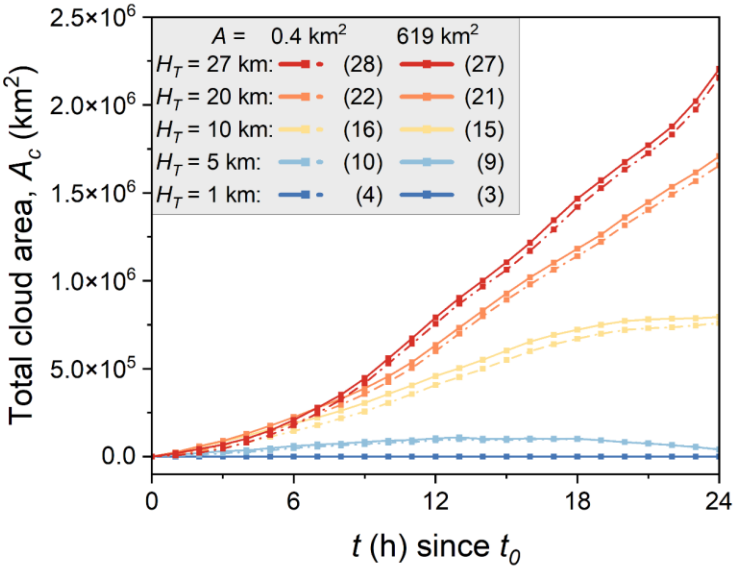


**Figure 11.** The total cloud area as a function of time for model runs within numerical experiment 2. The five different colours correspond to the different plume heights. Each with $A_{min}$ = 0.4 km$^2$ for $\alpha_{max}$ = 1.7 and $A_{max}$ = 619 km$^2$ for $\alpha_{min}$ = 0.2 as a dotted and solid line, respectively. The total plume area, $A_c$, increases for all plume heights with time within the first 13 h. $H_T$ = 1 km and $H_T$ = 5 km decay afterwards, while the others continue to increase. The numbers in brackets correspond to the model run number. The lines between data points are not model fits and are just used to guide the eye.

Figure 12 shows the total modelled mass in the atmosphere with time. As expected, with increasing plume height (and thus MER), the total mass in the atmosphere (and the total column mass loadings in Figure 10) also increases. The maximum total mass occurs (for each plume height) after 1 h, which is the end of the emission time. The total mass in the atmosphere released from higher plumes ($H_T$ = 10 km, $H_T$ = 20 km and $H_T$ = 27 km) remains almost constant, slightly decreasing, while when $H_T$ = 1 km and $H_T$ = 5 km there is a larger reduction/decay with time. When $H_T$ = 1 km the total mass decreases to 0.004% of the initial total mass at 24 h since $t_0$, whereas when $H_T$ = 27 km the ash cloud retains 68% of its initial total mass after 24 h.

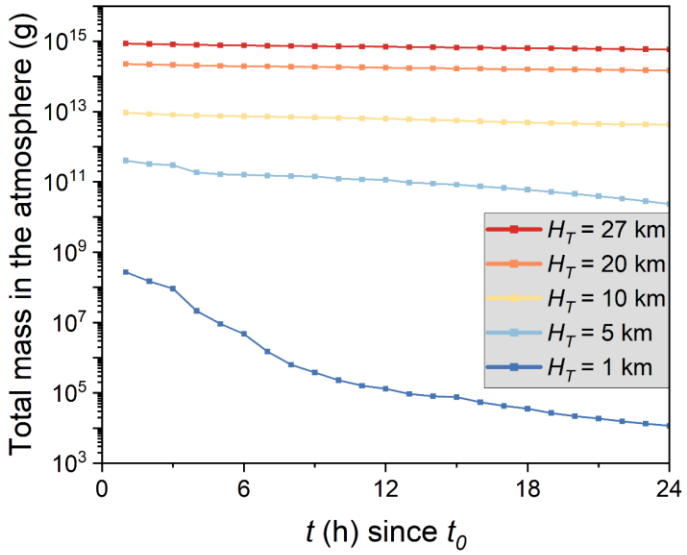


**Figure 12.** Total mass in atmosphere per plume height in numerical experiment 2. For visual clarity, only $A_{max}$ = 619 km$^2$, $\alpha_{min}$ = 0.2 is shown here, but the other runs show a similar relationship. For all plume heights, the total mass in the atmosphere is greatest at 1h since $t_0$ (end of particle emission) and decays afterwards. The smaller the plume height, the greater the decay. The lines between data points are not model fits and are just used to guide the eye.

### 3.5. Outlook and future work

NAME models the long-range transport and dispersion of ash clouds. In this study, we have represented the release of ash into the atmosphere with a set of eruption source parameters. However, additional schemes can be coupled to NAME to represent vent proximal behaviour, including those for buoyant plumes and umbrella clouds (Beckett et al., 2015; Devenish, 2013; Webster et al., 2012, 2020). At the expense of increased computational time, these schemes could be applied to investigate the dynamics of co-PDCs and, when coupled to NAME, their impact on the long-range transport of the resulting ash cloud.

We have assumed an emission duration of 1 h. This aligns with the resolution of the averaging period used for the modelled total column mass loadings. It is expected that co-PDC plumes will have a range of ash emission times corresponding to eruption parameters such as the MER and source area; however, no quantitative relationships currently exist. The emission time also becomes important if the emitted volume/mass of ash needs to be quantified to a higher accuracy. To test the sensitivity of our model outputs to the emission time, we re-ran all our model configurations with a 24 h release, the results of which can be

seen in the supplementary information (Figures S8 to S16). The key results outlined in this contribution show no difference when using this longer emission time (24 h vs 1 h). Only the total cloud area and total column mass loadings vary in their absolute magnitude.

Our model runs used an emission start time of 31st of January 2022, 09:00 UTC, at which time there were westerly winds, representative of the prevailing conditions in this area. Our results suggest that long-range transport and dispersion model simulations of ash clouds are insensitive to varying emission source areas and aspect ratios, within the range of end-members identified for co-PDC plumes. We would only expect there to be sensitivity if the meteorological conditions varied significantly across the area of the source, and for most meteorological scenarios, we would not expect large step changes in conditions across source areas typical of co-PDCs. There could be exceptions though, for example, the moment when there is a passage of a weather front or if there is a strong sea breeze. The sensitivity is also dependent on the resolution of the Numerical Weather Prediction (NWP) data and its ability to represent any variation. Here we have used NWP data from the Global configuration of the UM, which has a horizontal resolution of ~ 10 km, which has been shown to be optimal for representing long-range transport of ash clouds (see Beckett et al., 2020). We have repeated numerical experiment 1 for eight different weather patterns (Neal et al., 2016), describing different circulation types and therefore including different weather scenarios (Figures S17 to S58). The exact cloud shape and location vary with different weather patterns and dates, but our findings that the impact of source area and aspect ratio is negligible are confirmed across the data set. The FMS plateaus $\gtrsim$ 75% for all source areas, aspect ratios and weather patterns (Figures S17, S23, S29, S35, S41, S47, and S53). Further investigations are required to determine any impact of differing seasons or climates.

The applied relationship between $H_T$ and MER is well established for point sources; however, it is not clear how well this applies for elongated source geometries. Unknown, so far, is how the source area and MER are impacted by entrainment of ambient air, changing the particle concentration across the plume for these elongated source geometries. We assume entrainment to be lower along the edges of a linear plume than along the edges of a circular plume. It remains to be investigated whether large areas, i.e., $A_{max}$ = 619 km$^2$, are still likely to reach a plume height of $H_T$ = 30 km with the same MER predicted by the power law relationship derived from vent-derived plume information (Aubry et al., 2023) and whether the assumption of a uniform MER over the whole source area is suitable. Although the co-

PDC plume of MSH falls within the confidence interval of the MER relationship used here, smaller co-PDC plumes might be better described by a different plume scheme, e.g., a thermal buoyant plume, with an instantaneous mass release, meaning that the MER-$H_T$ relationship might be different (Biass et al., 2016; Bonadonna, Macedonio, et al., 2002; Druitt et al., 2002; Woods & Kienle, 1994).

The use of inversion approaches, such as that outlined by Pelley et al. (2021), to optimally constrain the time-varying distribution of mass with height at the source for vent-derived plumes have proved to be powerful tools during operational response when information may be scarce. Given our results show that capturing the plume height and MER is fundamentally important for co-PDC plumes too, then the use of inversion tools for this type of event will also be beneficial. Some inversion approaches have also explored optimising source geometry for umbrella cloud releases (Zidikheri et al., 2017). Here we have shown that after the first few hours, this is not a key parameter (due to its relatively small source area compared to umbrella clouds), however such an approach could also be further explored.

## 4 Conclusion

We studied the transport and dispersion of a volcanic ash cloud generated from a co-PDC plume to assess the sensitivity to the eruption source parameters used to initialise model simulations. Co-PDC ash plumes/clouds, generated from PDCs, have unique source properties, in particular their particle size distribution and source geometry are different to typical eruption plumes. Our sensitivity study showed that changes in the source area and the aspect ratio of the source have only a minor impact on the resultant cloud location and its total column mass loadings after ~ 6 h from the start of the release. The impact, during the early hours, is greatest if the long axis of the source geometry is perpendicular to the wind direction. However, as previously established for vent-derived plumes, the plume height and corresponding mass eruption rate are leading order parameters. Here we have shown that they yield significant differences when modelling transport and dispersion of co-PDC ash clouds. This result suggests that VAACs may not need to obtain a detailed description of the co-PDC source geometry, which would be difficult to establish quickly, and rather operational response should continue to focus on assigning optimal plume heights and MERs.

## Acknowledgements

The authors would like to acknowledge the Engineering & Physical Sciences Research Council (EPSRC) which funded this research (Grant reference EP/X525583/1). TJJ was also supported by a UK Research and Innovation (UKRI) Future Leaders Fellowship (Grant reference MR/W009781/1). The authors want to thank Nicola Stebbing from the Met Office, who kindly supplied a python script for the plume area overlap calculation (FMS) and supported in the application to our data set, and as well thanking the whole V&C group members at the Met Office for their support on NAME and technical related questions. Matthew Hort from the Met Office contributed with an inspiring conversation on the grid length resolutions. SLE was supported by the NC-ODA grant NE/R000069/1: Geoscience for Sustainable Futures and publishes with permission of the CEO, British Geological Survey. We would like to acknowledge Sarah Millington and Symeon Makris from the Met Office and BGS respectively, for their internal reviews. We also thank our journal reviewers Larry Mastin and Alice Crawford for useful comments that improved this paper.

## Conflict of Interest

The authors declare no conflicts of interest relevant to this study.

## Data Accessibility Statement

NAME III Version 8.5 was used in the transport and dispersion model simulations. The UK Met Office NAME model and UM output to drive NAME are available via license from the UK Met Office (© Crown Copyright, Met Office): https://www.metoffice.gov.uk/research/approach/modelling-systems/dispersion-model. The script used to generate the data used in this contribution can be found in the supporting information as [Supporting Information F1] uploaded to Zenodo (Hagenbourger et al., 2025).

## References

Andrews, B. J., & Manga, M. (2011). Effects of topography on pyroclastic density current runout and formation of coignimbrites. *Geology*, *39*(12), 1099–1102. https://doi.org/10.1130/G32226.1

Andrews, B. J., & Manga, M. (2012). Experimental study of turbulence, sedimentation, and coignimbrite mass partitioning in dilute pyroclastic density currents. *Journal of Volcanology and Geothermal Research*, *225–226*, 30–44. https://doi.org/10.1016/j.jvolgeores.2012.02.011

736 Aubry, T. J., Engwell, S. L., Bonadonna, C., Carazzo, G., Scollo, S., Van Eaton, A. R., Taylor, I. A.,
737 Jessop, D., Eychenne, J., Gouhier, M., Mastin, L. G., Wallace, K. L., Biass, S., Bursik, M.,
738 Grainger, R. G., Jellinek, A. M., & Schmidt, A. (2021). The Independent Volcanic Eruption
739 Source Parameter Archive (IVESPA, version 1.0): A new observational database to support
740 explosive eruptive column model validation and development. *Journal of Volcanology and*
741 *Geothermal Research*, *417*, 107295. https://doi.org/10.1016/j.jvolgeores.2021.107295
742 Aubry, T. J., Engwell, S. L., Bonadonna, C., Mastin, L. G., Carazzo, G., Van Eaton, A. R., Jessop, D.
743 E., Grainger, R. G., Scollo, S., Taylor, I. A., Jellinek, A. M., Schmidt, A., Biass, S., &
744 Gouhier, M. (2023). New Insights Into the Relationship Between Mass Eruption Rate and
745 Volcanic Column Height Based On the IVESPA Data Set. *Geophysical Research Letters*,
746 *50*(14), e2022GL102633. https://doi.org/10.1029/2022GL102633
747 Beckett, F. M., Bensimon, D., Crawford, A., Deslandes, M., Guidard, V., Hort, M. C., Jeoffrion, M.,
748 Kristiansen, N., Lucas, C., Nishijo, A., Osores, S., Renard, E., Servranckx, G., Snee, E.,
749 Trancoso, R., & Vazquez, E. (2024). *VAAC Model Setup Tables 2023*.
750 https://doi.org/10.5281/zenodo.10671098
751 Beckett, F. M., Witham, C. S., Hort, M. C., Stevenson, J. A., Bonadonna, C., & Millington, S. C.
752 (2015). Sensitivity of dispersion model forecasts of volcanic ash clouds to the physical
753 characteristics of the particles. *Journal of Geophysical Research: Atmospheres*, *120*(22),
754 11,636-11,652. https://doi.org/10.1002/2015JD023609
755 Beckett, F. M., Witham, C. S., Leadbetter, S. J., Crocker, R., Webster, H. N., Hort, M. C., Jones, A. R.,
756 Devenish, B. J., & Thomson, D. J. (2020). Atmospheric Dispersion Modelling at the London
757 VAAC: A Review of Developments since the 2010 Eyjafjallajökull Volcano Ash Cloud.
758 *Atmosphere*, *11*(4), 352. https://doi.org/10.3390/atmos11040352
759 Biass, S., Bonadonna, C., Connor, L., & Connor, C. (2016). TephraProb: A Matlab package for
760 probabilistic hazard assessments of tephra fallout. *Journal of Applied Volcanology*, *5*(1), 10.
761 https://doi.org/10.1186/s13617-016-0050-5
762 Bonadonna, C., Macedonio, G., & Sparks, R. S. J. (2002). Numerical modelling of tephra fallout
763 associated with dome collapses and Vulcanian explosions: Application to hazard assessment

764 on Montserrat. *Geological Society, London, Memoirs*, *21*(1), 517–537.
765 https://doi.org/10.1144/GSL.MEM.2002.021.01.23
766 Bonadonna, C., Mayberry, G. C., Calder, E. S., Sparks, R. S. J., Choux, C., Jackson, P., Lejeune, A.
767 M., Loughlin, S. C., Norton, G. E., Rose, W. I., Ryan, G., & Young, S. R. (2002). Tephra
768 fallout in the eruption of Soufrière Hills Volcano, Montserrat. In T. H. Druitt & B. P. Kokelaar
769 (Eds), *The Eruption of Soufrière Hills Volcano, Montserrat from 1995 to 1999* (Vol. 21, pp.
770 483–516). Geological Society of London. https://doi.org/10.1144/GSL.MEM.2002.021.01.22
771 Bonadonna, C., & Phillips, J. C. (2003). Sedimentation from strong volcanic plumes. *Journal of*
772 *Geophysical Research: Solid Earth*, *108*(B7), 2340. https://doi.org/10.1029/2002JB002034
773 Brown, A., Milton, S., Cullen, M., Golding, B., Mitchell, J., & Shelly, A. (2012). Unified Modeling
774 and Prediction of Weather and Climate: A 25-Year Journey. *Bulletin of the American*
775 *Meteorological Society*, *93*(12), 1865–1877. https://doi.org/10.1175/BAMS-D-12-00018.1
776 Brown, R. J., & Andrews, G. D. M. (2015). Chapter 36—Deposits of Pyroclastic Density Currents. In
777 H. Sigurdsson (Ed.), *The Encyclopedia of Volcanoes (Second Edition)* (pp. 631–648).
778 Academic Press. https://doi.org/10.1016/B978-0-12-385938-9.00036-5
779 Bursik, M. (2001). Effect of wind on the rise height of volcanic plumes. *Geophysical Research*
780 *Letters*, *28*(18), 3621–3624. https://doi.org/10.1029/2001GL013393
781 Bursik, M., & Woods, A. W. (1996). The dynamics and thermodynamics of large ash flows. *Bulletin of*
782 *Volcanology*, *58*(2), 175–193. https://doi.org/10.1007/s004450050134
783 Calder, E. S., Sparks, R. S. J., & Woods, A. W. (1997). Dynamics of co-ignimbrite plumes generated
784 from pyroclastic flows of Mount St. Helens (7 August 1980). *Bulletin of Volcanology*, *58*(6),
785 432–440. https://doi.org/10.1007/s004450050151
786 Carey, S., & Sparks, R. S. J. (1986). Quantitative models of the fallout and dispersal of tephra from
787 volcanic eruption columns. *Bulletin of Volcanology*, *48*(2), 109–125.
788 https://doi.org/10.1007/BF01046546
789 Charbonnier, S. J., & Gertisser, R. (2008). Field observations and surface characteristics of pristine
790 block-and-ash flow deposits from the 2006 eruption of Merapi Volcano, Java, Indonesia.

*Journal of Volcanology and Geothermal Research*, *177*(4), 971–982. https://doi.org/10.1016/j.jvolgeores.2008.07.008

Constantinescu, R., Hopulele-Gligor, A., Connor, C. B., Bonadonna, C., Connor, L. J., Lindsay, J. M., Charbonnier, S., & Volentik, A. C. M. (2021). The radius of the umbrella cloud helps characterize large explosive volcanic eruptions. *Communications Earth & Environment*, *2*(1), 3. https://doi.org/10.1038/s43247-020-00078-3

Dacre, H. F., Grant, A. L. M., Hogan, R. J., Belcher, S. E., Thomson, D. J., Devenish, B. J., Marenco, F., Hort, M. C., Haywood, J. M., Ansmann, A., Mattis, I., & Clarisse, L. (2011). Evaluating the structure and magnitude of the ash plume during the initial phase of the 2010 Eyjafjallajökull eruption using lidar observations and NAME simulations. *Journal of Geophysical Research: Atmospheres*, *116*(D20), D00U03. https://doi.org/10.1029/2011JD015608

Davies, T., Cullen, M. J. P., Malcolm, A. J., Mawson, M. H., Staniforth, A., White, A. A., & Wood, N. (2005). A new dynamical core for the Met Office's global and regional modelling of the atmosphere. *Quarterly Journal of the Royal Meteorological Society*, *131*(608), 1759–1782. https://doi.org/10.1256/qj.04.101

Dellino, P., Dioguardi, F., Isaia, R., Sulpizio, R., & Mele, D. (2021). The impact of pyroclastic density currents duration on humans: The case of the AD 79 eruption of Vesuvius. *Scientific Reports*, *11*(1), 4959. https://doi.org/10.1038/s41598-021-84456-7

Devenish, B. J. (2013). Using simple plume models to refine the source mass flux of volcanic eruptions according to atmospheric conditions. *Journal of Volcanology and Geothermal Research*, *256*, 118–127. https://doi.org/10.1016/j.jvolgeores.2013.02.015

Druitt, T. H. (1998). Pyroclastic density currents. *Geological Society, London, Special Publications*, *145*(1), 145–182. https://doi.org/10.1144/GSL.SP.1996.145.01.08

Druitt, T. H., Young, S. R., Baptie, B., Bonadonna, C., Calder, E. S., Clarke, A. B., Cole, P. D., Harford, C. L., Herd, R. A., Luckett, R., Ryan, G., & Voight, B. (2002). Episodes of cyclic Vulcanian explosive activity with fountain collapse at Soufrière Hills Volcano, Montserrat.

*Geological Society, London, Memoirs*, *21*(1), 281–306. https://doi.org/10.1144/GSL.MEM.2002.021.01.13

Dufek, J., Esposti Ongaro, T., & Roche, O. (2015). Chapter 35 - Pyroclastic Density Currents: Processes and Models. In H. Sigurdsson (Ed.), *The Encyclopedia of Volcanoes (Second Edition)* (pp. 617–629). Academic Press. https://doi.org/10.1016/B978-0-12-385938-9.00035-3

Dürig, T., Gudmundsson, M. T., Dioguardi, F., Woodhouse, M., Björnsson, H., Barsotti, S., Witt, T., & Walter, T. R. (2018). REFIR- A multi-parameter system for near real-time estimates of plume-height and mass eruption rate during explosive eruptions. *Journal of Volcanology and Geothermal Research*, *360*, 61–83. https://doi.org/10.1016/j.jvolgeores.2018.07.003

Engwell, S. L., de' Michieli Vitturi, M., Esposti Ongaro, T., & Neri, A. (2016). Insights into the formation and dynamics of coignimbrite plumes from one-dimensional models. *Journal of Geophysical Research: Solid Earth*, *121*(6), 4211–4231. https://doi.org/10.1002/2016JB012793

Engwell, S. L., & Eychenne, J. (2016). Chapter 4—Contribution of Fine Ash to the Atmosphere From Plumes Associated With Pyroclastic Density Currents. In S. Mackie, K. Cashman, H. Ricketts, A. Rust, & M. Watson (Eds), *Volcanic Ash* (pp. 67–85). Elsevier. https://doi.org/10.1016/B978-0-08-100405-0.00007-0

Eychenne, J., & Engwell, S. L. (2022). The grainsize of volcanic fall deposits: Spatial trends and physical controls. *GSA Bulletin*, *135*(7–8), 1844–1858. https://doi.org/10.1130/B36275.1

Fisher, R. V., Glicken, H. X., & Hoblitt, R. P. (1987). May 18, 1980, Mount St. Helens deposits in South Coldwater Creek, Washington. *Journal of Geophysical Research: Solid Earth*, *92*(B10), 10267–10283. https://doi.org/10.1029/JB092iB10p10267

Folch, A., Costa, A., & Basart, S. (2012). Validation of the FALL3D ash dispersion model using observations of the 2010 Eyjafjallajökull volcanic ash clouds. *Atmospheric Environment*, *48*, 165–183. https://doi.org/10.1016/j.atmosenv.2011.06.072

Giordano, G., & Cas, R. A. F. (2021). Classification of ignimbrites and their eruptions. *Earth-Science Reviews*, *220*, 103697. https://doi.org/10.1016/j.earscirev.2021.103697

Global Volcanism Program. (2024). *Volcanoes of the World* (No. Hekla (372070); Version 5.1.7) [Data set]. Distributed by Smithsonian Institution, compiled by Venzke, E. https://doi.org/10.5479/si.GVP.VOTW5-2024.5.2

Hagenbourger, M., Beckett, F., Jones, T. J., & Engwell, S. (2025). *Supporting Information: Modelling the transport and dispersion of volcanic co-PDC ash clouds using NAME: an evaluation of source geometry and mass eruption rate* (Version NAME III, v.8.5) [Computer software]. Zenodo. https://doi.org/10.5281/zenodo.15084579

Harvey, N. J., Huntley, N., Dacre, H. F., Goldstein, M., Thomson, D., & Webster, H. (2018). Multi-level emulation of a volcanic ash transport and dispersion model to quantify sensitivity to uncertain parameters. *Natural Hazards and Earth System Sciences*, *18*(1), 41–63. https://doi.org/10.5194/nhess-18-41-2018

Herzog, M., & Graf, H.-F. (2010). Applying the three-dimensional model ATHAM to volcanic plumes: Dynamic of large co-ignimbrite eruptions and associated injection heights for volcanic gases. *Geophysical Research Letters*, *37*(19), L19807. https://doi.org/10.1029/2010GL044986

Holasek, R. E., & Self, S. (1995). GOES weather satellite observations and measurements of the May 18, 1980, Mount St. Helens eruption. *Journal of Geophysical Research: Solid Earth*, *100*(B5), 8469–8487. https://doi.org/10.1029/94JB03137

Jones, A., Thomson, D., Hort, M., & Devenish, B. (2007). The U.K. Met Office's Next-Generation Atmospheric Dispersion Model, NAME III. In C. Borrego & A.-L. Norman (Eds), *Air Pollution Modeling and Its Application XVII* (pp. 580–589). Springer US. https://doi.org/10.1007/978-0-387-68854-1%255C_62

Jones, T. J., Beckett, F., Bernard, B., Breard, E. C. P., Dioguardi, F., Dufek, J., Engwell, S., & Eychenne, J. (2023). Physical properties of pyroclastic density currents: Relevance, challenges and future directions. *Frontiers in Earth Science*, *11*. https://doi.org/10.3389/feart.2023.1218645

Lube, G., Breard, E. C. P., Esposti-Ongaro, T., Dufek, J., & Brand, B. (2020). Multiphase flow behaviour and hazard prediction of pyroclastic density currents. *Nature Reviews Earth & Environment*, *1*(7), 348–365. https://doi.org/10.1038/s43017-020-0064-8

Marti, A., Folch, A., Costa, A., & Engwell, S. L. (2016). Reconstructing the plinian and co-ignimbrite sources of large volcanic eruptions: A novel approach for the Campanian Ignimbrite. *Scientific Reports*, *6*(1), 21220. https://doi.org/10.1038/srep21220

Mastin, L. G., Carey, S. N., Van Eaton, A. R., Eychenne, J., & Sparks, R. S. J. (2022). Understanding and modeling tephra transport: Lessons learned from the 18 May 1980 eruption of Mount St. Helens. *Bulletin of Volcanology*, *85*(1), 4. https://doi.org/10.1007/s00445-022-01613-0

Mastin, L. G., Guffanti, M., Servranckx, R., Webley, P., Barsotti, S., Dean, K., Durant, A., Ewert, J. W., Neri, A., Rose, W. I., Schneider, D., Siebert, L., Stunder, B., Swanson, G., Tupper, A., Volentik, A., & Waythomas, C. F. (2009). A multidisciplinary effort to assign realistic source parameters to models of volcanic ash-cloud transport and dispersion during eruptions. *Journal of Volcanology and Geothermal Research*, *186*(1–2), 10–21. https://doi.org/10.1016/j.jvolgeores.2009.01.008

Mastin, L. G., & Van Eaton, A. R. (2020). Comparing Simulations of Umbrella-Cloud Growth and Ash Transport with Observations from Pinatubo, Kelud, and Calbuco Volcanoes. *Atmosphere*, *11*(10), Article 10. https://doi.org/10.3390/atmos11101038

Michol, K. A., Russell, J. K., & Andrews, G. D. M. (2008). Welded block and ash flow deposits from Mount Meager, British Columbia, Canada. *Journal of Volcanology and Geothermal Research*, *169*(3), 121–144. https://doi.org/10.1016/j.jvolgeores.2007.08.010

Morton, B. R., Taylor, G. I., & Turner, J. S. (1956). Turbulent gravitational convection from maintained and instantaneous sources. *Proceedings of the Royal Society of London. Series A. Mathematical and Physical Sciences*, *234*(1196), 1–23. https://doi.org/10.1098/rspa.1956.0011

Neal, R., Fereday, D., Crocker, R., & Comer, R. E. (2016). A flexible approach to defining weather patterns and their application in weather forecasting over Europe. *Meteorological Applications*, *23*(3), 389–400. https://doi.org/10.1002/met.1563

Neri, A., Di Muro, A., & Rosi, M. (2002). Mass partition during collapsing and transitional columns by using numerical simulations. *Journal of Volcanology and Geothermal Research*, *115*(1), 1–18. https://doi.org/10.1016/S0377-0273(01)00304-3

Neri, A., Esposti Ongaro, T., Macedonio, G., & Gidaspow, D. (2003). Multiparticle simulation of collapsing volcanic columns and pyroclastic flow. *Journal of Geophysical Research: Solid Earth*, *108*(B4), 2202. https://doi.org/10.1029/2001JB000508

Pardini, F., Barsotti, S., Bonadonna, C., de' Michieli Vitturi, M., Folch, A., Mastin, L., Osores, S., & Prata, A. T. (2024). Dynamics, Monitoring, and Forecasting of Tephra in the Atmosphere. *Reviews of Geophysics*, *62*(4), e2023RG000808. https://doi.org/10.1029/2023RG000808

Pelley, R. E., Thomson, D. J., Webster, H. N., Cooke, M. C., Manning, A. J., Witham, C. S., & Hort, M. C. (2021). A Near-Real-Time Method for Estimating Volcanic Ash Emissions Using Satellite Retrievals. *Atmosphere*, *12*(12), 1573. https://doi.org/10.3390/atmos12121573

Pioli, L., Bonadonna, C., & Pistolesi, M. (2019). Reliability of Total Grain-Size Distribution of Tephra Deposits. *Scientific Reports*, *9*(1), 10006. https://doi.org/10.1038/s41598-019-46125-8

Pioli, L., & Harris, A. J. L. (2019). Real-Time Geophysical Monitoring of Particle Size Distribution During Volcanic Explosions at Stromboli Volcano (Italy). *Frontiers in Earth Science*, *7*. https://doi.org/10.3389/feart.2019.00052

Prata, F., Prata, A. T., Tanner, R., Grainger, R. G., Borgas, M., & Aubry, T. J. (2025). The radial spreading of volcanic umbrella clouds deduced from satellite measurements. *Volcanica*, *8*(1), 1–29. https://doi.org/10.30909/vol.08.01.0129

Rolph, G. D., Ngan, F., & Draxler, R. R. (2014). Modeling the fallout from stabilized nuclear clouds using the HYSPLIT atmospheric dispersion model. *Journal of Environmental Radioactivity*, *136*, 41–55. https://doi.org/10.1016/j.jenvrad.2014.05.006

Rosi, M., Bertagnini, A., Harris, A. J. L., Pioli, L., Pistolesi, M., & Ripepe, M. (2006). A case history of paroxysmal explosion at Stromboli: Timing and dynamics of the April 5, 2003 event. *Earth and Planetary Science Letters*, *243*(3), 594–606. https://doi.org/10.1016/j.epsl.2006.01.035

Saint, C., Beckett, F. M., Dioguardi, F., Kristiansen, N., & Tubbs, R. N. (2024). Using Simulated Radiances to Understand the Limitations of Satellite-Retrieved Volcanic Ash Data and the

928 Implications for Volcanic Ash Cloud Forecasting. *Journal of Geophysical Research:*
929 *Atmospheres*, *129*(23), e2024JD041112. https://doi.org/10.1029/2024JD041112
930 Sigurdsson, H., & Carey, S. (1989). Plinian and co-ignimbrite tephra fall from the 1815 eruption of
931 Tambora volcano. *Bulletin of Volcanology*, *51*(4), 243–270.
932 https://doi.org/10.1007/BF01073515
933 Sparks, R. S. J. (1986). The dimensions and dynamics of volcanic eruption columns. *Bulletin of*
934 *Volcanology*, *48*(1), 3–15. https://doi.org/10.1007/BF01073509
935 Sparks, R. S. J., Bursik, M. I., Carey, S. N., Gilbert, J. S., Glaze, L. S., Sigurdsson, H., & Woods, A.
936 W. (1997). *Volcanic plumes*. Wiley.
937 Sparks, R. S. J., Moore, J. G., & Rice, C. J. (1986). The initial giant umbrella cloud of the May 18th,
938 1980, explosive eruption of Mount St. Helens. *Journal of Volcanology and Geothermal*
939 *Research*, *28*(3), 257–274. https://doi.org/10.1016/0377-0273(86)90026-0
940 Sulpizio, R., Capra, L., Sarocchi, D., Saucedo, R., Gavilanes-Ruiz, J. C., & Varley, N. R. (2010).
941 Predicting the block-and-ash flow inundation areas at Volcán de Colima (Colima, Mexico)
942 based on the present day (February 2010) status. *Journal of Volcanology and Geothermal*
943 *Research*, *193*(1), 49–66. https://doi.org/10.1016/j.jvolgeores.2010.03.007
944 Ui, T., Matsuwo, N., Sumita, M., & Fujinawa, A. (1999). Generation of block and ash flows during
945 the 1990–1995 eruption of Unzen Volcano, Japan. *Journal of Volcanology and Geothermal*
946 *Research*, *89*(1), 123–137. https://doi.org/10.1016/S0377-0273(98)00128-0
947 Walters, D., Baran, A. J., Boutle, I., Brooks, M., Earnshaw, P., Edwards, J., Furtado, K., Hill, P., Lock,
948 A., Manners, J., Morcrette, C., Mulcahy, J., Sanchez, C., Smith, C., Stratton, R., Tennant, W.,
949 Tomassini, L., Van Weverberg, K., Vosper, S., … Zerroukat, M. (2019). The Met Office
950 Unified Model Global Atmosphere 7.0/7.1 and JULES Global Land 7.0 configurations.
951 *Geoscientific Model Development*, *12*(5), 1909–1963. https://doi.org/10.5194/gmd-12-1909-
952 2019
953 Warner, S., Platt, N., & Heagy, J. F. (2004). User-Oriented Two-Dimensional Measure of
954 Effectiveness for the Evaluation of Transport and Dispersion Models. *Journal of Applied*

*Meteorology*, *43*(1), 58–73. https://doi.org/10.1175/1520-0450(2004)043%253C0058:UTMOEF%253E2.0.CO;2

Watanabe, K., Ono, K., Sakaguchi, K., Takada, A., & Hoshizumi, H. (1999). Co-ignimbrite ash-fall deposits of the 1991 eruptions of Fugen-dake, Unzen Volcano, Japan. *Journal of Volcanology and Geothermal Research*, *89*(1), 95–112. https://doi.org/10.1016/S0377-0273(98)00126-7

Webster, H. N., Devenish, B. J., Mastin, L. G., Thomson, D. J., & Van Eaton, A. R. (2020). Operational Modelling of Umbrella Cloud Growth in a Lagrangian Volcanic Ash Transport and Dispersion Model. *Atmosphere*, *11*(2), Article 2. https://doi.org/10.3390/atmos11020200

Webster, H. N., Thomson, D. J., Johnson, B. T., Heard, I. P. C., Turnbull, K., Marenco, F., Kristiansen, N. I., Dorsey, J., Minikin, A., Weinzierl, B., Schumann, U., Sparks, R. S. J., Loughlin, S. C., Hort, M. C., Leadbetter, S. J., Devenish, B. J., Manning, A. J., Witham, C. S., Haywood, J. M., & Golding, B. W. (2012). Operational prediction of ash concentrations in the distal volcanic cloud from the 2010 Eyjafjallajökull eruption. *Journal of Geophysical Research: Atmospheres*, *117*(D20). https://doi.org/10.1029/2011JD016790

Webster, H. N., Whitehead, T., & Thomson, D. J. (2018). Parameterizing Unresolved Mesoscale Motions in Atmospheric Dispersion Models. *Journal of Applied Meteorology and Climatology*, *57*(3), 645–657. https://doi.org/10.1175/JAMC-D-17-0075.1

Wilson, L., Sparks, R. S. J., Huang, T. C., & Watkins, N. D. (1978). The control of volcanic column heights by eruption energetics and dynamics. *Journal of Geophysical Research: Solid Earth*, *83*(B4), 1829–1836. https://doi.org/10.1029/JB083iB04p01829

Witham, C., Webster, H., Hort, M., Jones, A., & Thomson, D. (2012). Modelling concentrations of volcanic ash encountered by aircraft in past eruptions. *Atmospheric Environment*, *48*, 219–229. https://doi.org/10.1016/j.atmosenv.2011.06.073

Woods, A. W., & Kienle, J. (1994). The dynamics and thermodynamics of volcanic clouds: Theory and observations from the april 15 and april 21, 1990 eruptions of redoubt volcano, Alaska. *Journal of Volcanology and Geothermal Research*, *62*(1), 273–299. https://doi.org/10.1016/0377-0273(94)90037-X

982 Woods, A. W., & Wohletz, K. (1991). Dimensions and dynamics of co-ignimbrite eruption columns.
983 *Nature*, *350*(6315), 225–227. https://doi.org/10.1038/350225a0
984 Zidikheri, M. J., Lucas, C., & Potts, R. J. (2017). Estimation of optimal dispersion model source
985 parameters using satellite detections of volcanic ash. *Journal of Geophysical Research:*
986 *Atmospheres*, *122*(15), 8207–8232. https://doi.org/10.1002/2017JD026676
987

*Journal of Geophysical Research: Atmospheres*

Supporting Information for

# 'Modelling the transport and dispersion of volcanic co-PDC ash clouds using NAME: an evaluation of source geometry and mass eruption rate'

M. Hagenbourger[1], F. M. Beckett[2], T. J. Jones[1], and S. L. Engwell[3]

[1] *Lancaster Environment Centre, Lancaster University, Lancaster, United Kingdom*
[2] *Met Office, Exeter, United Kingdom*
[3] *British Geological Survey, The Lyell Centre, Edinburgh, United Kingdom*

## Contents of this file

**Figure S53 - S58:** Weather pattern 8. NAME outputs from numerical experiment 1.

## Additional Supporting Information (Files uploaded to: `https://doi.org/10.5281/zenodo.15084579`)

**.txt-File F1.** Exemplary NAME input file '*NAME_SI_maininput.txt*'
This template can be used with NAME to reproduce all the data used for this publication. The specific parameters and changes are highlighted in Tables 3 & 4. (This specific template has been used for numerical experiment 1; run # 22).

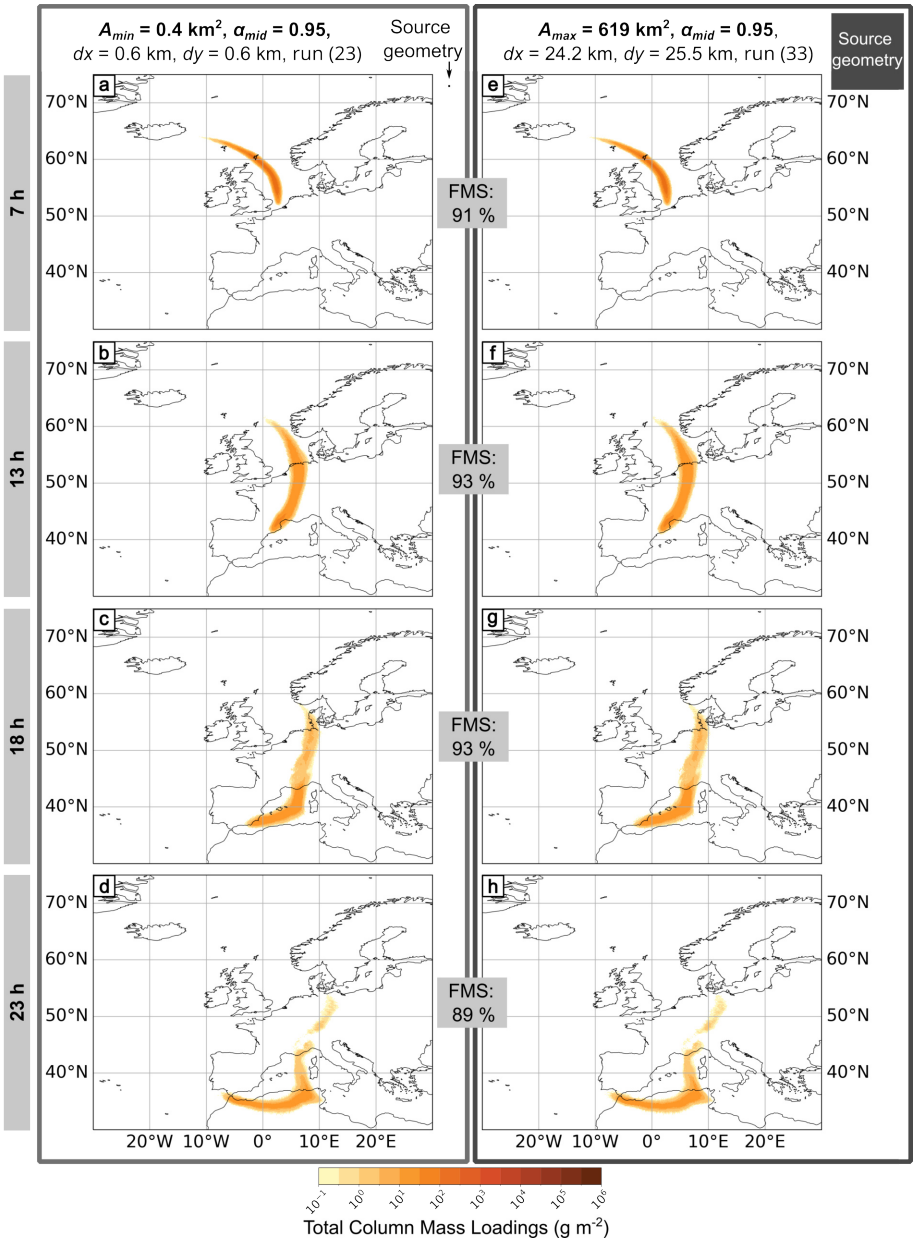


**Fig. S1**: NAME outputs for numerical experiment 1, all using $\alpha_{mid} = 0.95$, a 1 h particle release, $z = 8.5$ km, $dz = 3$ km and MER $= 1.06 \times 10^{13}$ g h$^{-1}$. The panels on the left are for the minimum source area, and the panels on the right are for the maximum. The area and orientation of the two source geometries are compared in relation to each other next to the parameter list at the top of the figure. For each area, four outputs are presented at different times after the eruption start $t_0$: **(a & e)** 7 h, **(b & f)** 13 h, **(c & g)** 18 h, and **(d & h)** 23 h. Total column mass loadings are averaged over the previous hour, and we applied a threshold of 0.2 g m$^{-2}$.

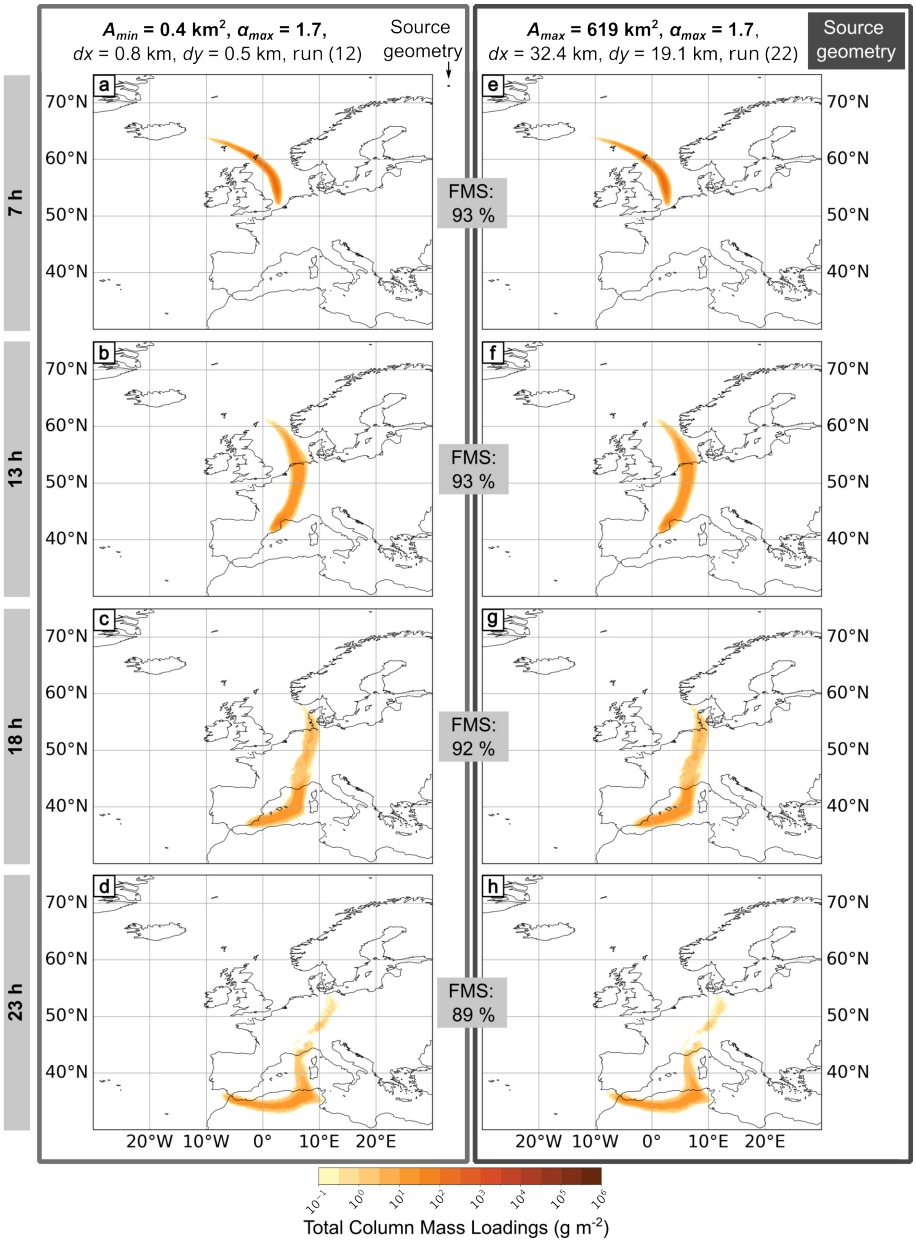


**Fig. S2**: NAME outputs for numerical experiment 1, all using $\alpha_{max} = 1.7$, a 1 h particle release, $z$ = 8.5 km, $dz$ = 3 km and MER = $1.06 \times 10^{13}$ g h$^{-1}$. The panels on the left are for the minimum source area, and the panels on the right are for the maximum. The area and orientation of the two source geometries are compared in relation to each other next to the parameter list at the top of the figure. For each area, four outputs are presented at different times after the eruption start $t_0$: **(a & e)** 7 h, **(b & f)** 13 h, **(c & g)** 18 h, and **(d & h)** 23 h. Total column mass loadings are averaged over the previous hour, and we applied a threshold of 0.2 g m$^{-2}$.

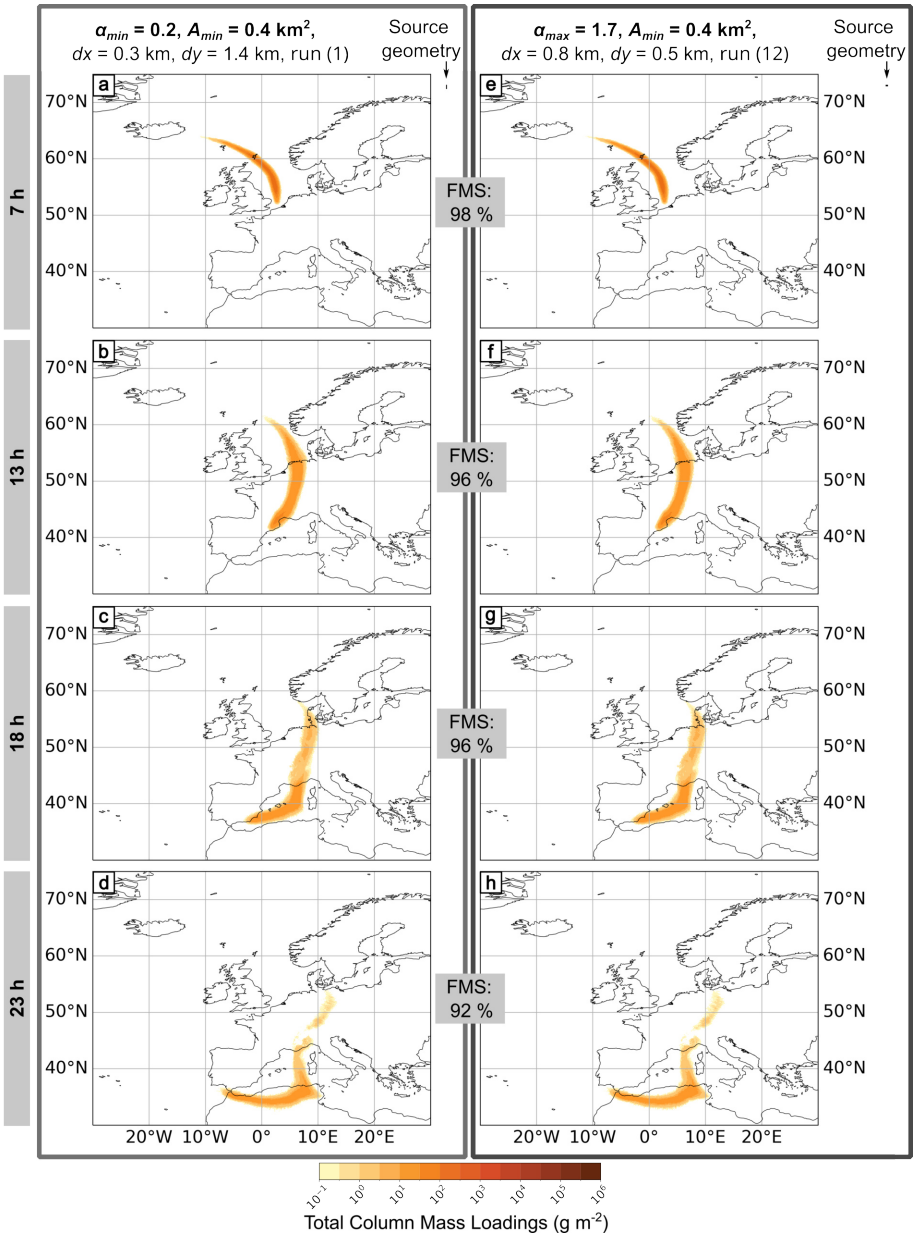


**Fig. S3**: NAME model outputs for numerical experiment 1, all using $A_{min} = 0.4\,\mathrm{km}^2$, a 1 h particle release, $z = 8.5\,\mathrm{km}$, $dz = 3\,\mathrm{km}$ and MER $= 1.06 \times 10^{13}\,\mathrm{g\,h^{-1}}$. The left figure panels **(a-d)** show results from the minimum aspect ratio $\alpha_{min} = 0.2$, and the right panels **(e-h)** show the maximum aspect ratio $\alpha_{max} = 1.7$. The area and orientation of the two source geometries are compared in relation to each other next to the parameter list at the top of the figure. For each aspect ratio, four outputs at different times after eruption start $t_0$ are shown: **(a & e)** 7 h, **(b & f)** 13 h, **(c & g)** 18 h, and **(d & h)** 23 h. Total column mass loadings are averaged over the previous hour, and we applied a threshold of $0.2\,\mathrm{g\,m^{-2}}$.

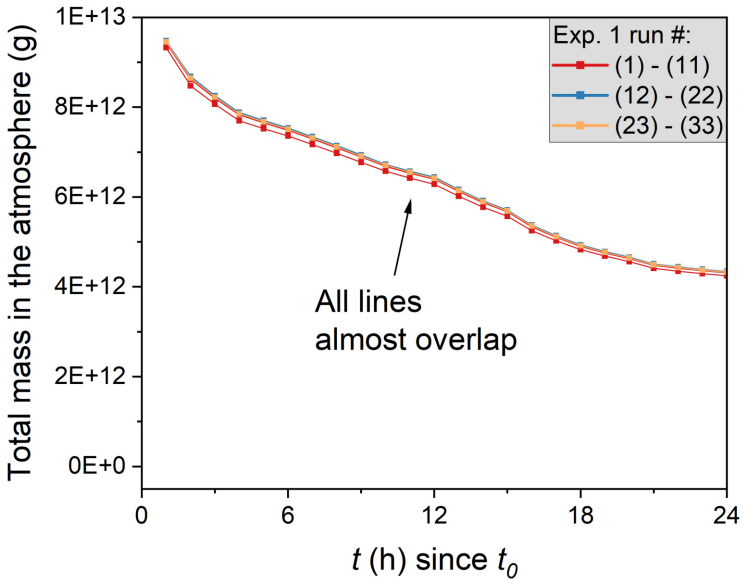


**Fig. S4**: Total mass in atmosphere for all model runs in numerical experiment 1. There are only very minor differences between model runs with different source areas and aspect ratios. The total mass in the atmosphere starts at a maximum, which is achieved after 1 h (the total time of particle emission) and then decays as wet and dry deposition (including sedimentation) occurs and no more particles are released into the atmosphere. The lines between data points are not model fits and are just used to guide the eye.

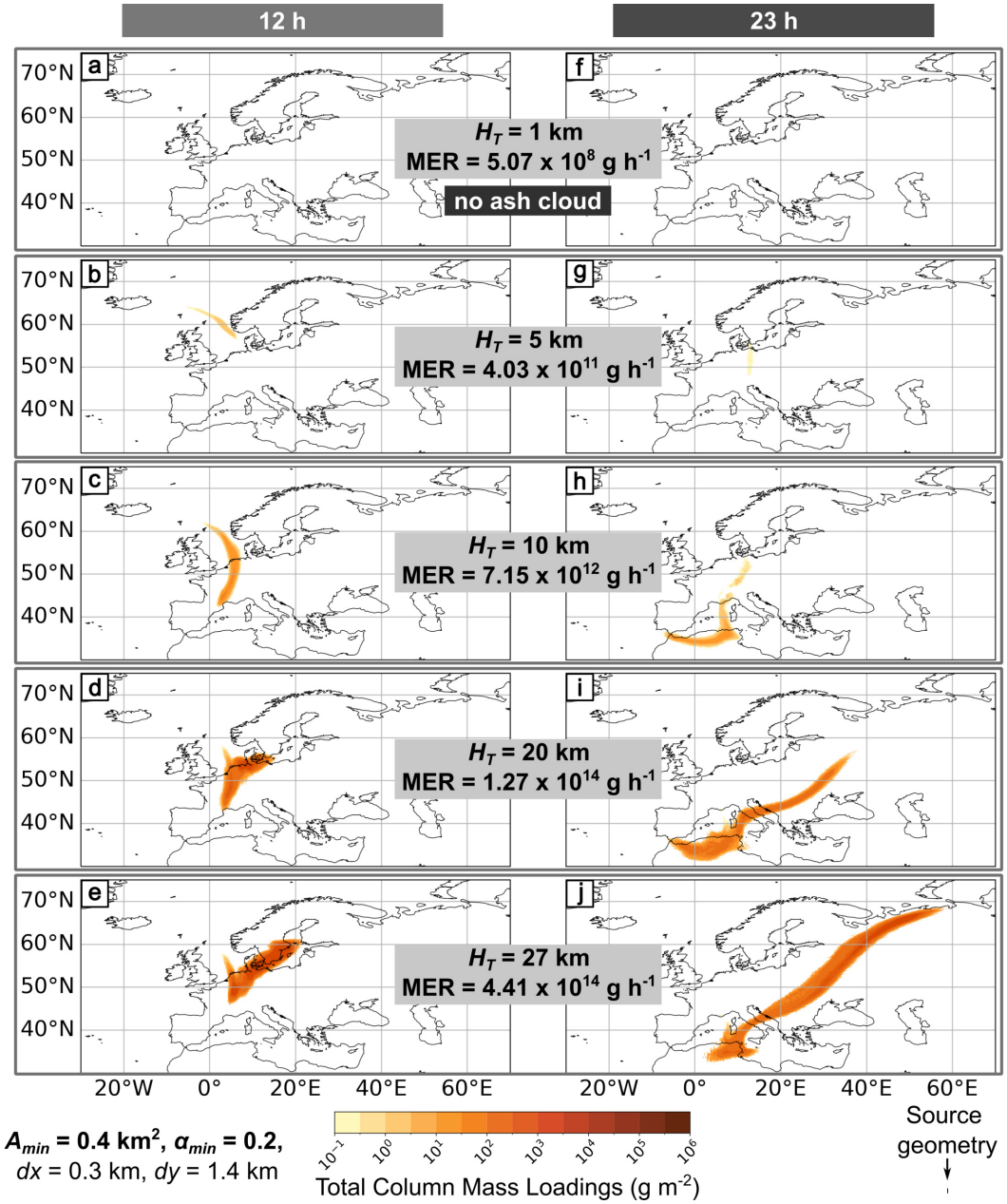


**Fig. S5**: NAME model outputs for experiment 2, all using a 1 h particle release with different $H_T$, MER, and $dz$. The figure panels on the left **(a-d)** are for 12 h after eruption start $t_0$, and the panels on the right **(e-h)** show 23 h after eruption start $t_0$. The outputs here are for $A_{min} = 0.4\,\mathrm{km}^2$ with $\alpha_{min} = 0.2$. With increasing $H_T$ and $t$ (h), the plume size grows. Total column mass loadings are averaged over the previous hour, and we applied a threshold of $0.2\,\mathrm{g\,m^{-2}}$. The subplots **(a & f)** show no ash cloud (i.e., mass loading $< 0.2\,\mathrm{g\,m^{-2}}$).

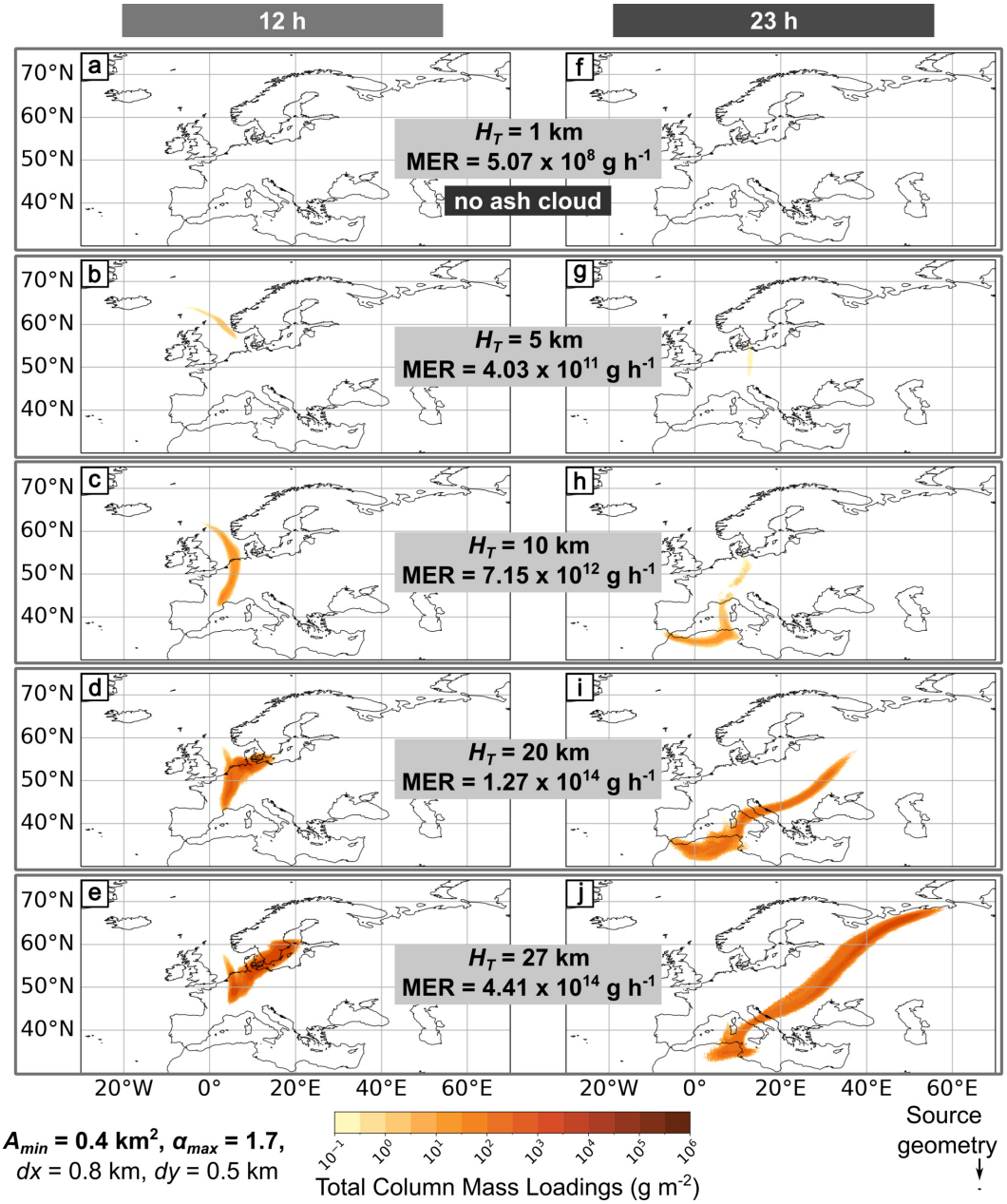


**Fig. S6**: NAME model outputs for experiment 2, all using a 1 h particle release with different $H_T$, MER, and $dz$. The figure panels on the left **(a-d)** are for 12 h after eruption start $t_0$, and the panels on the right **(e-h)** show 23 h after eruption start $t_0$. The outputs here are for $A_{min} = 0.4\,\mathrm{km}^2$ with $\alpha_{max} = 1.7$. With increasing $H_T$ and $t$ (h), the plume size grows. Total column mass loadings are averaged over the previous hour, and we applied a threshold of $0.2\,\mathrm{g\,m^{-2}}$. The subplots **(a & f)** show no ash cloud (i.e., mass loading $< 0.2\,\mathrm{g\,m^{-2}}$).

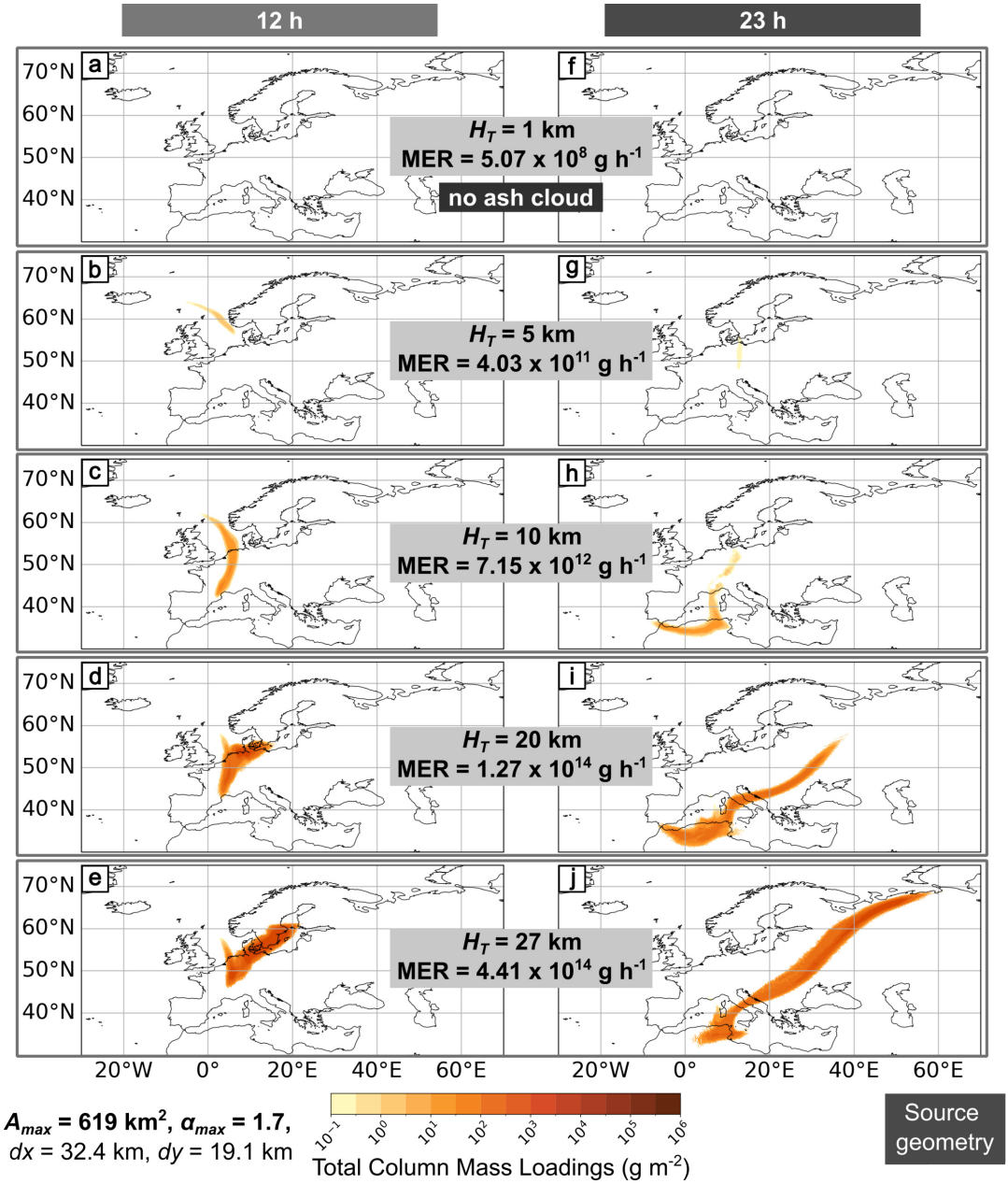


**Fig. S7**: NAME model outputs for experiment 2, all using a 1 h particle release with different $H_T$, MER, and $dz$. The figure panels on the left **(a-d)** are for 12 h after eruption start $t_0$, and the panels on the right **(e-h)** show 23 h after eruption start $t_0$. The outputs here are for $A_{max} = 619\,\mathrm{km}^2$ with $\alpha_{max} = 1.7$. With increasing $H_T$ and $t$ (h), the plume size grows. Total column mass loadings are averaged over the previous hour, and we applied a threshold of $0.2\,\mathrm{g\,m^{-2}}$. The subplots **(a & f)** show no ash cloud (i.e., mass loading $< 0.2\,\mathrm{g\,m^{-2}}$).

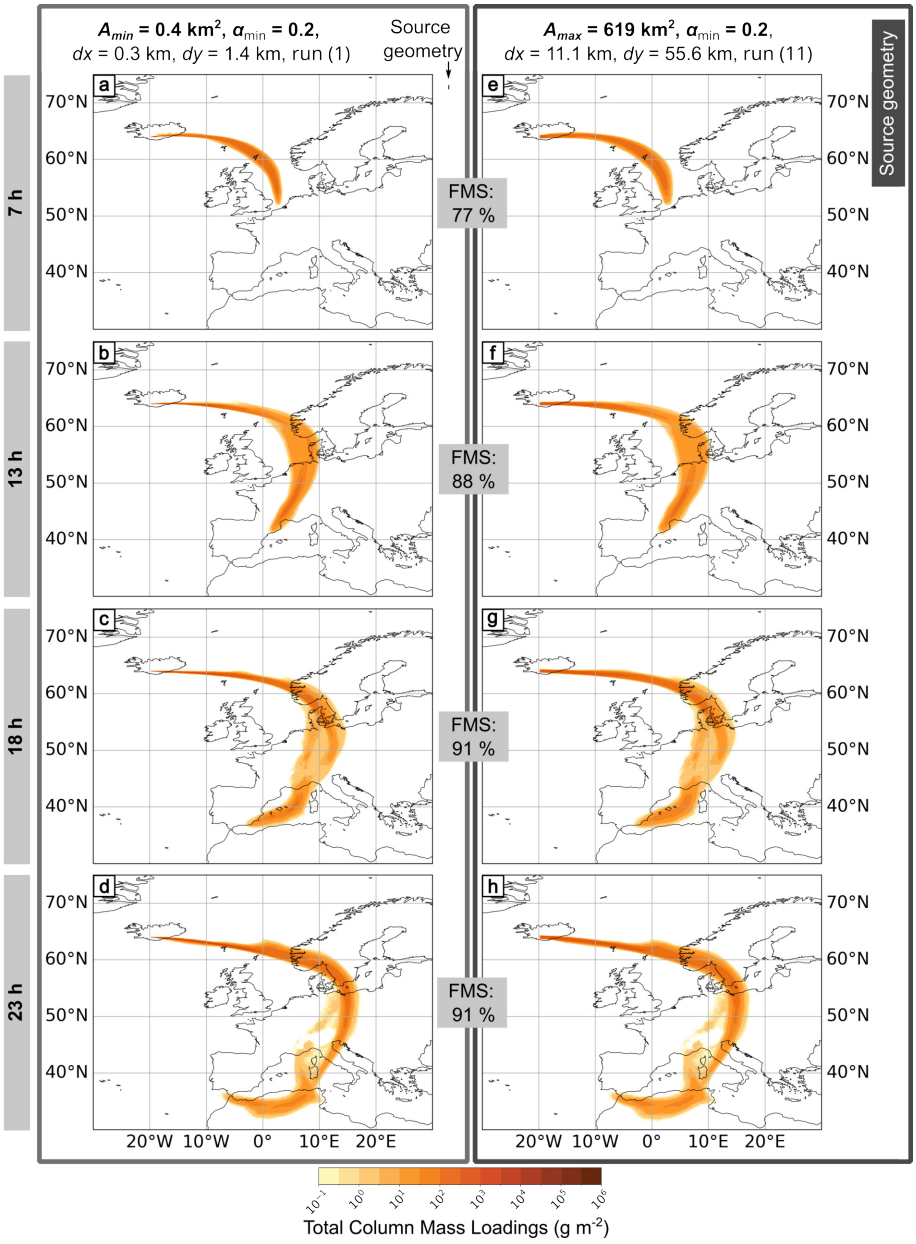


**Fig. S8**: NAME outputs for numerical experiment 1, all using $\alpha_{min} = 0.2$, a 24 h particle release, $z = 8.5$ km, $dz = 3$ km and MER $= 1.06 \times 10^{13}$ g h$^{-1}$. The panels on the left are for the minimum source area, and the panels on the right are for the maximum. The area and orientation of the two source geometries are compared in relation to each other next to the parameter list at the top of the figure. For each area, four outputs are presented at different times after the eruption start $t_0$: **(a & e)** 7 h, **(b & f)** 13 h, **(c & g)** 18 h, and **(d & h)** 23 h. Total column mass loadings are averaged over the previous hour, and we applied a threshold of 0.2 g m$^{-2}$.

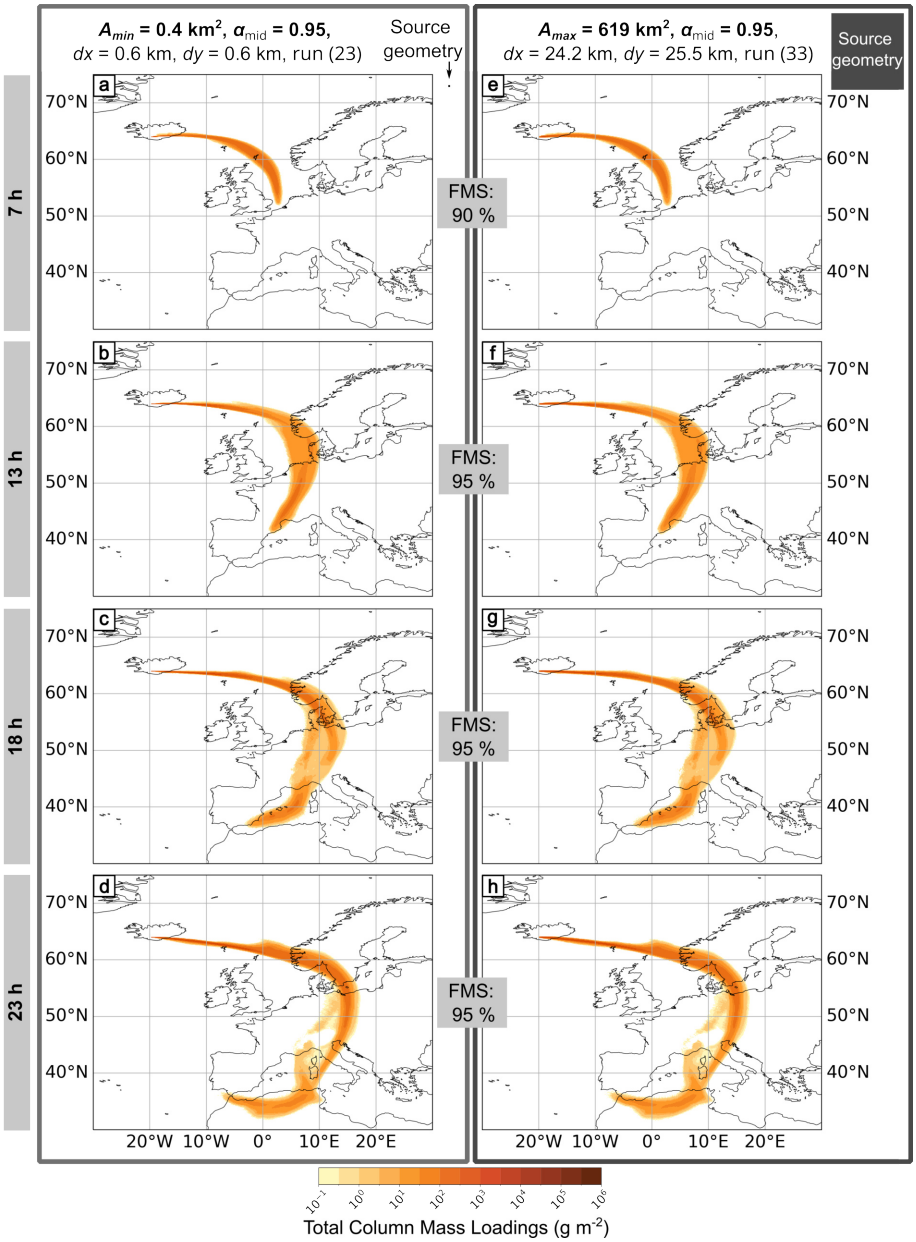


**Fig. S9**: NAME outputs for numerical experiment 1, all using $\alpha_{mid} = 0.95$, a 24 h particle release, $z = 8.5$ km, $dz = 3$ km and MER $= 1.06 \times 10^{13}$ g h$^{-1}$. The panels on the left are for the minimum source area, and the panels on the right are for the maximum. The area and orientation of the two source geometries are compared in relation to each other next to the parameter list at the top of the figure. For each area, four outputs are presented at different times after the eruption start $t_0$: **(a & e)** 7 h, **(b & f)** 13 h, **(c & g)** 18 h, and **(d & h)** 23 h. Total column mass loadings are averaged over the previous hour, and we applied a threshold of 0.2 g m$^{-2}$.

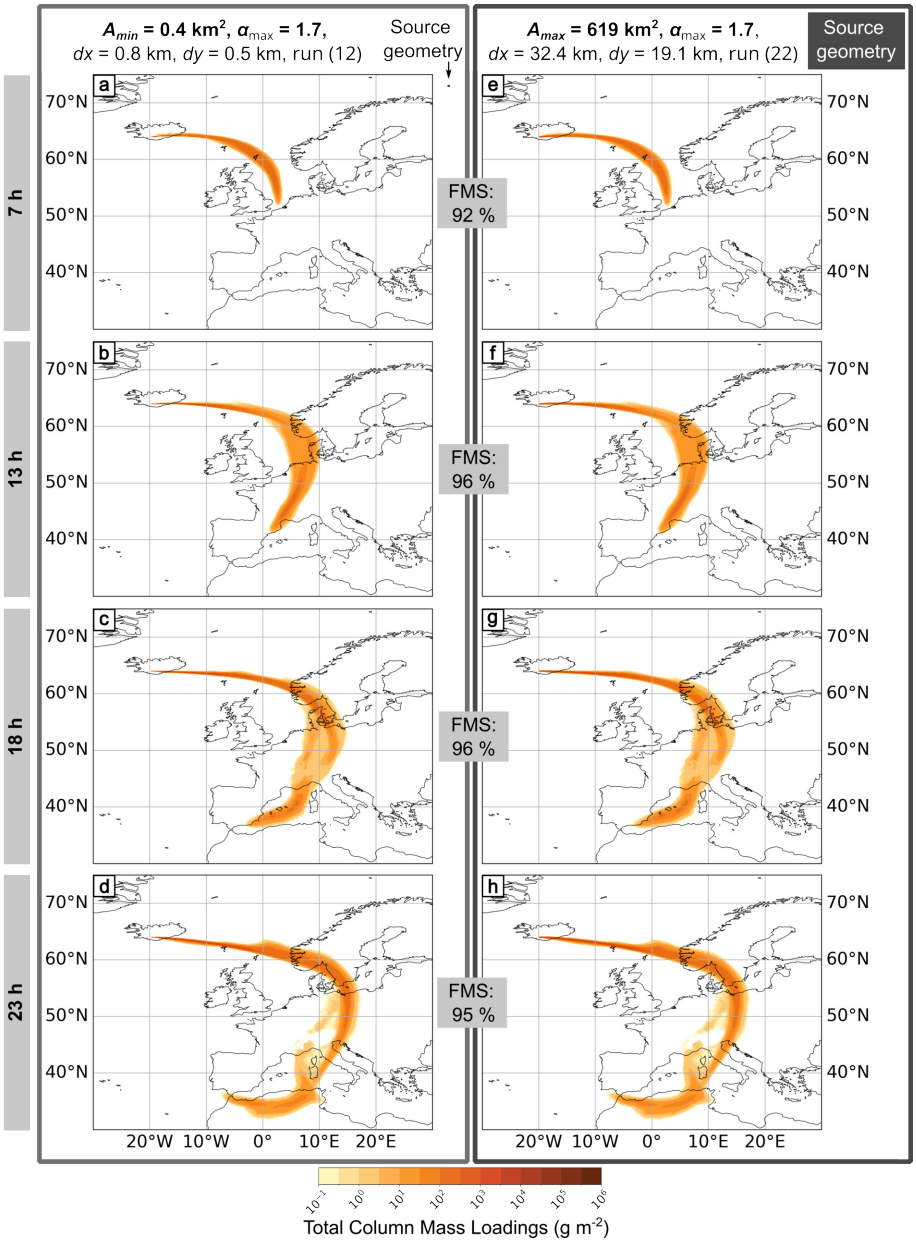


**Fig. S10**: NAME outputs for numerical experiment 1, all using $\alpha_{max} = 1.7$, a 24 h particle release, $z = 8.5$ km, $dz = 3$ km and MER $= 1.06 \times 10^{13}$ g h$^{-1}$. The panels on the left are for the minimum source area, and the panels on the right are for the maximum. The area and orientation of the two source geometries are compared in relation to each other next to the parameter list at the top of the figure. For each area, four outputs are presented at different times after the eruption start $t_0$: **(a & e)** 7 h, **(b & f)** 13 h, **(c & g)** 18 h, and **(d & h)** 23 h. Total column mass loadings are averaged over the previous hour, and we applied a threshold of 0.2 g m$^{-2}$.

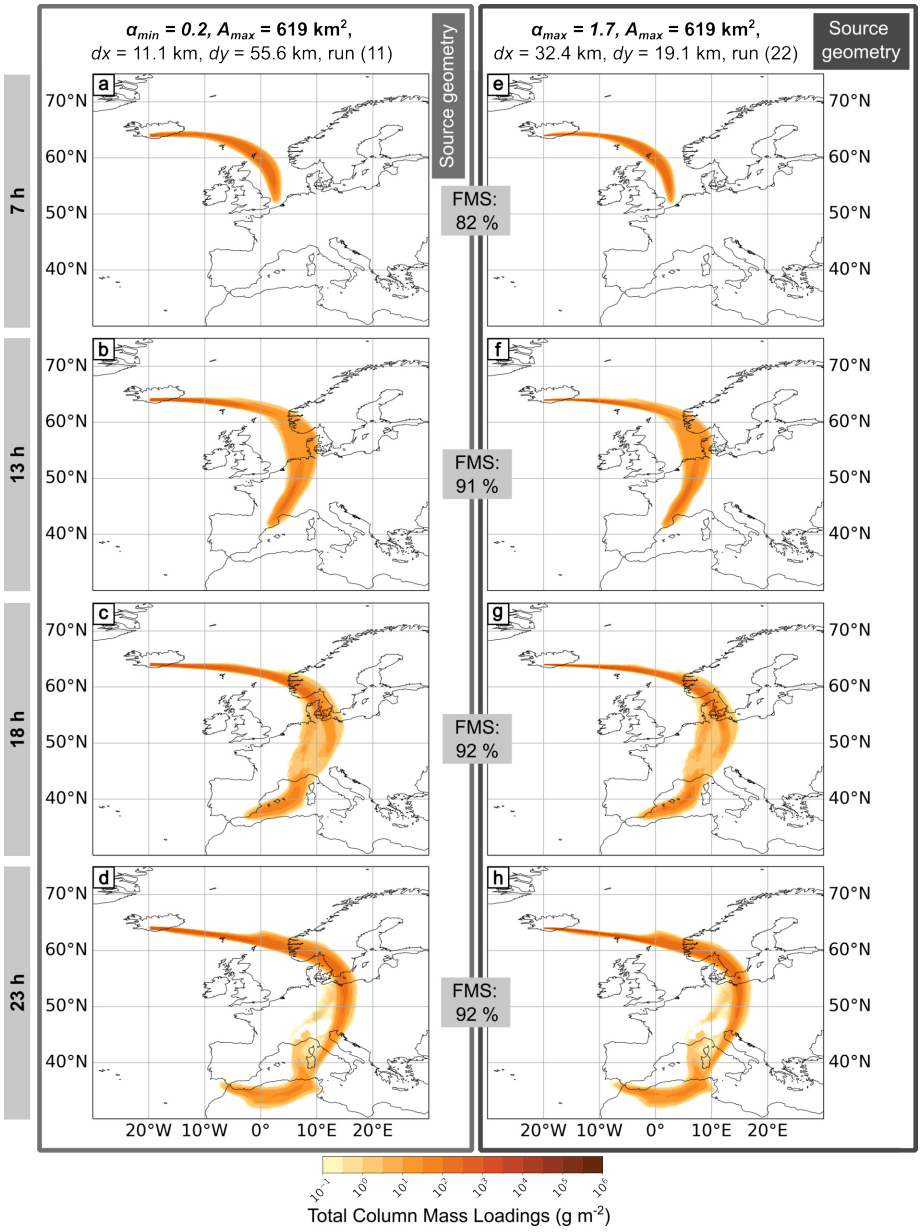


**Fig. S11**: NAME model outputs for numerical experiment 1, all using $A_{max} = 619\,\mathrm{km}^2$, a 24 h particle release, $z = 8.5\,\mathrm{km}$, $dz = 3\,\mathrm{km}$ and MER $= 1.06 \times 10^{13}\,\mathrm{g\,h^{-1}}$. The left figure panels **(a-d)** show results from the minimum aspect ratio $\alpha_{min} = 0.2$, and the right panels **(e-h)** show the maximum aspect ratio $\alpha_{max} = 1.7$. The area and orientation of the two source geometries are compared in relation to each other next to the parameter list at the top of the figure. For each aspect ratio, four outputs at different times after eruption start $t_0$ are shown: **(a & e)** 7 h, **(b & f)** 13 h, **(c & g)** 18 h, and **(d & h)** 23 h. Total column mass loadings are averaged over the previous hour, and we applied a threshold of $0.2\,\mathrm{g\,m^{-2}}$.

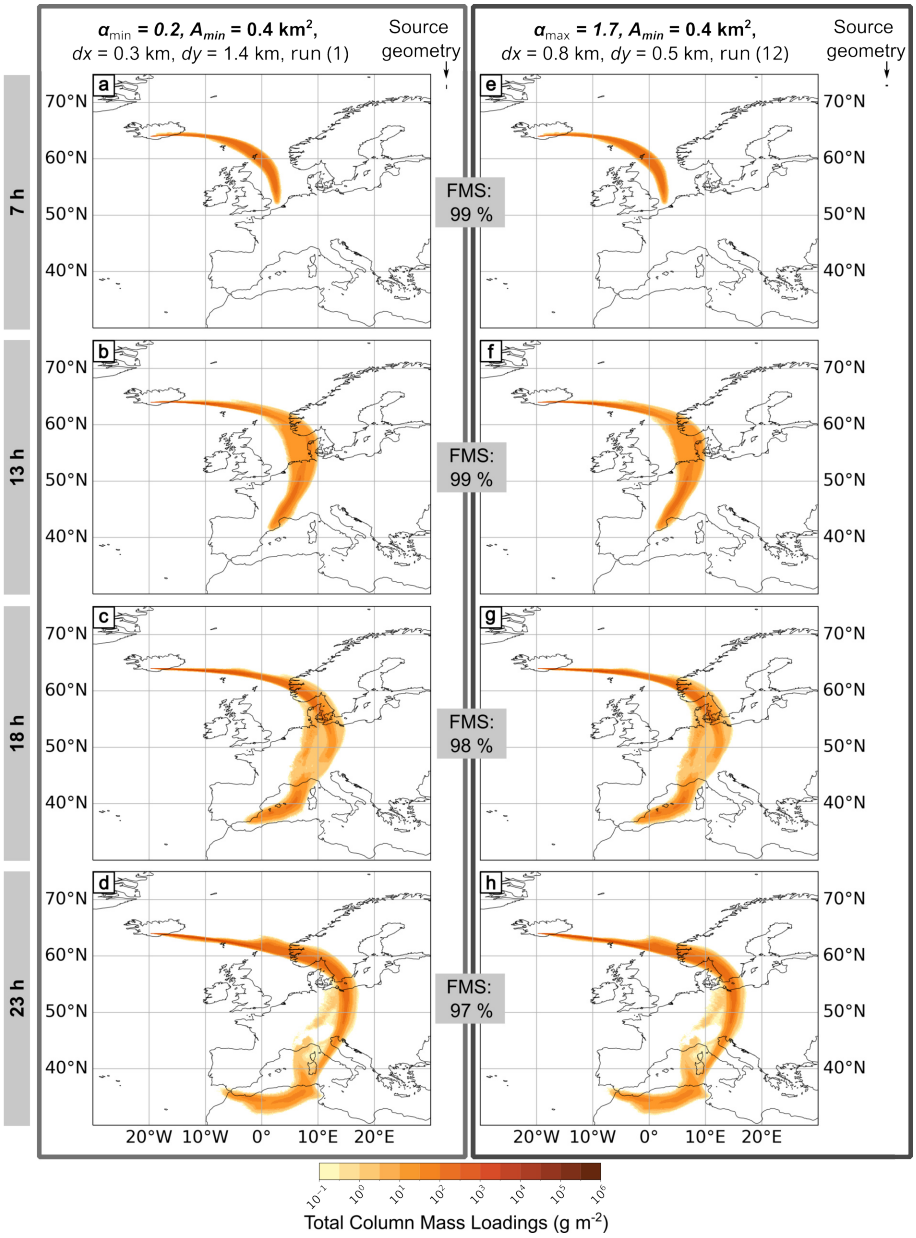


**Fig. S12**: NAME model outputs for numerical experiment 1, all using $A_{min} = 0.4\,\mathrm{km}^2$, a 24 h particle release, $z = 8.5\,\mathrm{km}$, $dz = 3\,\mathrm{km}$ and MER $= 1.06 \times 10^{13}\,\mathrm{g\,h}^{-1}$. The left figure panels **(a-d)** show results from the minimum aspect ratio $\alpha_{min} = 0.2$, and the right panels **(e-h)** show the maximum aspect ratio $\alpha_{max} = 1.7$. The area and orientation of the two source geometries are compared in relation to each other next to the parameter list at the top of the figure. For each aspect ratio, four outputs at different times after eruption start $t_0$ are shown: **(a & e)** 7 h, **(b & f)** 13 h, **(c & g)** 18 h, and **(d & h)** 23 h. Total column mass loadings are averaged over the previous hour, and we applied a threshold of $0.2\,\mathrm{g\,m}^{-2}$.

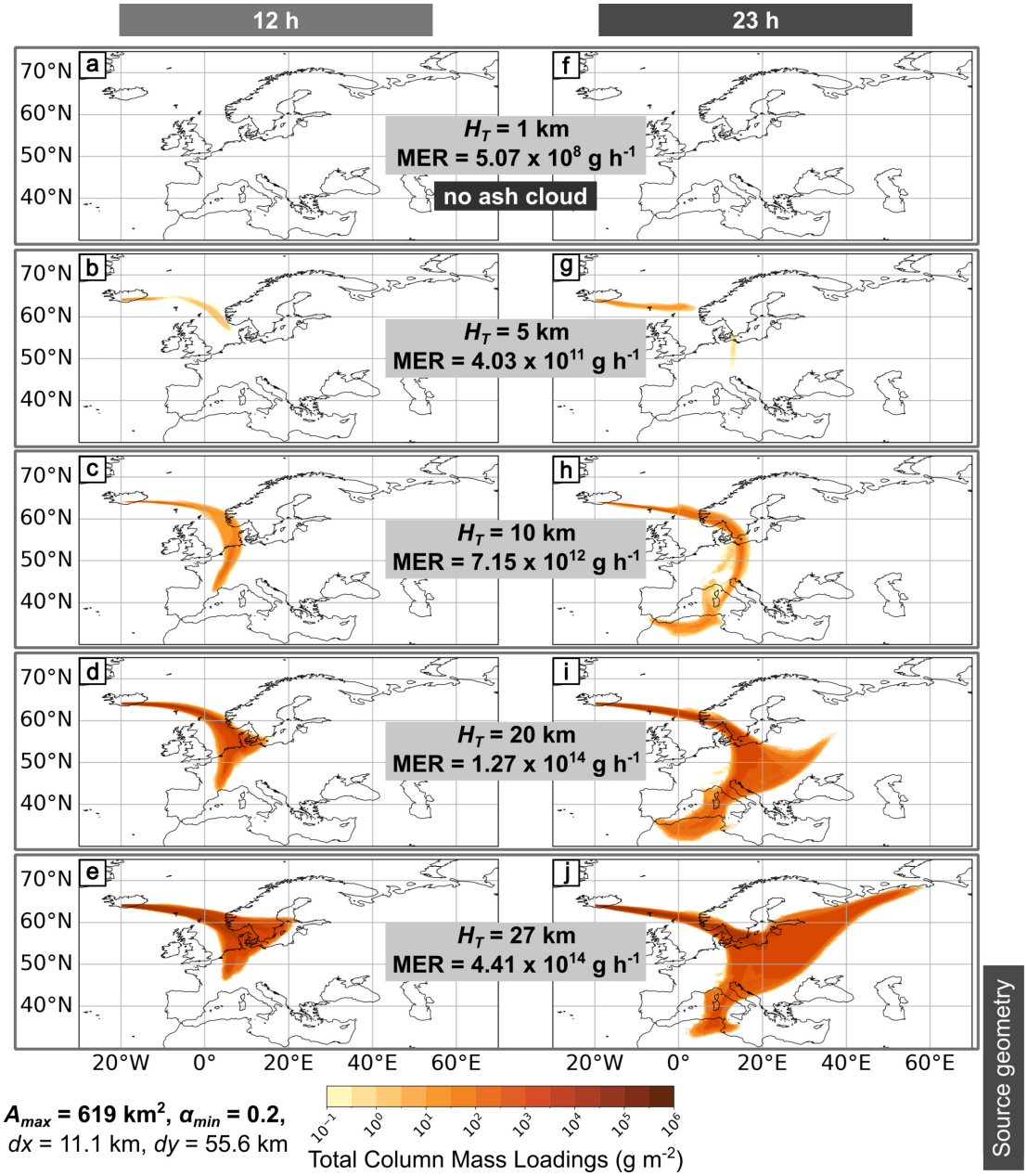


**Fig. S13**: NAME model outputs for experiment 2, all using a 24 h particle release with different $H_T$, MER, and $dz$. The figure panels on the left **(a-d)** are for 12 h after eruption start $t_0$, and the panels on the right **(e-h)** show 23 h after eruption start $t_0$. The outputs here are for $A_{max}$ = 619 km$^2$ with $\alpha_{min}$ = 0.2. With increasing $H_T$ and $t$ (h), the plume size grows. Total column mass loadings are averaged over the previous hour, and we applied a threshold of 0.2 g m$^{-2}$. The subplots **(a & f)** show no ash cloud (i.e., mass loading $< 0.2$ g m$^{-2}$).

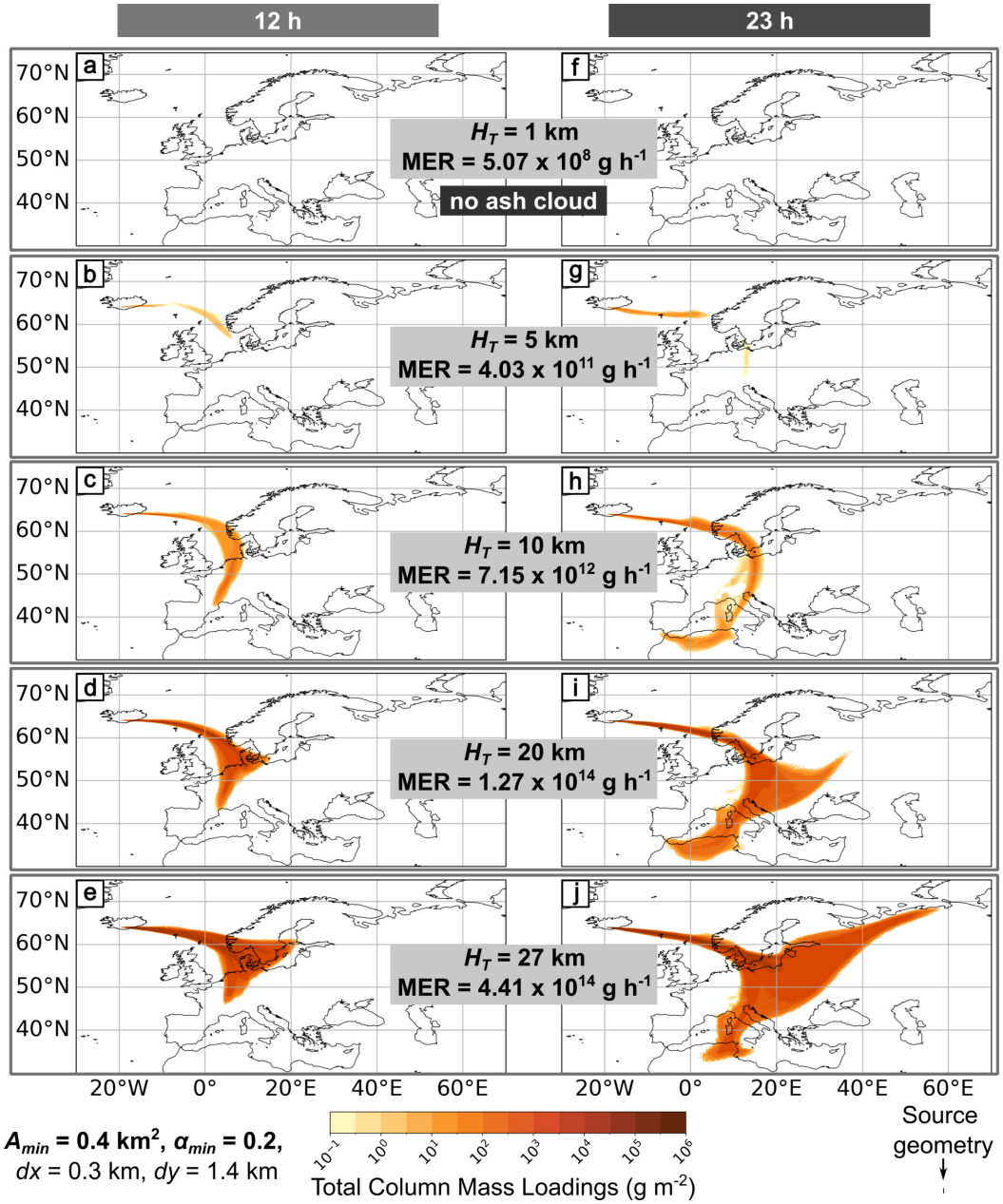


**Fig. S14**: NAME model outputs for experiment 2, all using a 24 h particle release different $H_T$, MER, and $dz$. The figure panels on the left **(a-d)** are for 12 h after eruption start $t_0$, and the panels on the right **(e-h)** show 23 h after eruption start $t_0$. The outputs here are for $A_{min} = 0.4\,\mathrm{km}^2$ with $\alpha_{min} = 0.2$. With increasing $H_T$ and $t$ (h), the plume size grows. Total column mass loadings are averaged over the previous hour, and we applied a threshold of $0.2\,\mathrm{g\,m^{-2}}$. The subplots **(a & f)** show no ash cloud (i.e., mass loading $< 0.2\,\mathrm{g\,m^{-2}}$).

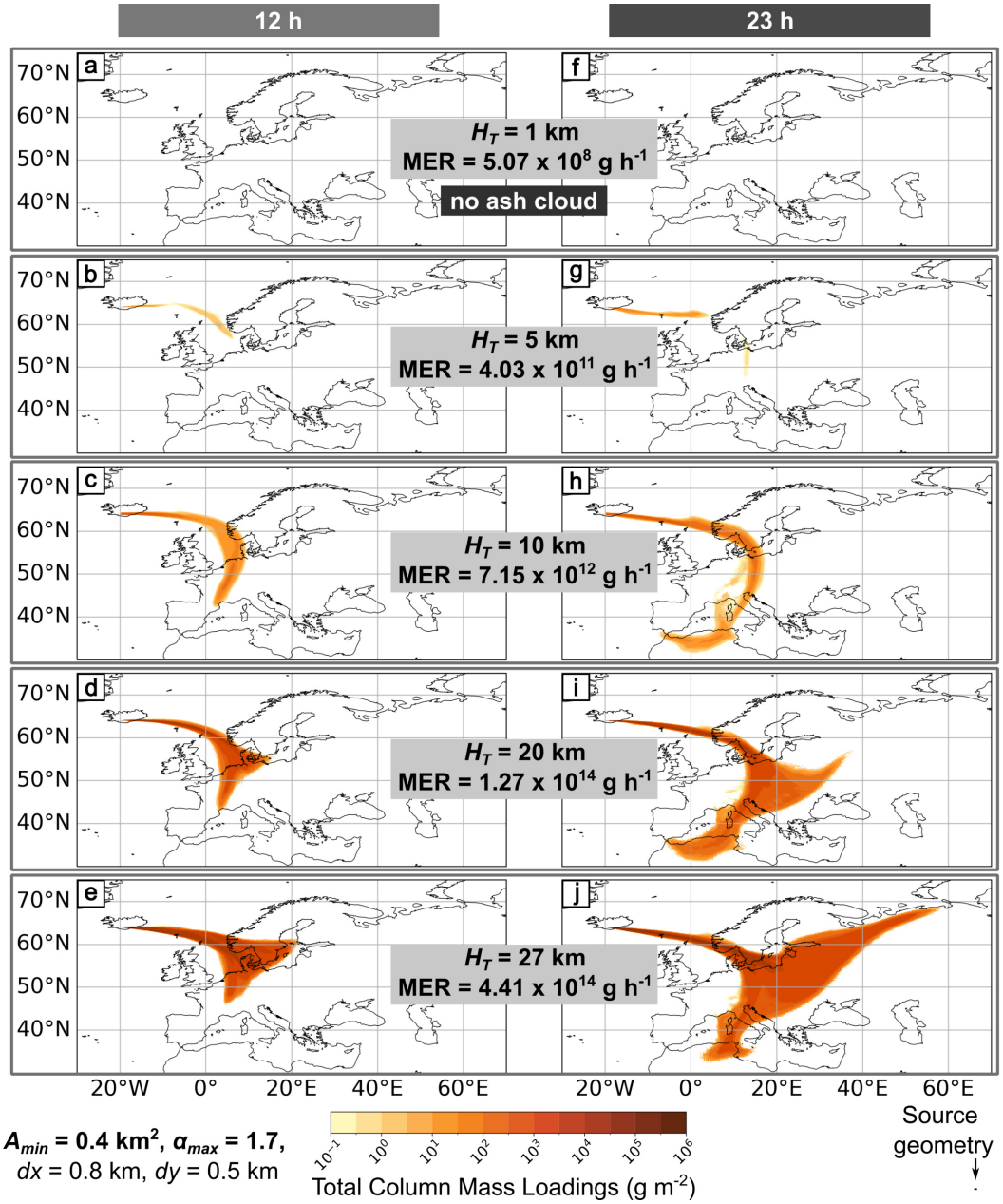


**Fig. S15**: NAME model outputs for experiment 2, all using a 24 h particle release different $H_T$, MER, and $dz$. The figure panels on the left **(a-d)** are for 12 h after eruption start t0, and the panels on the right **(e-h)** show 23 h after eruption start $t_0$. The outputs here are for $A_{min} = 0.4\,\mathrm{km}^2$ with $\alpha_{max} = 1.7$. With increasing $H_T$ and $t$ (h), the plume size grows. Total column mass loadings are averaged over the previous hour, and we applied a threshold of $0.2\,\mathrm{g\,m^{-2}}$. The subplots **(a & f)** show no ash cloud (i.e., mass loading $< 0.2\,\mathrm{g\,m^{-2}}$).

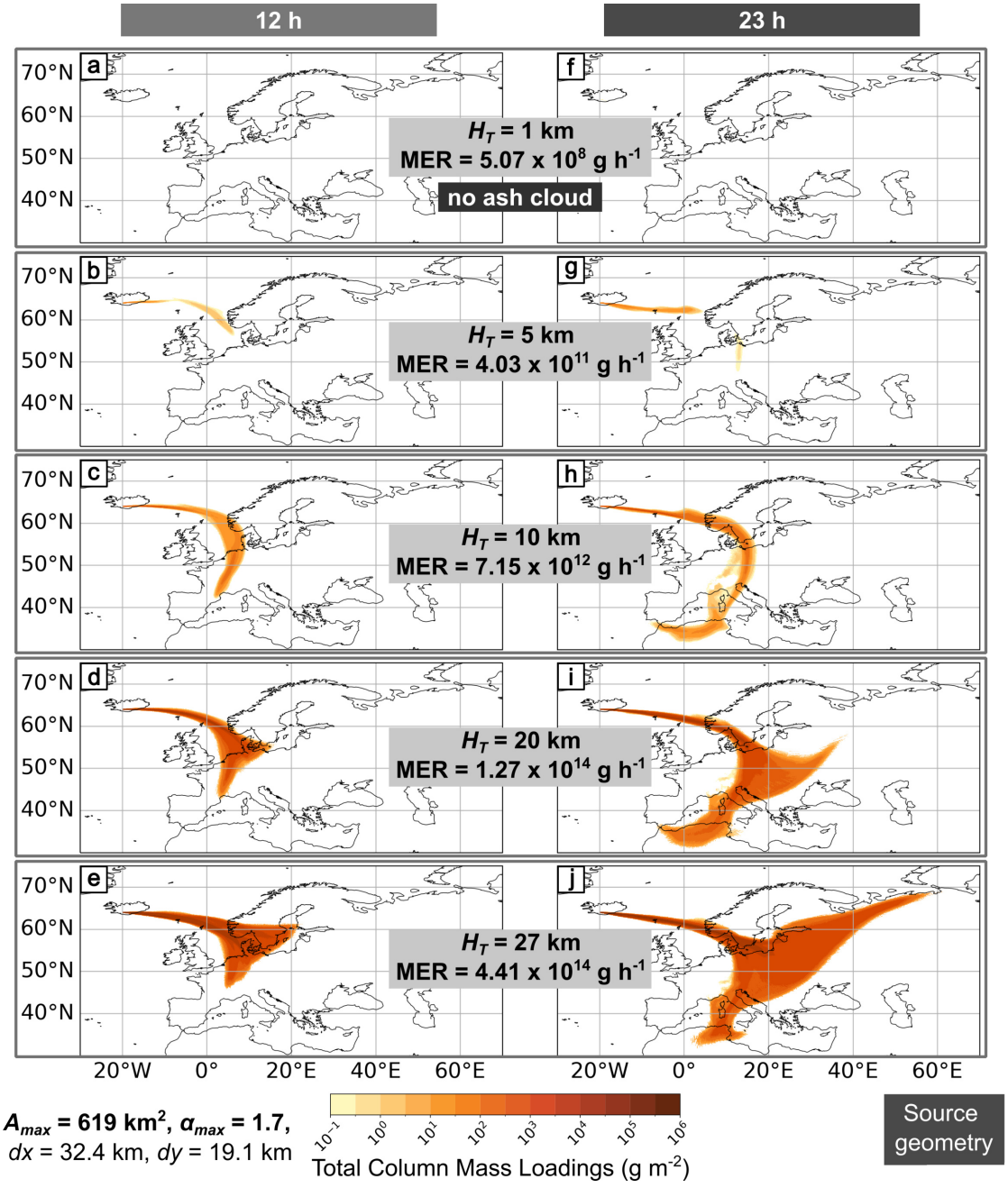


**Fig. S16**: NAME model outputs for experiment 2, all using a 24 h particle release different $H_T$, MER, and $dz$. The figure panels on the left **(a-d)** are for 12 h after eruption start $t_0$, and the panels on the right **(e-h)** show 23 h after eruption start $t_0$. The outputs here are for $A_{max} = 619\,\mathrm{km}^2$ with $\alpha_{max} = 1.7$. With increasing $H_T$ and $t$ (h), the plume size grows. Total column mass loadings are averaged over the previous hour, and we applied a threshold of $0.2\,\mathrm{g\,m^{-2}}$. The subplots **(a & f)** show no ash cloud (i.e., mass loading $< 0.2\,\mathrm{g\,m^{-2}}$).

**Table S1**: Date manually chosen per each weather pattern. Each weather pattern describes a different weather circulation type defined for the UK and surrounding European area.

| **Weather pattern** | **Day** | **Month** | **Year** |
|---|---|---|---|
| 1 | 25 | 12 | 2021 |
| 2 | 11 | 3 | 2019 |
| 3 | 31 | 1 | 2022 |
| 4 | 29 | 11 | 2018 |
| 5 | 16 | 4 | 2022 |
| 6 | 31 | 5 | 2019 |
| 7 | 13 | 6 | 2017 |
| 8 | 7 | 9 | 2020 |

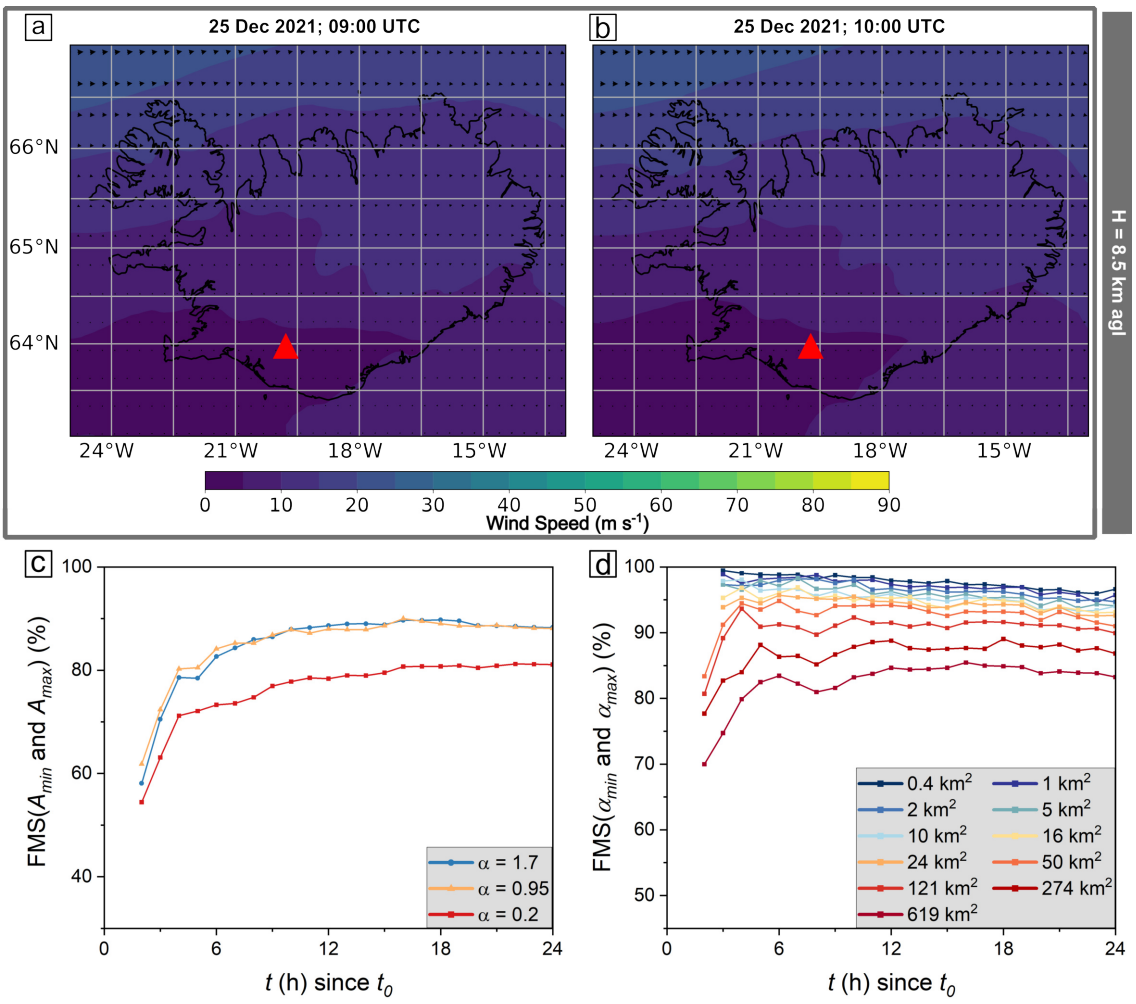


**Fig. S17**: Meteorological data for Iceland for weather pattern 1 at 8.5 km agl elevation at times **(a)** 09:00 UTC and **(b)** 10:00 UTC. The Figure of Merit in space (FMS) determined by Equation 9, shown **(c)** between the plumes generated using the minimum ($A_{min}$) and maximum ($A_{max}$) source area and **(d)** between the minimum ($\alpha_{min}$) and maximum ($\alpha_{max}$) aspect ratio.

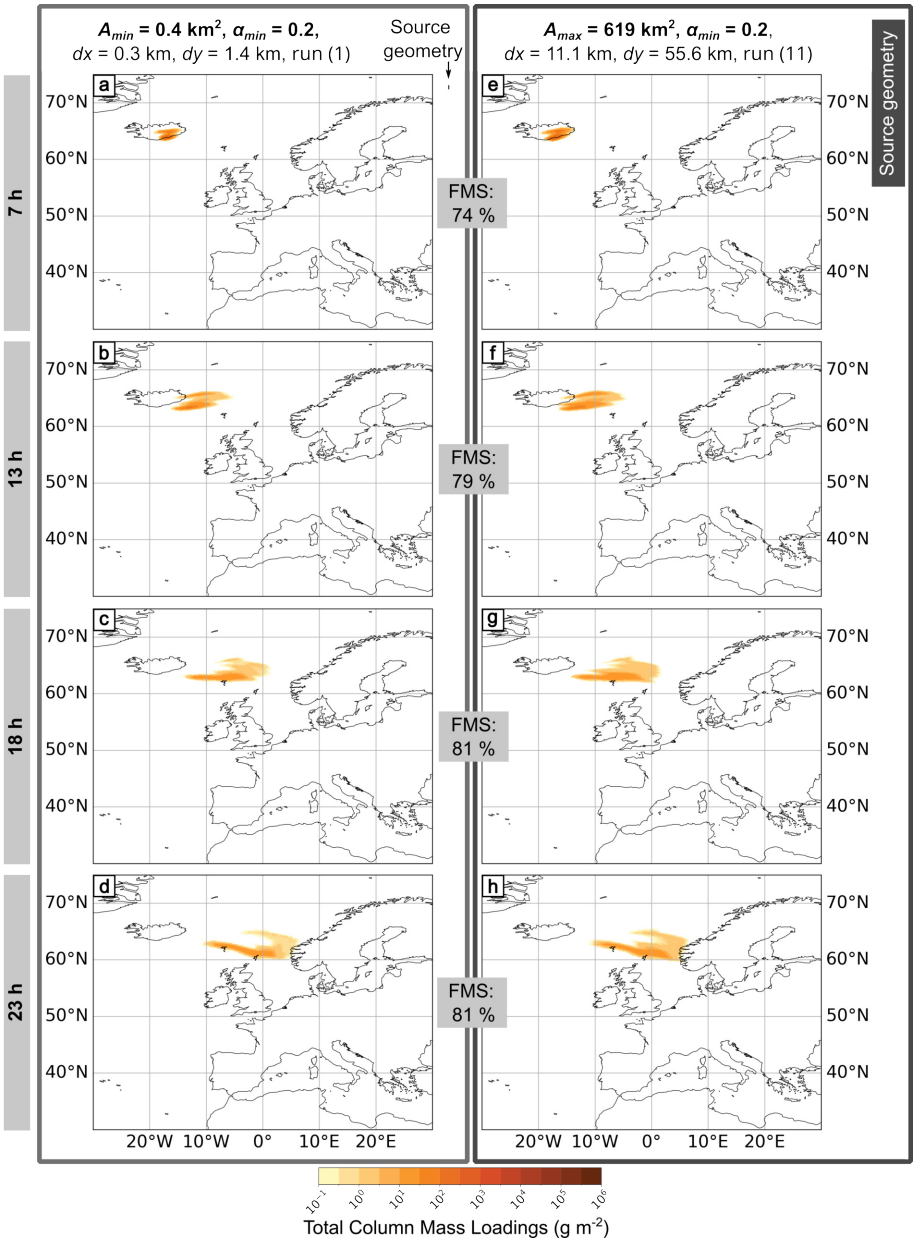


**Fig. S18**: Weather pattern 1. NAME outputs for numerical experiment 1, all using $\alpha_{min} = 0.2$, a 1 h particle release, $z = 8.5$ km, $dz = 3$ km and MER $= 1.06 \times 10^{13}$ g h$^{-1}$. The panels on the left are for the minimum source area, and the panels on the right are for the maximum. The area and orientation of the two source geometries are compared in relation to each other next to the parameter list at the top of the figure. For each area, four outputs are presented at different times after the eruption start $t_0$: **(a & e)** 7 h, **(b & f)** 13 h, **(c & g)** 18 h, and **(d & h)** 23 h. Total column mass loadings are averaged over the previous hour, and we applied a threshold of 0.2 g m$^{-2}$.

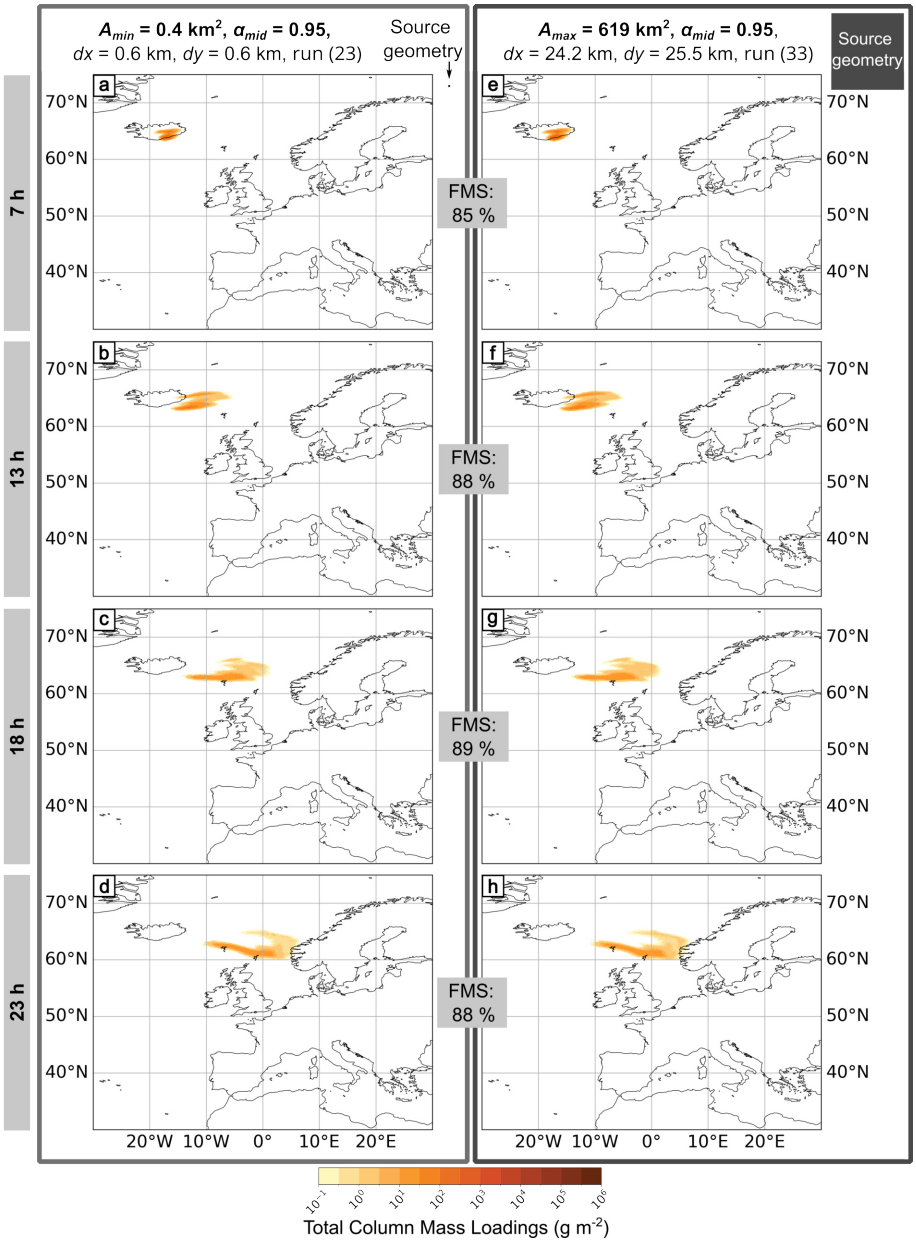


**Fig. S19**: Weather pattern 1. NAME outputs for numerical experiment 1, all using $\alpha_{mid} = 0.95$, a 1 h particle release, $z = 8.5$ km, $dz = 3$ km and MER $= 1.06 \times 10^{13}$ g h$^{-1}$. The panels on the left are for the minimum source area, and the panels on the right are for the maximum. The area and orientation of the two source geometries are compared in relation to each other next to the parameter list at the top of the figure. For each area, four outputs are presented at different times after the eruption start $t_0$: **(a & e)** 7 h, **(b & f)** 13 h, **(c & g)** 18 h, and **(d & h)** 23 h. Total column mass loadings are averaged over the previous hour, and we applied a threshold of 0.2 g m$^{-2}$.

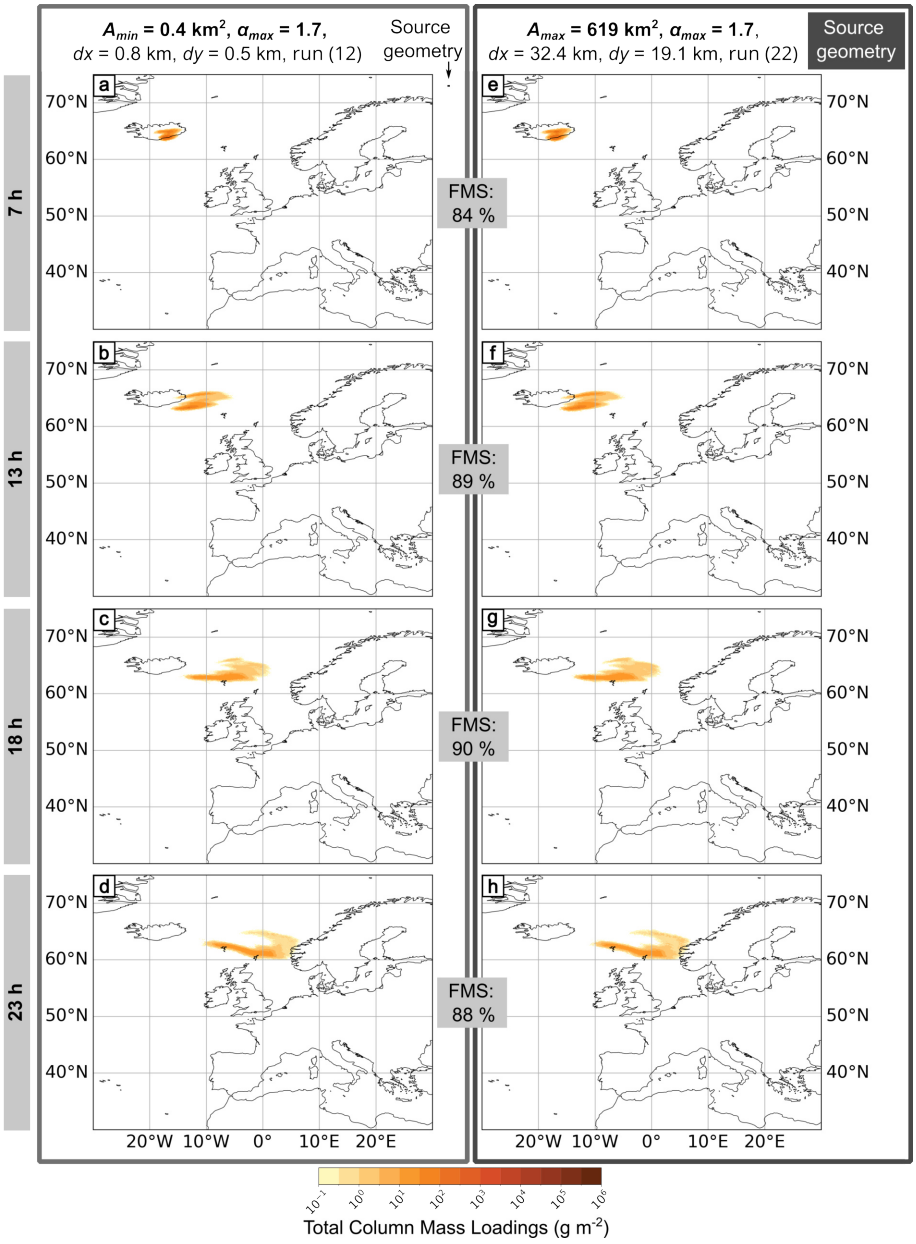


**Fig. S20**: Weather pattern 1. NAME outputs for numerical experiment 1, all using $\alpha_{max} = 1.7$, a 1 h particle release, $z = 8.5$ km, $dz = 3$ km and MER $= 1.06 \times 10^{13}$ g h$^{-1}$. The panels on the left are for the minimum source area, and the panels on the right are for the maximum. The area and orientation of the two source geometries are compared in relation to each other next to the parameter list at the top of the figure. For each area, four outputs are presented at different times after the eruption start $t_0$: **(a & e)** 7 h, **(b & f)** 13 h, **(c & g)** 18 h, and **(d & h)** 23 h. Total column mass loadings are averaged over the previous hour, and we applied a threshold of 0.2 g m$^{-2}$.

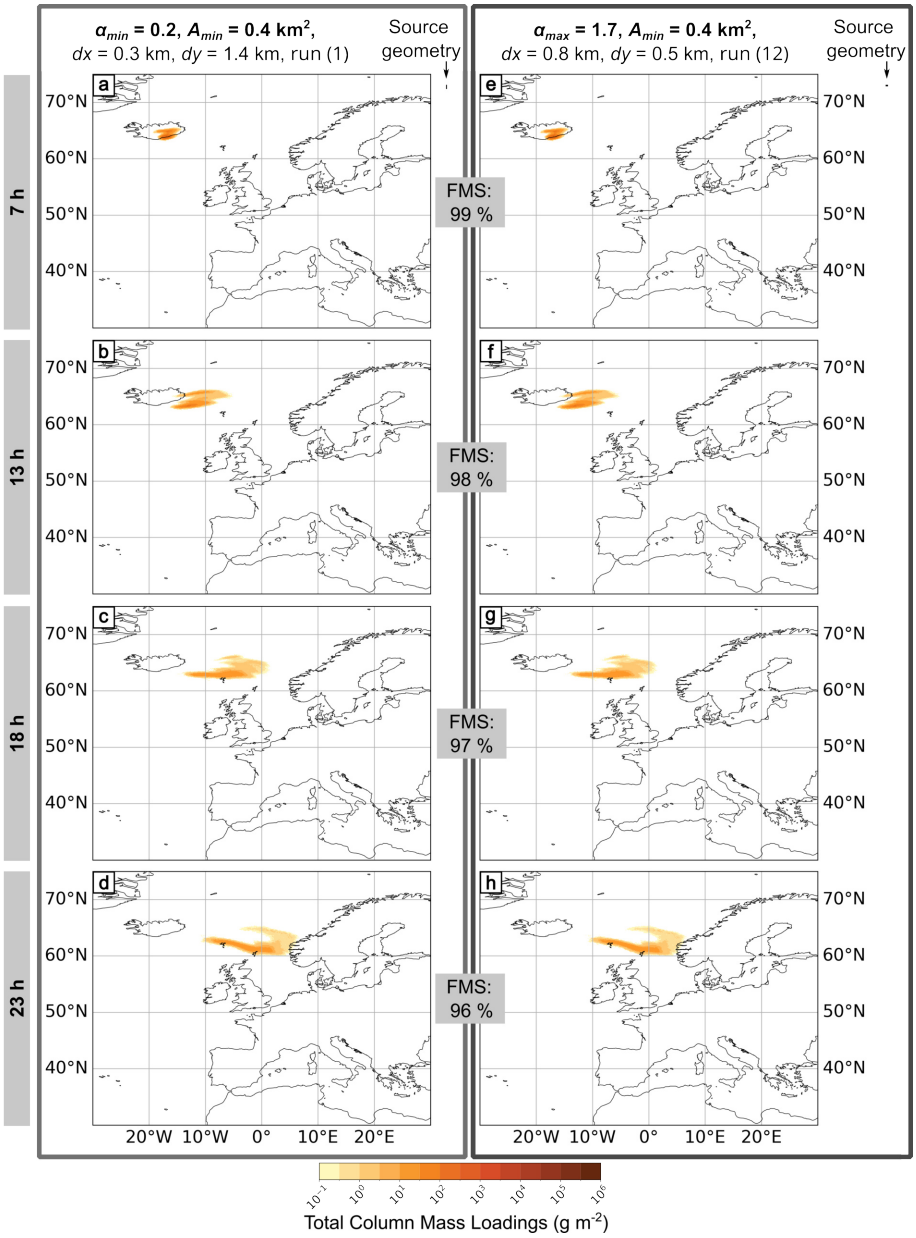


**Fig. S21**: Weather pattern 1. NAME model outputs for numerical experiment 1, all using $A_{min} = 0.4\,\mathrm{km}^2$, a 1 h particle release, $z = 8.5\,\mathrm{km}$, $dz = 3\,\mathrm{km}$ and MER $= 1.06 \times 10^{13}\,\mathrm{g\,h^{-1}}$. The left figure panels **(a-d)** show results from the minimum aspect ratio $\alpha_{min} = 0.2$, and the right panels **(e-h)** show the maximum aspect ratio $\alpha_{max} = 1.7$. The area and orientation of the two source geometries are compared in relation to each other next to the parameter list at the top of the figure. For each aspect ratio, four outputs at different times after eruption start $t_0$ are shown: **(a & e)** 7 h, **(b & f)** 13 h, **(c & g)** 18 h, and **(d & h)** 23 h. Total column mass loadings are averaged over the previous hour, and we applied a threshold of $0.2\,\mathrm{g\,m^{-2}}$.

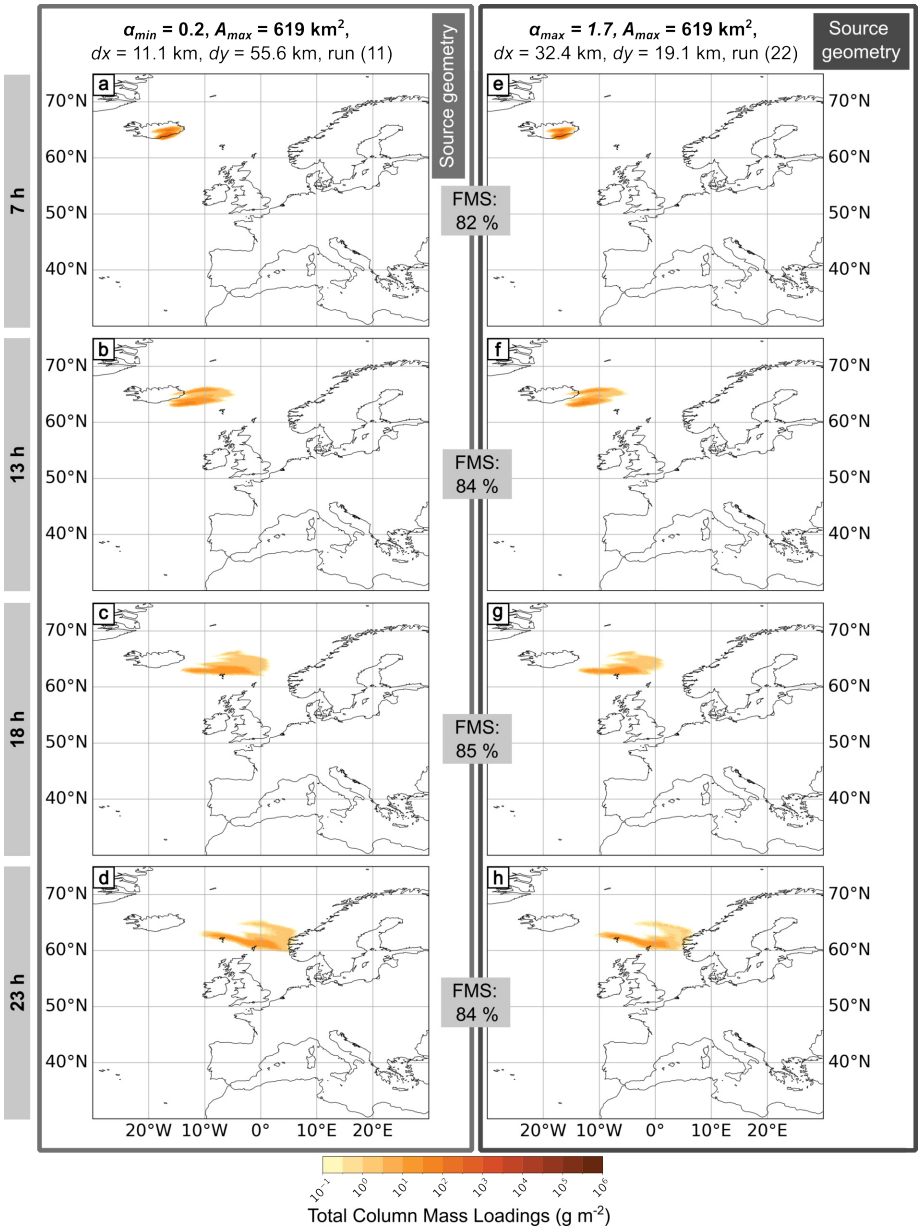


**Fig. S22**: Weather pattern 1. NAME model outputs for numerical experiment 1, all using $A_{max} = 619\,\mathrm{km}^2$, a 1 h particle release, $z = 8.5\,\mathrm{km}$, $dz = 3\,\mathrm{km}$ and $\mathrm{MER} = 1.06 \times 10^{13}\,\mathrm{g\,h^{-1}}$. The left figure panels **(a-d)** show results from the minimum aspect ratio $\alpha_{min} = 0.2$, and the right panels **(e-h)** show the maximum aspect ratio $\alpha_{max} = 1.7$. The area and orientation of the two source geometries are compared in relation to each other next to the parameter list at the top of the figure. For each aspect ratio, four outputs at different times after eruption start $t_0$ are shown: **(a & e)** 7 h, **(b & f)** 13 h, **(c & g)** 18 h, and **(d & h)** 23 h. Total column mass loadings are averaged over the previous hour, and we applied a threshold of $0.2\,\mathrm{g\,m^{-2}}$.

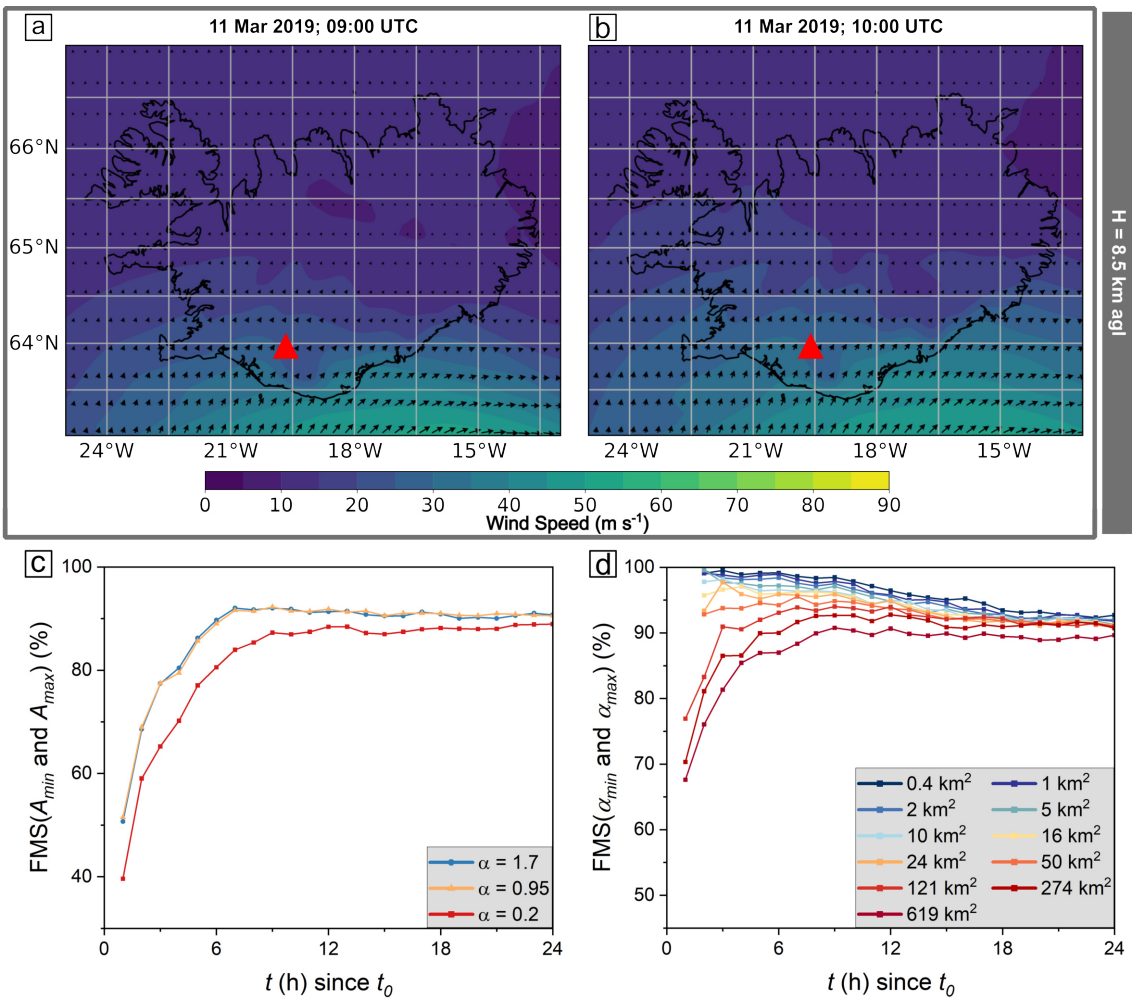


**Fig. S23**: Meteorological data for Iceland for weather pattern 2 at 8.5 km agl elevation at times **(a)** 09:00 UTC and **(b)** 10:00 UTC. The Figure of Merit in space (FMS) determined by Equation 9, shown **(c)** between the plumes generated using the minimum ($A_{min}$) and maximum ($A_{max}$) source area and **(d)** between the minimum ($\alpha_{min}$) and maximum ($\alpha_{max}$) aspect ratio.

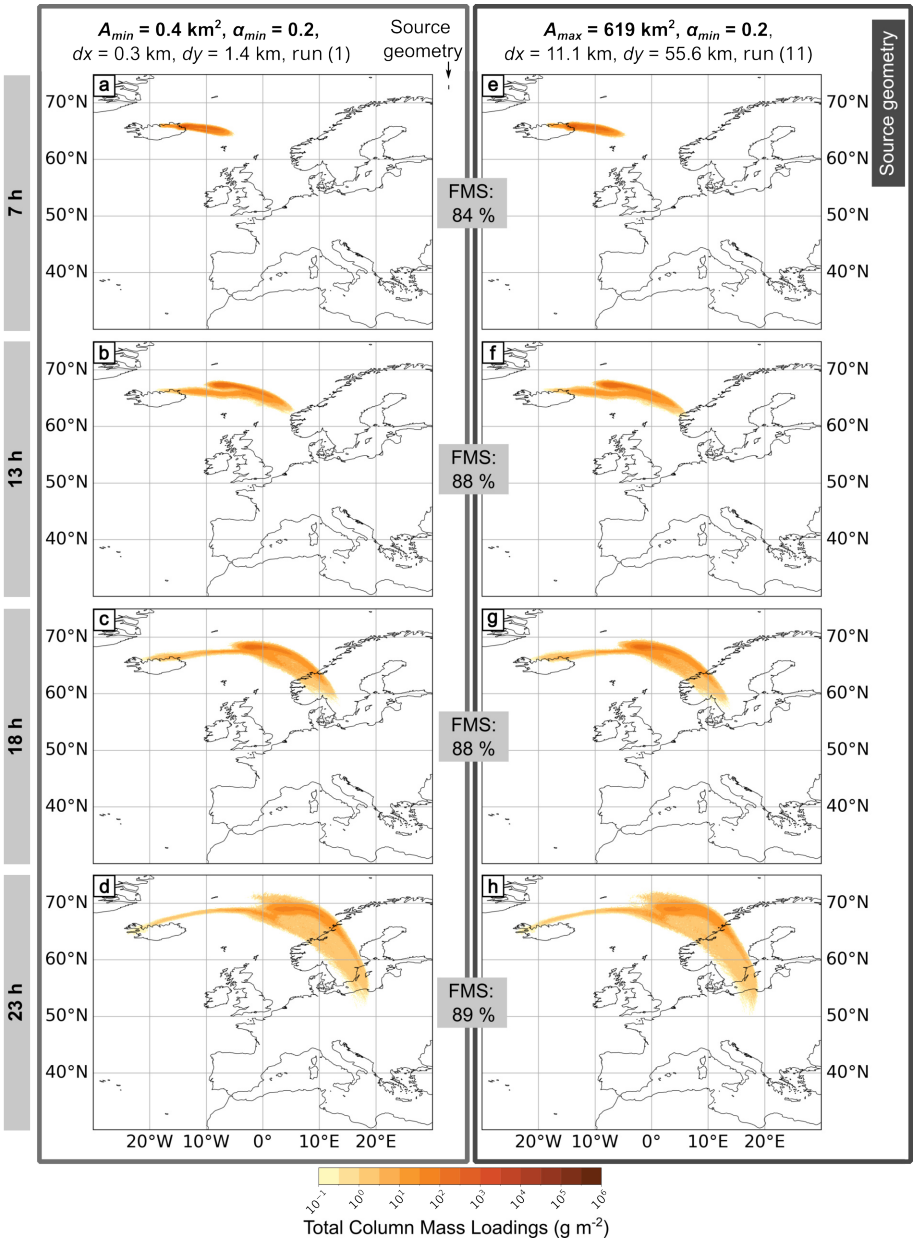


**Fig. S24**: Weather pattern 2. NAME outputs for numerical experiment 1, all using $\alpha_{min} = 0.2$, a 1 h particle release, $z = 8.5$ km, $dz = 3$ km and MER $= 1.06 \times 10^{13}$ g h$^{-1}$. The panels on the left are for the minimum source area, and the panels on the right are for the maximum. The area and orientation of the two source geometries are compared in relation to each other next to the parameter list at the top of the figure. For each area, four outputs are presented at different times after the eruption start $t_0$: **(a & e)** 7 h, **(b & f)** 13 h, **(c & g)** 18 h, and **(d & h)** 23 h. Total column mass loadings are averaged over the previous hour, and we applied a threshold of 0.2 g m$^{-2}$.

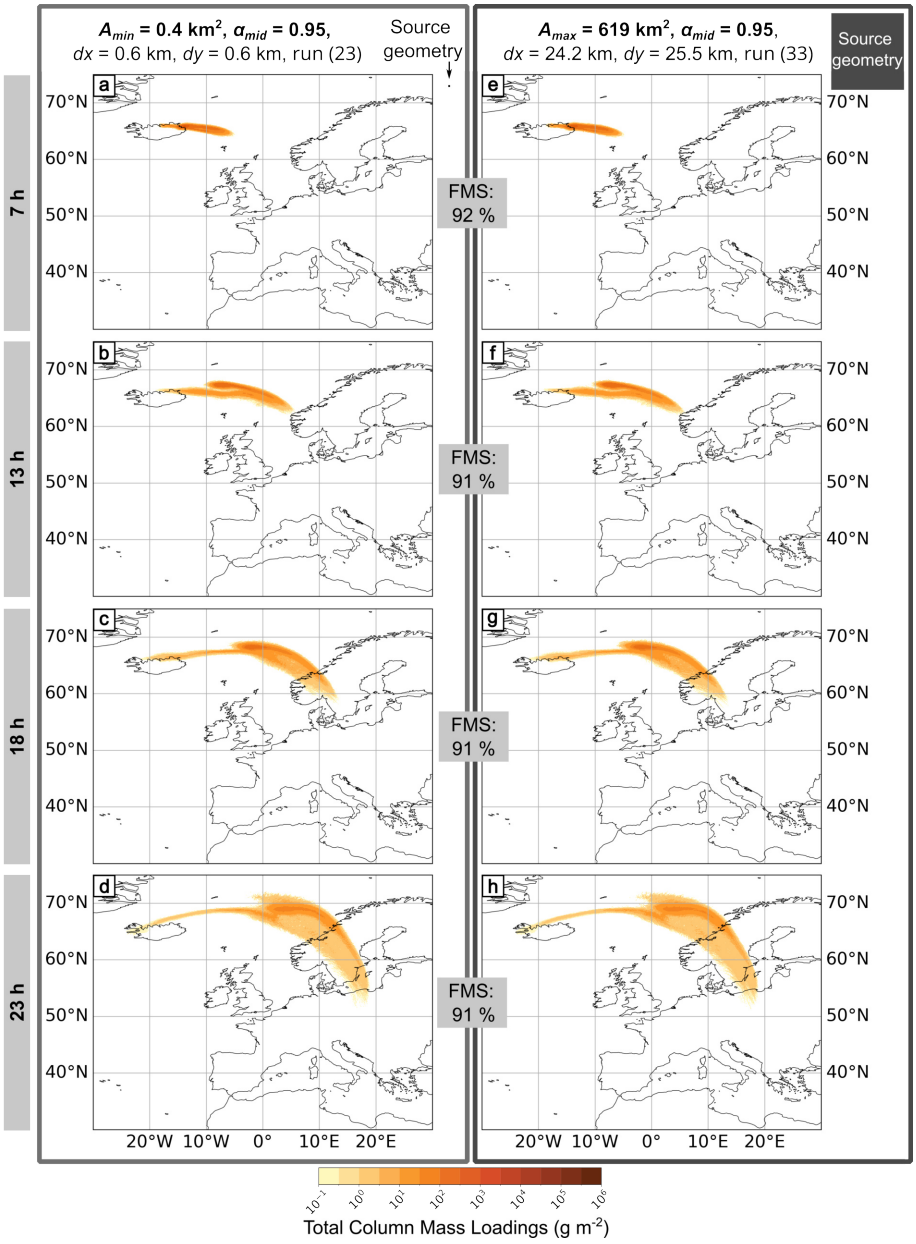


**Fig. S25**: Weather pattern 2. NAME outputs for numerical experiment 1, all using $\alpha_{mid} = 0.95$, a 1 h particle release, $z = 8.5$ km, $dz = 3$ km and MER $= 1.06 \times 10^{13}$ g h$^{-1}$. The panels on the left are for the minimum source area, and the panels on the right are for the maximum. The area and orientation of the two source geometries are compared in relation to each other next to the parameter list at the top of the figure. For each area, four outputs are presented at different times after the eruption start $t_0$: **(a & e)** 7 h, **(b & f)** 13 h, **(c & g)** 18 h, and **(d & h)** 23 h. Total column mass loadings are averaged over the previous hour, and we applied a threshold of 0.2 g m$^{-2}$.

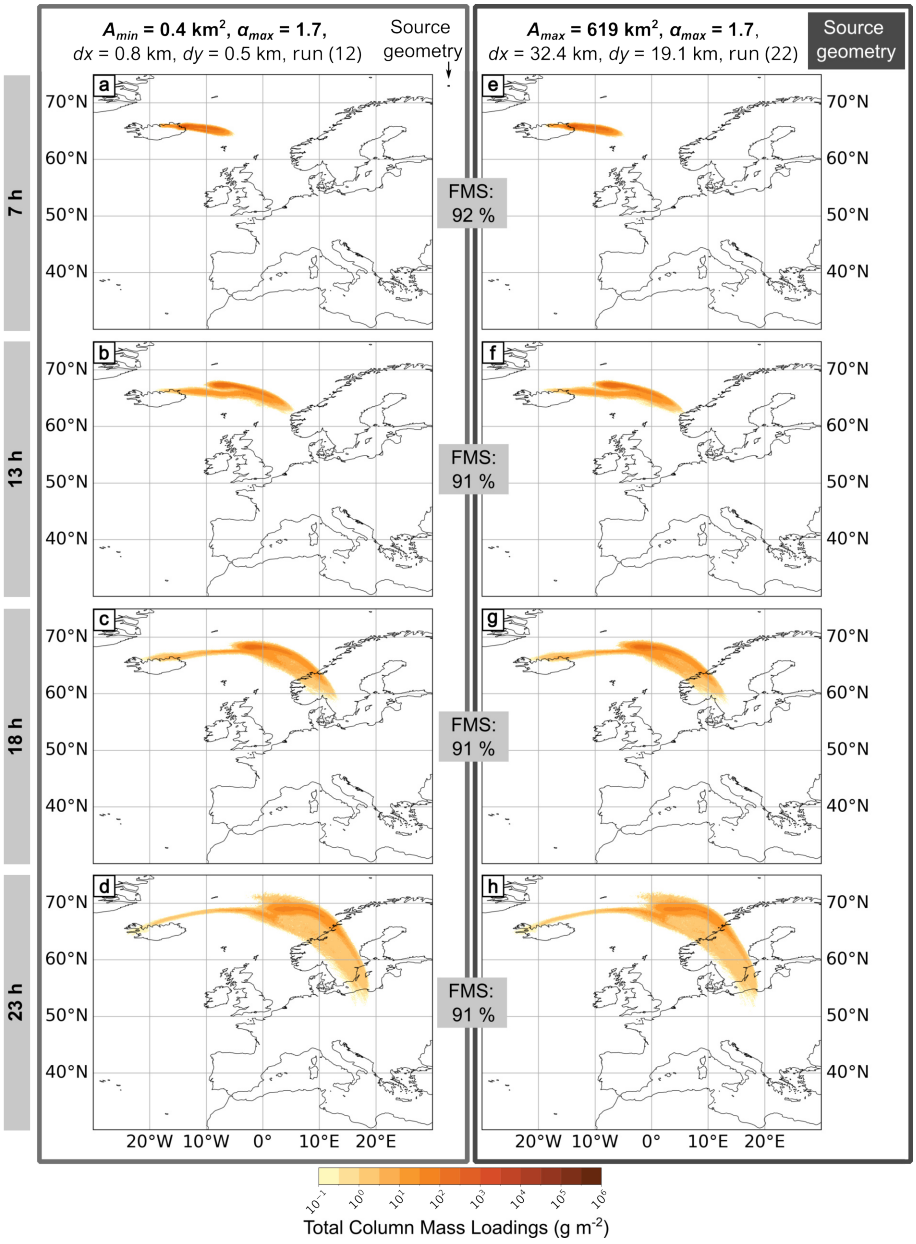


**Fig. S26**: Weather pattern 2. NAME outputs for numerical experiment 1, all using $\alpha_{max} = 1.7$, a 1 h particle release, $z = 8.5$ km, $dz = 3$ km and MER $= 1.06 \times 10^{13}$ g h$^{-1}$. The panels on the left are for the minimum source area, and the panels on the right are for the maximum. The area and orientation of the two source geometries are compared in relation to each other next to the parameter list at the top of the figure. For each area, four outputs are presented at different times after the eruption start $t_0$: **(a & e)** 7 h, **(b & f)** 13 h, **(c & g)** 18 h, and **(d & h)** 23 h. Total column mass loadings are averaged over the previous hour, and we applied a threshold of 0.2 g m$^{-2}$.

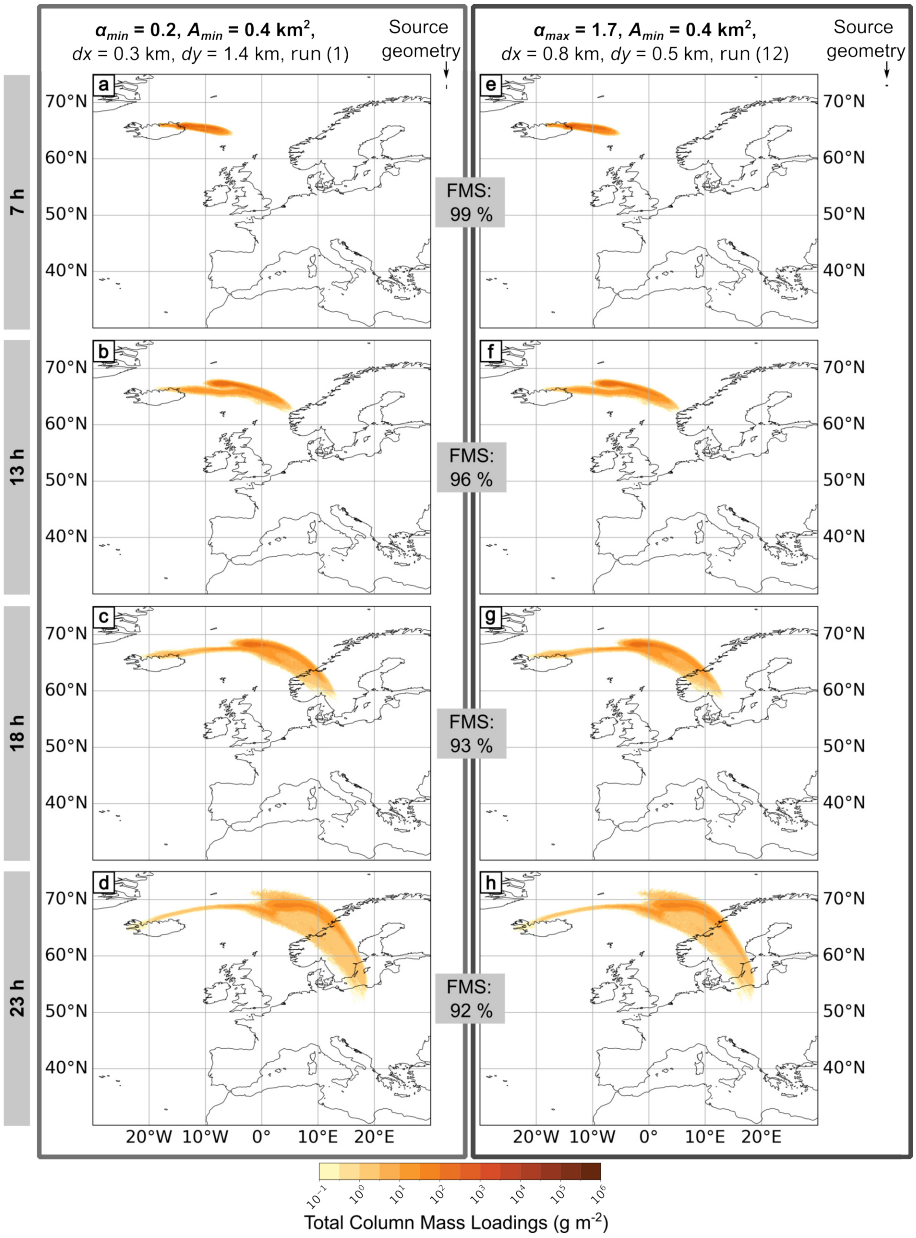


**Fig. S27**: Weather pattern 2. NAME model outputs for numerical experiment 1, all using $A_{min} = 0.4\,\mathrm{km}^2$, a 1 h particle release, $z = 8.5\,\mathrm{km}$, $dz = 3\,\mathrm{km}$ and MER $= 1.06 \times 10^{13}\,\mathrm{g\,h^{-1}}$. The left figure panels **(a-d)** show results from the minimum aspect ratio $\alpha_{min} = 0.2$, and the right panels **(e-h)** show the maximum aspect ratio $\alpha_{max} = 1.7$. The area and orientation of the two source geometries are compared in relation to each other next to the parameter list at the top of the figure. For each aspect ratio, four outputs at different times after eruption start $t_0$ are shown: **(a & e)** 7 h, **(b & f)** 13 h, **(c & g)** 18 h, and **(d & h)** 23 h. Total column mass loadings are averaged over the previous hour, and we applied a threshold of $0.2\,\mathrm{g\,m^{-2}}$.

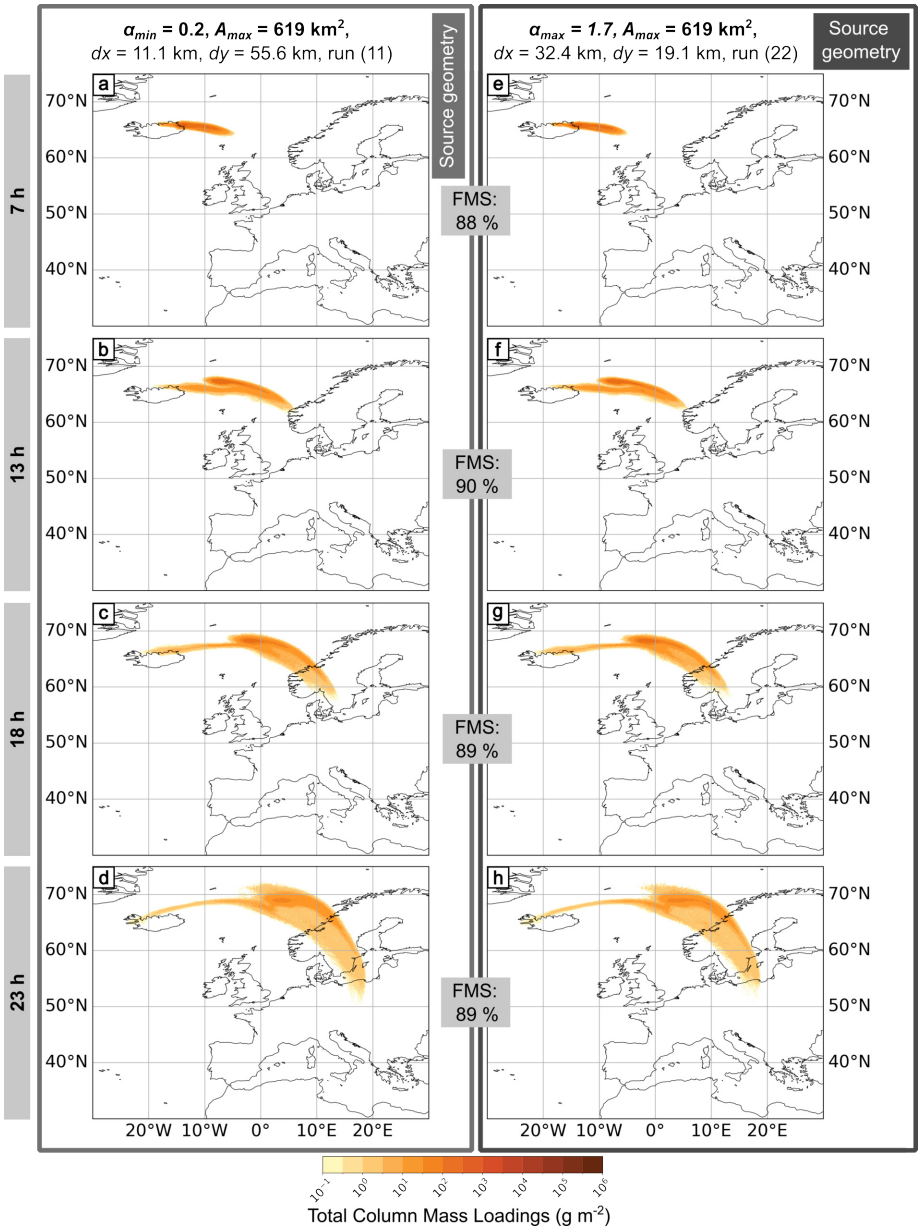


**Fig. S28**: Weather pattern 2. NAME model outputs for numerical experiment 1, all using $A_{max} = 619\,\mathrm{km}^2$, a 1 h particle release, $z = 8.5\,\mathrm{km}$, $dz = 3\,\mathrm{km}$ and MER $= 1.06 \times 10^{13}\,\mathrm{g\,h^{-1}}$. The left figure panels **(a-d)** show results from the minimum aspect ratio $\alpha_{min} = 0.2$, and the right panels **(e-h)** show the maximum aspect ratio $\alpha_{max} = 1.7$. The area and orientation of the two source geometries are compared in relation to each other next to the parameter list at the top of the figure. For each aspect ratio, four outputs at different times after eruption start $t_0$ are shown: **(a & e)** 7 h, **(b & f)** 13 h, **(c & g)** 18 h, and **(d & h)** 23 h. Total column mass loadings are averaged over the previous hour, and we applied a threshold of $0.2\,\mathrm{g\,m^{-2}}$.

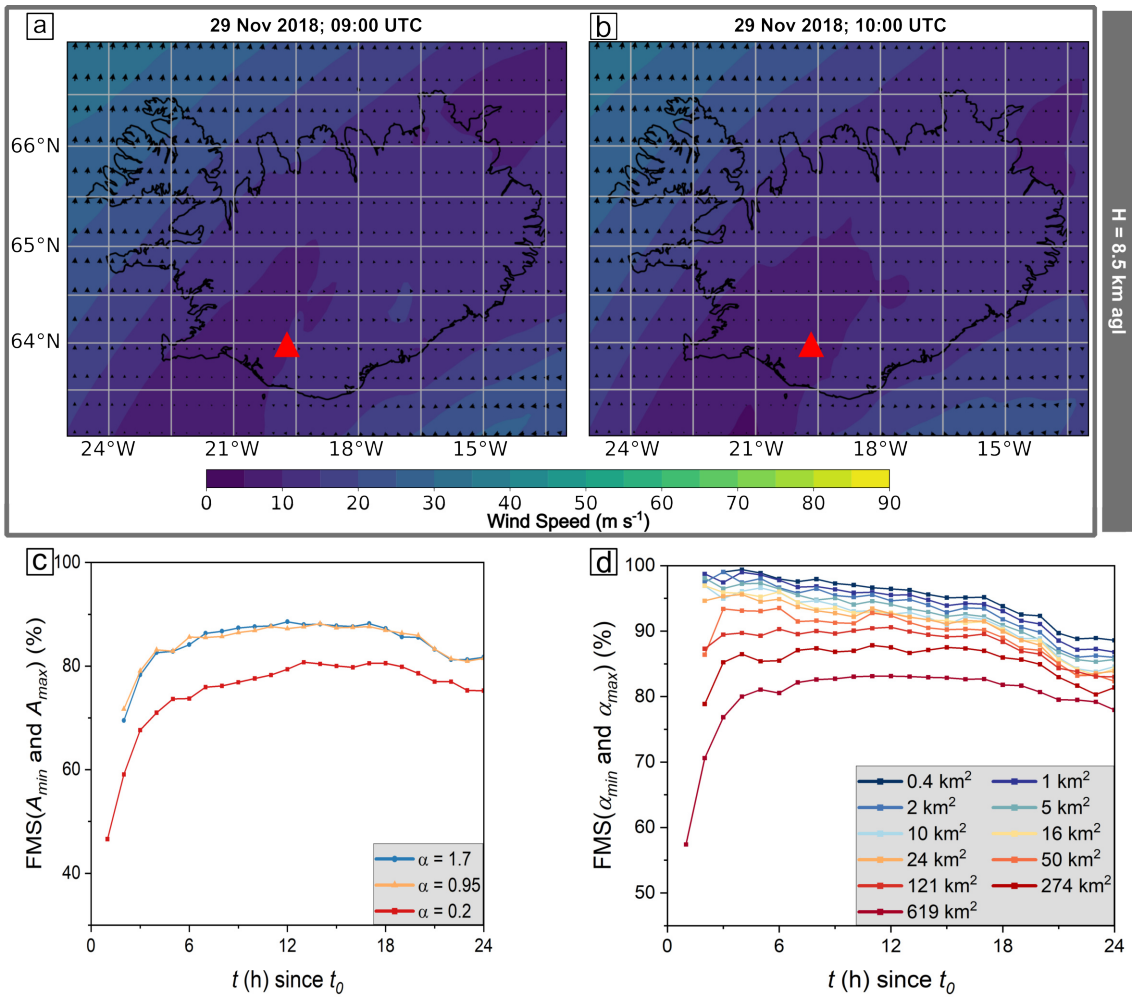


**Fig. S29**: Meteorological data for Iceland for weather pattern 4 at 8.5 km agl elevation at times **(a)** 09:00 UTC and **(b)** 10:00 UTC. The Figure of Merit in space (FMS) determined by Equation 9, shown **(c)** between the plumes generated using the minimum ($A_{min}$) and maximum ($A_{max}$) source area and **(d)** between the minimum ($\alpha_{min}$) and maximum ($\alpha_{max}$) aspect ratio.

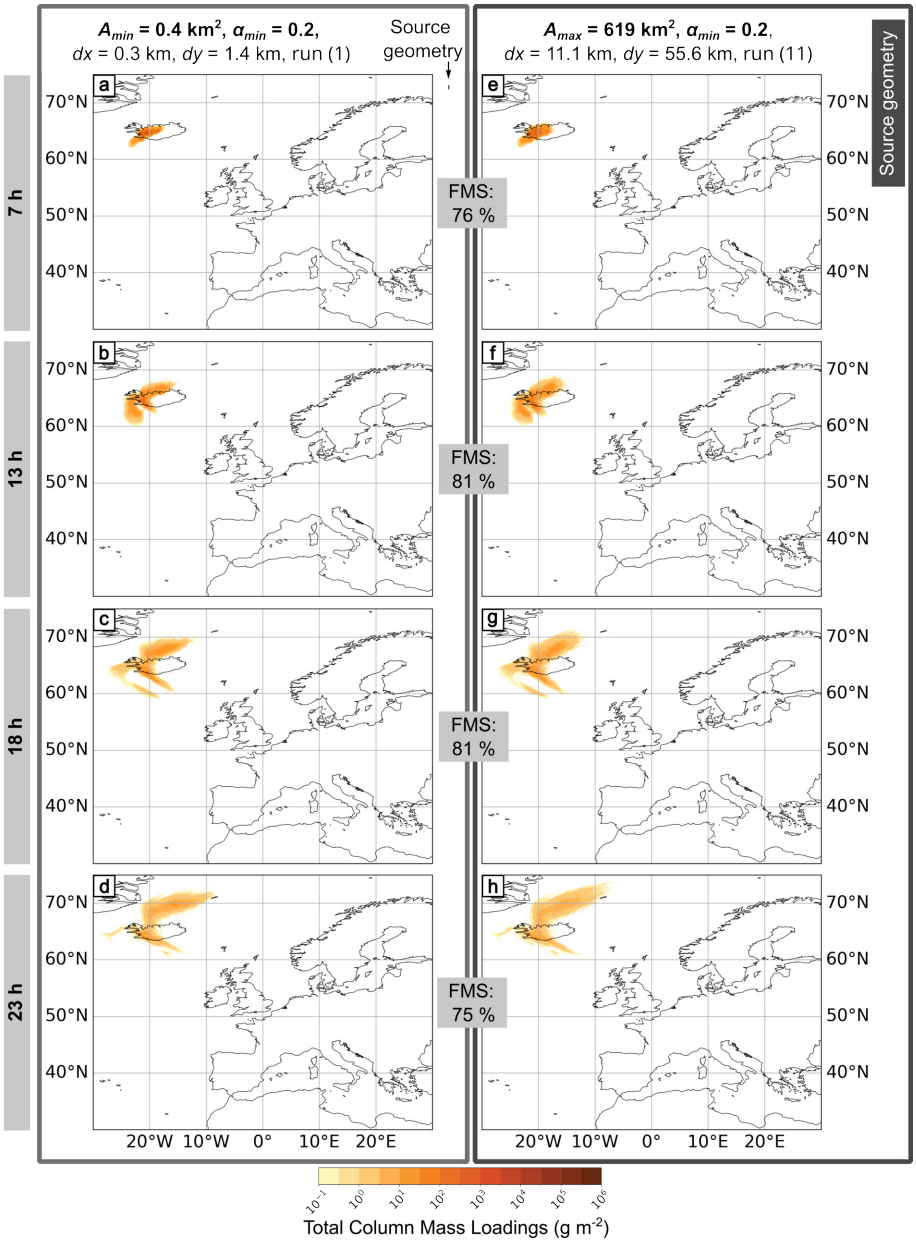


**Fig. S30**: Weather pattern 4. NAME outputs for numerical experiment 1, all using $\alpha_{min} = 0.2$, a 1 h particle release, $z = 8.5$ km, $dz = 3$ km and MER $= 1.06 \times 10^{13}$ g h$^{-1}$. The panels on the left are for the minimum source area, and the panels on the right are for the maximum. The area and orientation of the two source geometries are compared in relation to each other next to the parameter list at the top of the figure. For each area, four outputs are presented at different times after the eruption start $t_0$: **(a & e)** 7 h, **(b & f)** 13 h, **(c & g)** 18 h, and **(d & h)** 23 h. Total column mass loadings are averaged over the previous hour, and we applied a threshold of 0.2 g m$^{-2}$.

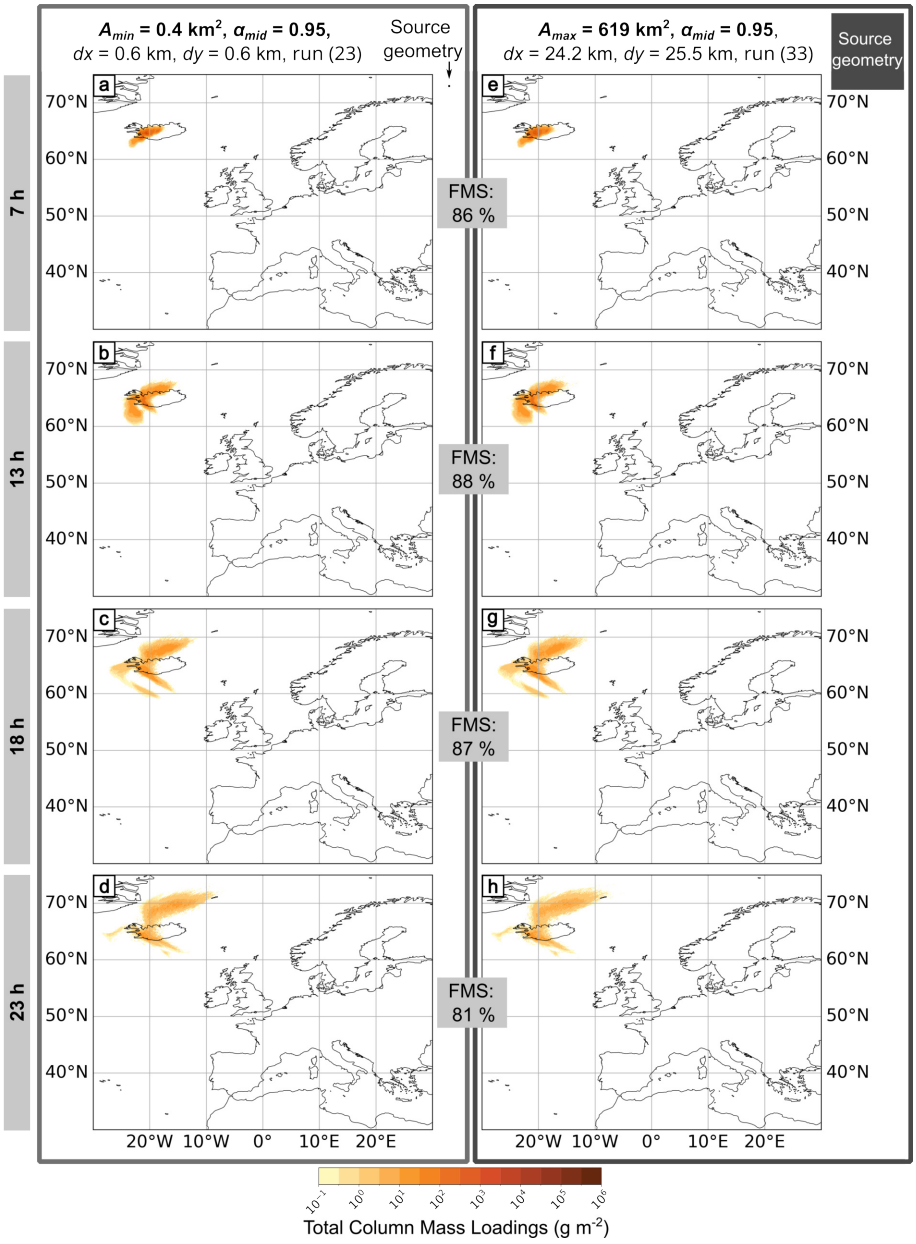


**Fig. S31**: Weather pattern 4. NAME outputs for numerical experiment 1, all using $\alpha_{mid} = 0.95$, a 1 h particle release, $z = 8.5$ km, $dz = 3$ km and MER $= 1.06 \times 10^{13}$ g h$^{-1}$. The panels on the left are for the minimum source area, and the panels on the right are for the maximum. The area and orientation of the two source geometries are compared in relation to each other next to the parameter list at the top of the figure. For each area, four outputs are presented at different times after the eruption start $t_0$: **(a & e)** 7 h, **(b & f)** 13 h, **(c & g)** 18 h, and **(d & h)** 23 h. Total column mass loadings are averaged over the previous hour, and we applied a threshold of 0.2 g m$^{-2}$.

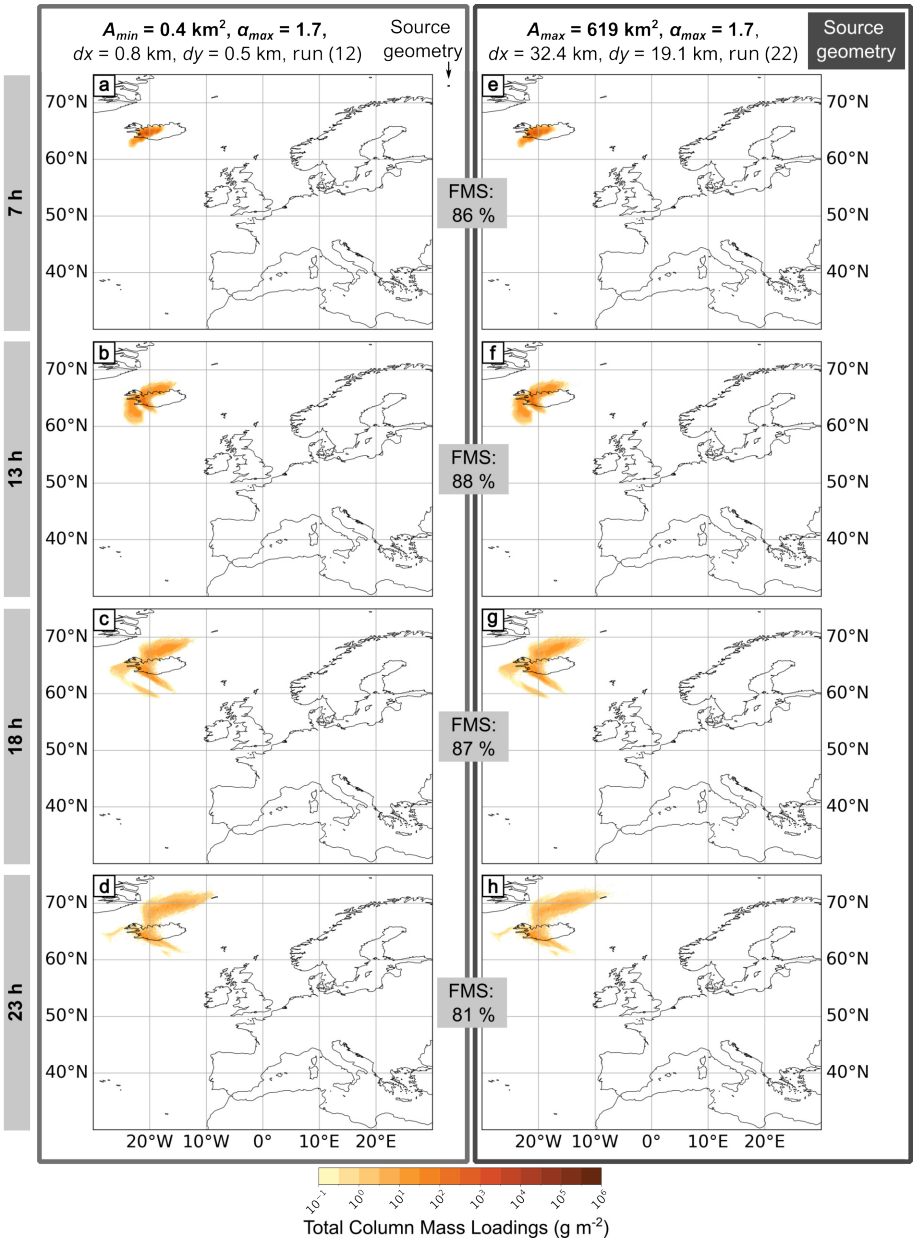


**Fig. S32**: Weather pattern 4. NAME outputs for numerical experiment 1, all using $\alpha_{max} = 1.7$, a 1 h particle release, $z = 8.5$ km, $dz = 3$ km and MER $= 1.06 \times 10^{13}$ g h$^{-1}$. The panels on the left are for the minimum source area, and the panels on the right are for the maximum. The area and orientation of the two source geometries are compared in relation to each other next to the parameter list at the top of the figure. For each area, four outputs are presented at different times after the eruption start $t_0$: **(a & e)** 7 h, **(b & f)** 13 h, **(c & g)** 18 h, and **(d & h)** 23 h. Total column mass loadings are averaged over the previous hour, and we applied a threshold of 0.2 g m$^{-2}$.

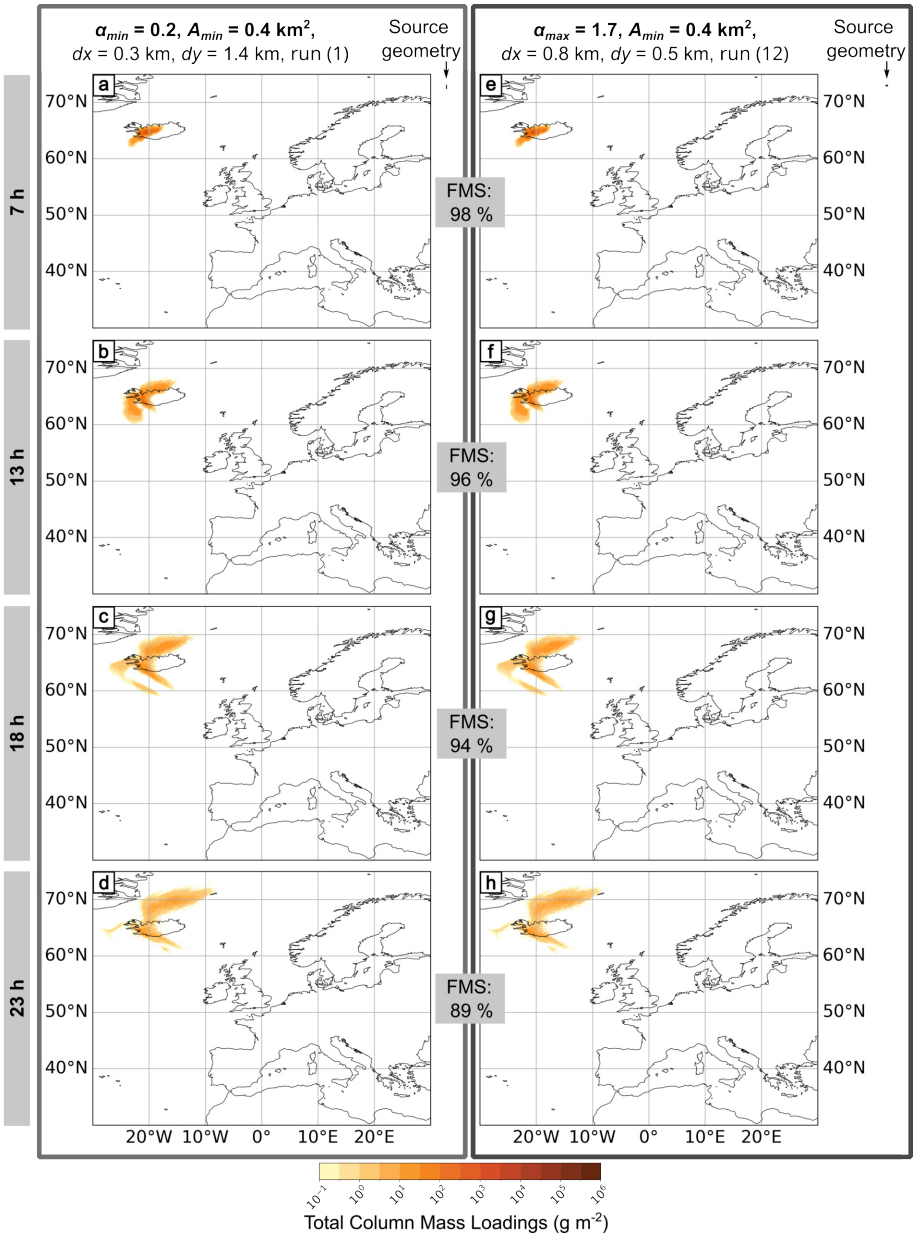


**Fig. S33**: Weather pattern 4. NAME model outputs for numerical experiment 1, all using $A_{min} = 0.4\,\mathrm{km}^2$, a 1 h particle release, $z = 8.5\,\mathrm{km}$, $dz = 3\,\mathrm{km}$ and MER $= 1.06 \times 10^{13}\,\mathrm{g\,h^{-1}}$. The left figure panels **(a-d)** show results from the minimum aspect ratio $\alpha_{min} = 0.2$, and the right panels **(e-h)** show the maximum aspect ratio $\alpha_{max} = 1.7$. The area and orientation of the two source geometries are compared in relation to each other next to the parameter list at the top of the figure. For each aspect ratio, four outputs at different times after eruption start $t_0$ are shown: **(a & e)** 7 h, **(b & f)** 13 h, **(c & g)** 18 h, and **(d & h)** 23 h. Total column mass loadings are averaged over the previous hour, and we applied a threshold of $0.2\,\mathrm{g\,m^{-2}}$.

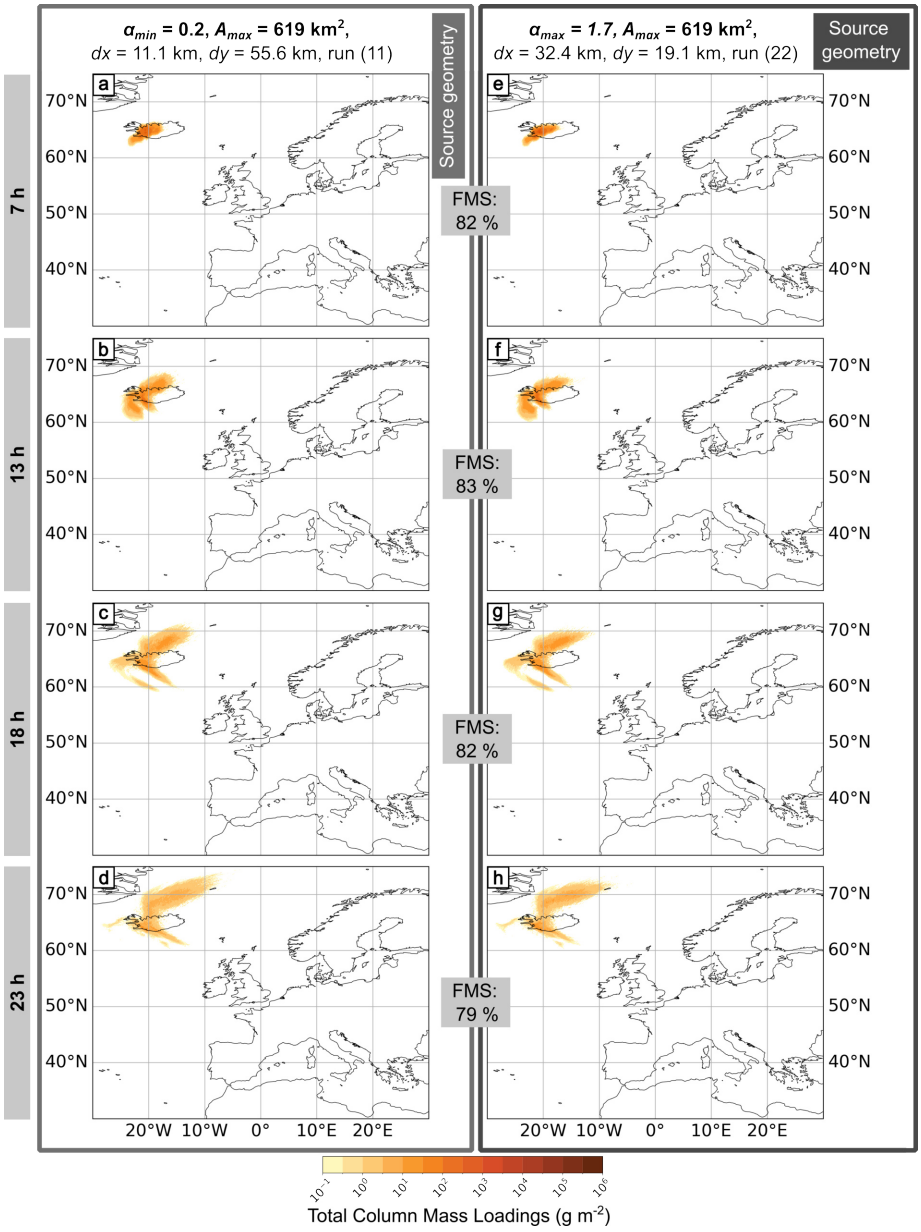


**Fig. S34**: Weather pattern 4. NAME model outputs for numerical experiment 1, all using $A_{max} = 619\,\mathrm{km}^2$, a 1 h particle release, $z = 8.5\,\mathrm{km}$, $dz = 3\,\mathrm{km}$ and $\mathrm{MER} = 1.06 \times 10^{13}\,\mathrm{g\,h^{-1}}$. The left figure panels **(a-d)** show results from the minimum aspect ratio $\alpha_{min} = 0.2$, and the right panels **(e-h)** show the maximum aspect ratio $\alpha_{max} = 1.7$. The area and orientation of the two source geometries are compared in relation to each other next to the parameter list at the top of the figure. For each aspect ratio, four outputs at different times after eruption start $t_0$ are shown: **(a & e)** 7 h, **(b & f)** 13 h, **(c & g)** 18 h, and **(d & h)** 23 h. Total column mass loadings are averaged over the previous hour, and we applied a threshold of $0.2\,\mathrm{g\,m^{-2}}$.

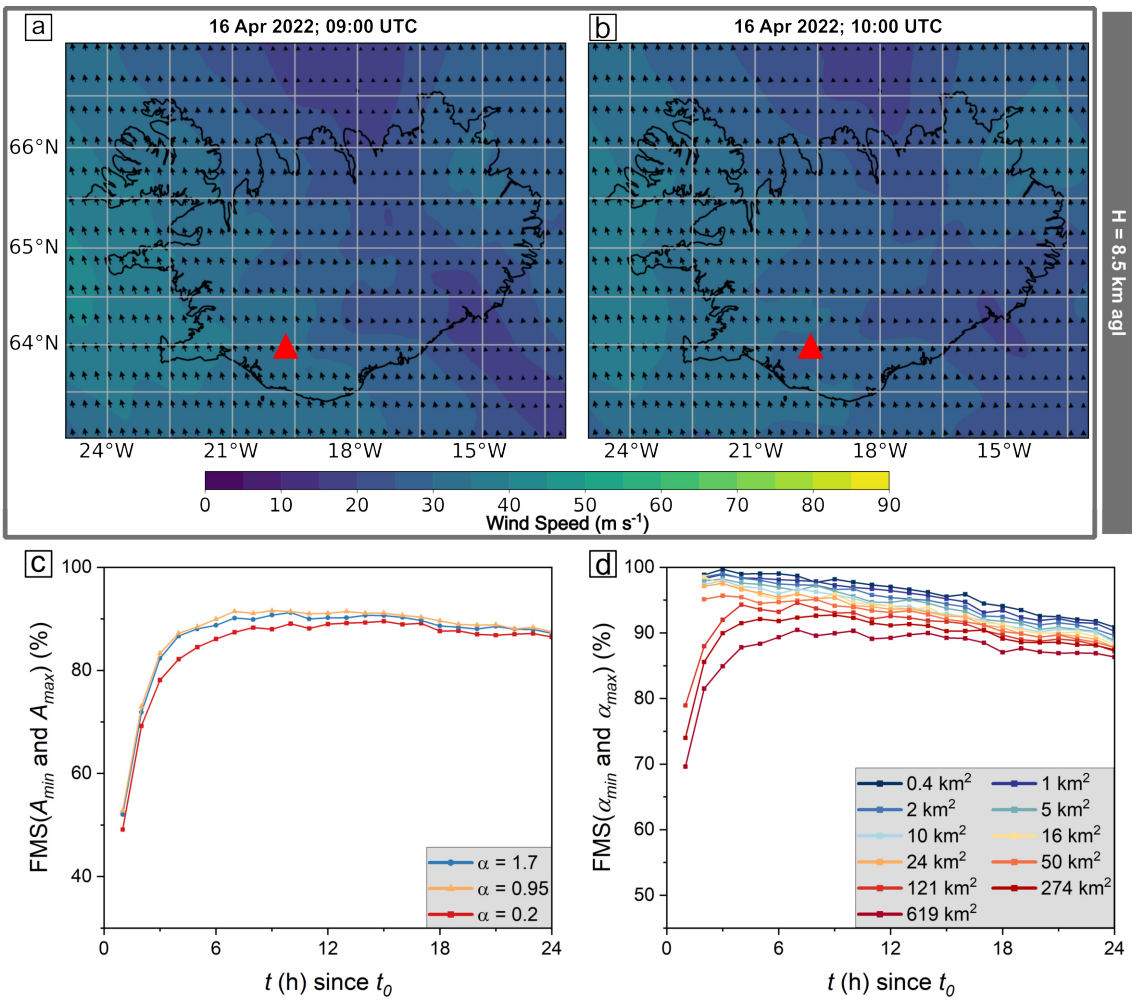


**Fig. S35**: Meteorological data for Iceland for weather pattern 5 at 8.5 km agl elevation at times **(a)** 09:00 UTC and **(b)** 10:00 UTC. The Figure of Merit in space (FMS) determined by Equation 9, shown **(c)** between the plumes generated using the minimum ($A_{min}$) and maximum ($A_{max}$) source area and **(d)** between the minimum ($\alpha_{min}$) and maximum ($\alpha_{max}$) aspect ratio.

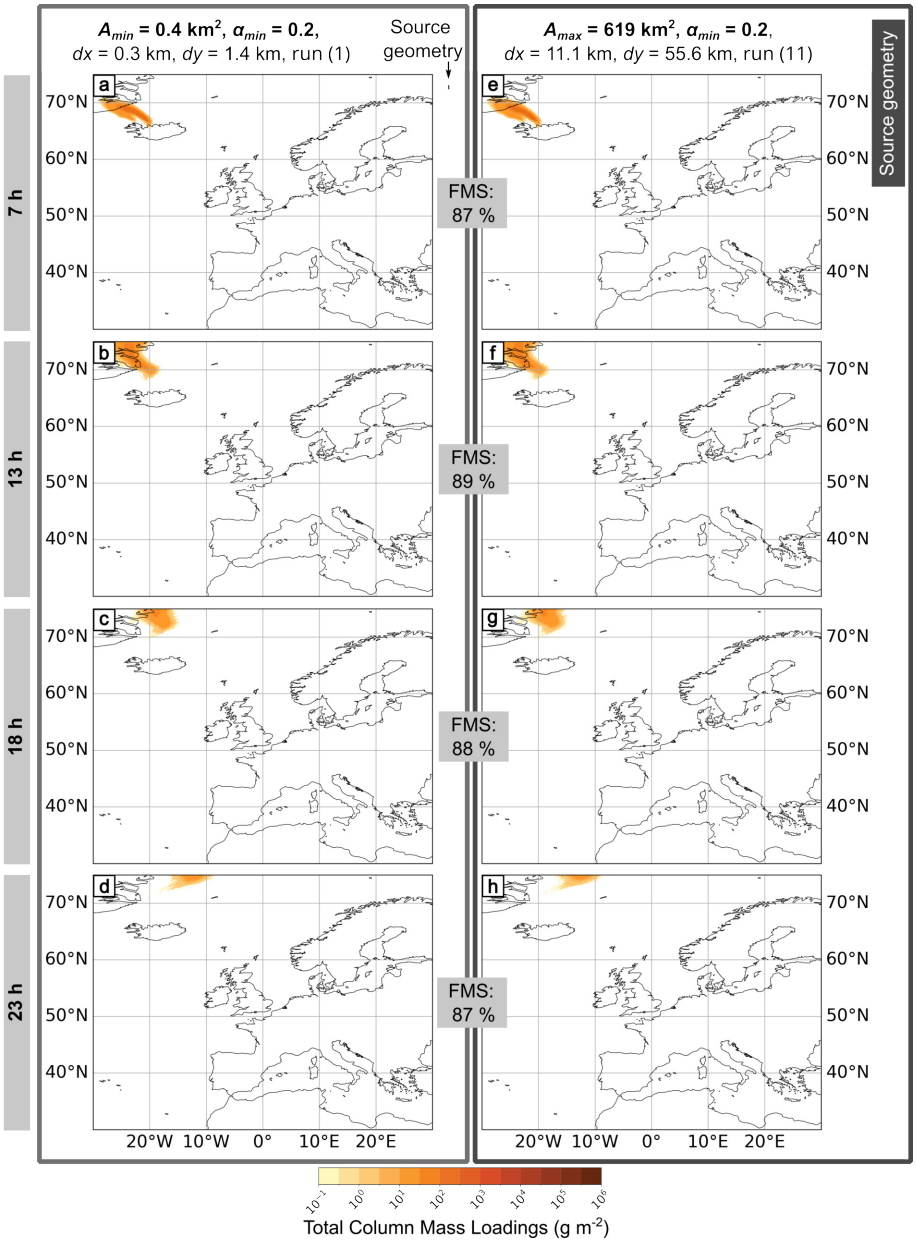


**Fig. S36**: Weather pattern 5. NAME outputs for numerical experiment 1, all using $\alpha_{min} = 0.2$, a 1 h particle release, $z = 8.5$ km, $dz = 3$ km and MER $= 1.06 \times 10^{13}$ g h$^{-1}$. The panels on the left are for the minimum source area, and the panels on the right are for the maximum. The area and orientation of the two source geometries are compared in relation to each other next to the parameter list at the top of the figure. For each area, four outputs are presented at different times after the eruption start $t_0$: **(a & e)** 7 h, **(b & f)** 13 h, **(c & g)** 18 h, and **(d & h)** 23 h. Total column mass loadings are averaged over the previous hour, and we applied a threshold of 0.2 g m$^{-2}$.

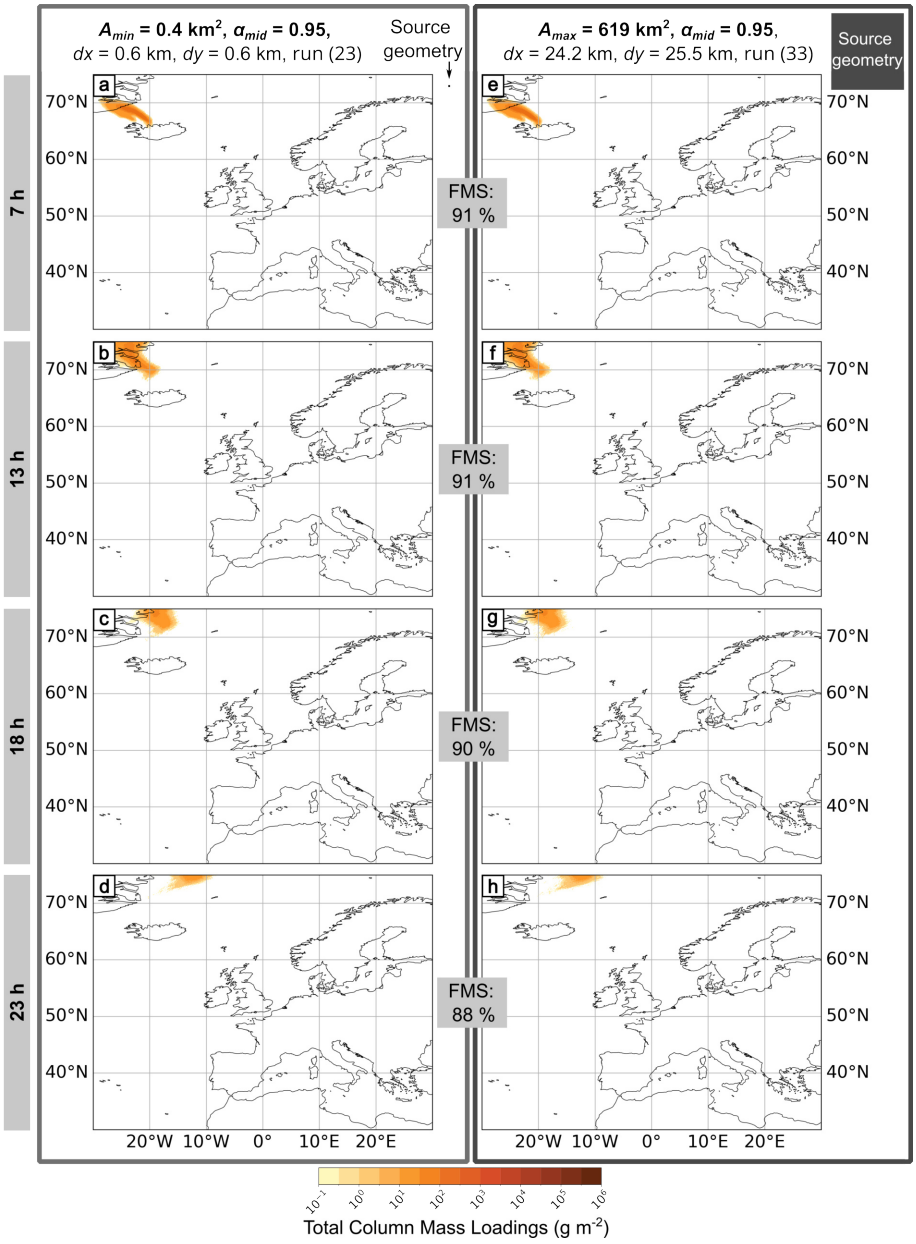


**Fig. S37**: Weather pattern 5. NAME outputs for numerical experiment 1, all using $\alpha_{mid} = 0.95$, a 1 h particle release, $z = 8.5$ km, $dz = 3$ km and MER $= 1.06 \times 10^{13}$ g h$^{-1}$. The panels on the left are for the minimum source area, and the panels on the right are for the maximum. The area and orientation of the two source geometries are compared in relation to each other next to the parameter list at the top of the figure. For each area, four outputs are presented at different times after the eruption start $t_0$: **(a & e)** 7 h, **(b & f)** 13 h, **(c & g)** 18 h, and **(d & h)** 23 h. Total column mass loadings are averaged over the previous hour, and we applied a threshold of 0.2 g m$^{-2}$.

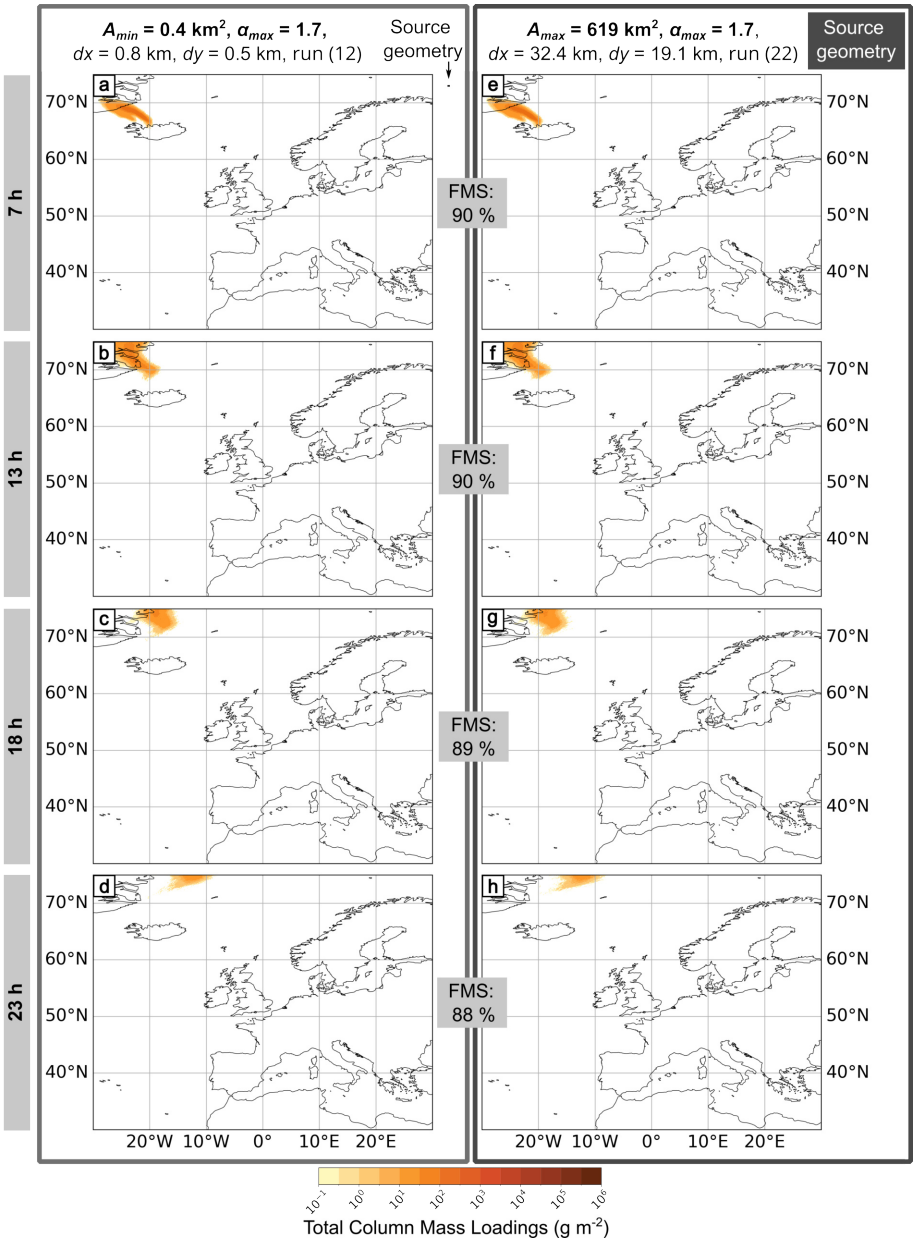


**Fig. S38**: Weather pattern 5. NAME outputs for numerical experiment 1, all using $\alpha_{max} = 1.7$, a 1 h particle release, $z = 8.5$ km, $dz = 3$ km and MER $= 1.06 \times 10^{13}$ g h$^{-1}$. The panels on the left are for the minimum source area, and the panels on the right are for the maximum. The area and orientation of the two source geometries are compared in relation to each other next to the parameter list at the top of the figure. For each area, four outputs are presented at different times after the eruption start $t_0$: **(a & e)** 7 h, **(b & f)** 13 h, **(c & g)** 18 h, and **(d & h)** 23 h. Total column mass loadings are averaged over the previous hour, and we applied a threshold of 0.2 g m$^{-2}$.

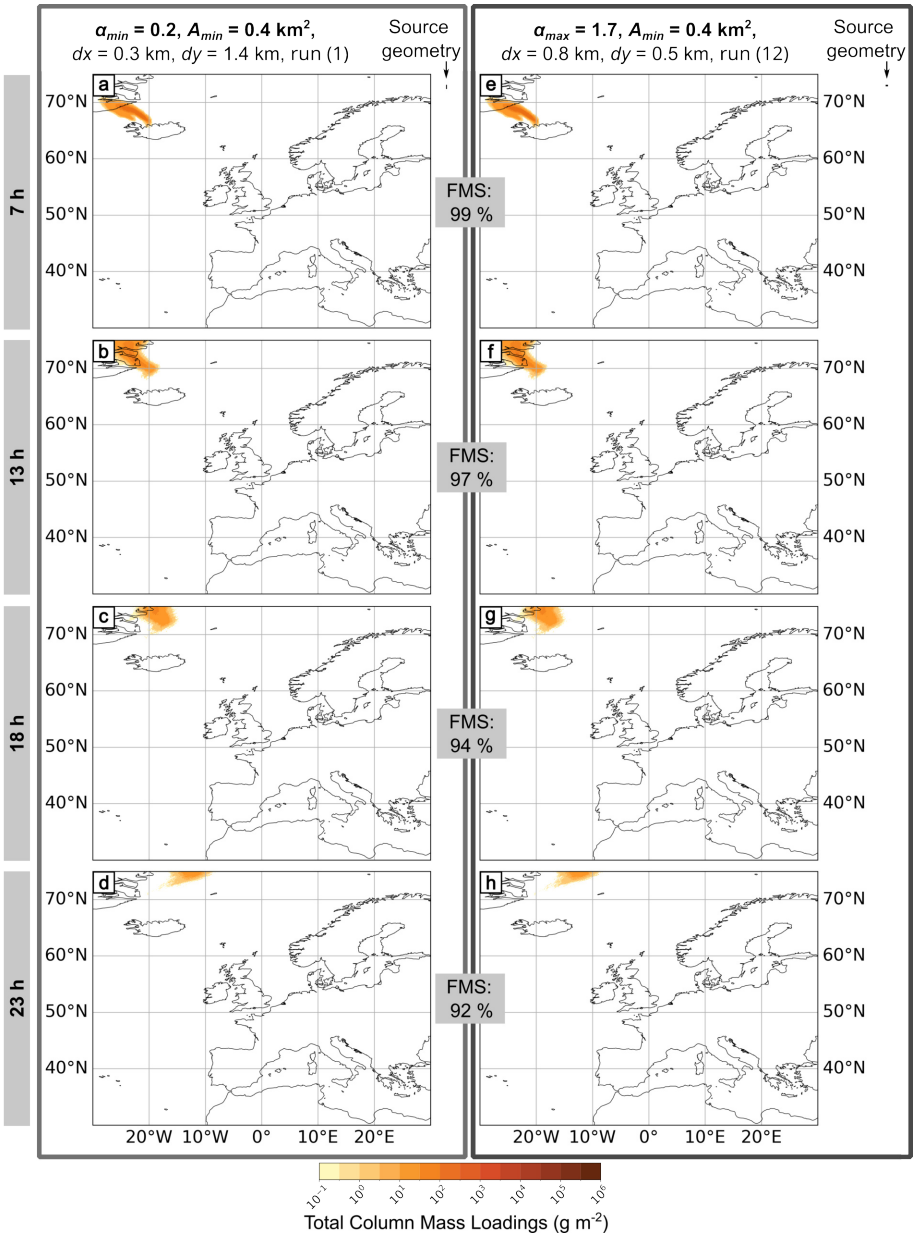


**Fig. S39**: Weather pattern 5. NAME model outputs for numerical experiment 1, all using $A_{min} = 0.4\,\mathrm{km}^2$, a 1 h particle release, $z = 8.5\,\mathrm{km}$, $dz = 3\,\mathrm{km}$ and MER $= 1.06 \times 10^{13}\,\mathrm{g\,h^{-1}}$. The left figure panels **(a-d)** show results from the minimum aspect ratio $\alpha_{min} = 0.2$, and the right panels **(e-h)** show the maximum aspect ratio $\alpha_{max} = 1.7$. The area and orientation of the two source geometries are compared in relation to each other next to the parameter list at the top of the figure. For each aspect ratio, four outputs at different times after eruption start $t_0$ are shown: **(a & e)** 7 h, **(b & f)** 13 h, **(c & g)** 18 h, and **(d & h)** 23 h. Total column mass loadings are averaged over the previous hour, and we applied a threshold of $0.2\,\mathrm{g\,m^{-2}}$.

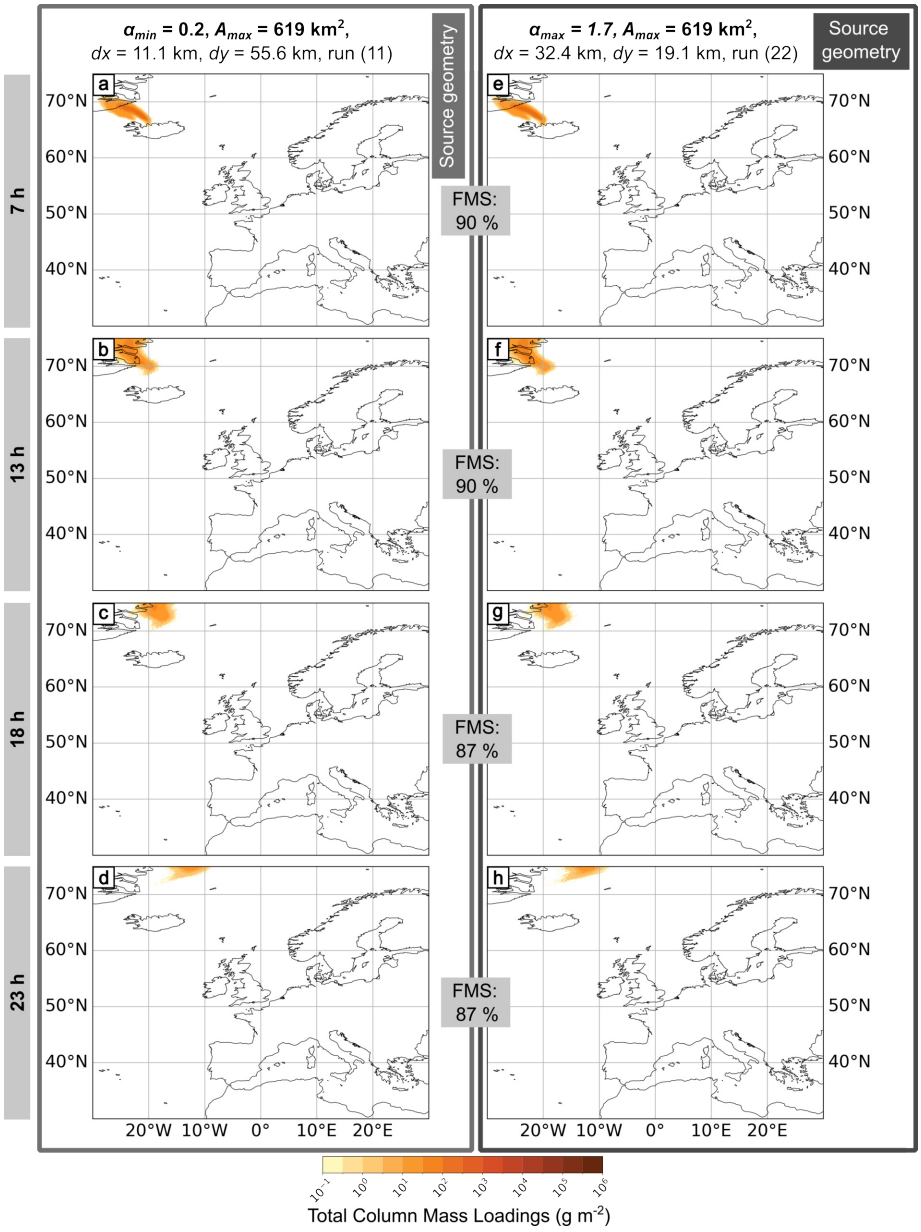


**Fig. S40**: Weather pattern 5. NAME model outputs for numerical experiment 1, all using $A_{max} = 619\,\mathrm{km}^2$, a 1 h particle release, $z = 8.5\,\mathrm{km}$, $dz = 3\,\mathrm{km}$ and MER $= 1.06 \times 10^{13}\,\mathrm{g\,h^{-1}}$. The left figure panels **(a-d)** show results from the minimum aspect ratio $\alpha_{min} = 0.2$, and the right panels **(e-h)** show the maximum aspect ratio $\alpha_{max} = 1.7$. The area and orientation of the two source geometries are compared in relation to each other next to the parameter list at the top of the figure. For each aspect ratio, four outputs at different times after eruption start $t_0$ are shown: **(a & e)** 7 h, **(b & f)** 13 h, **(c & g)** 18 h, and **(d & h)** 23 h. Total column mass loadings are averaged over the previous hour, and we applied a threshold of $0.2\,\mathrm{g\,m^{-2}}$.

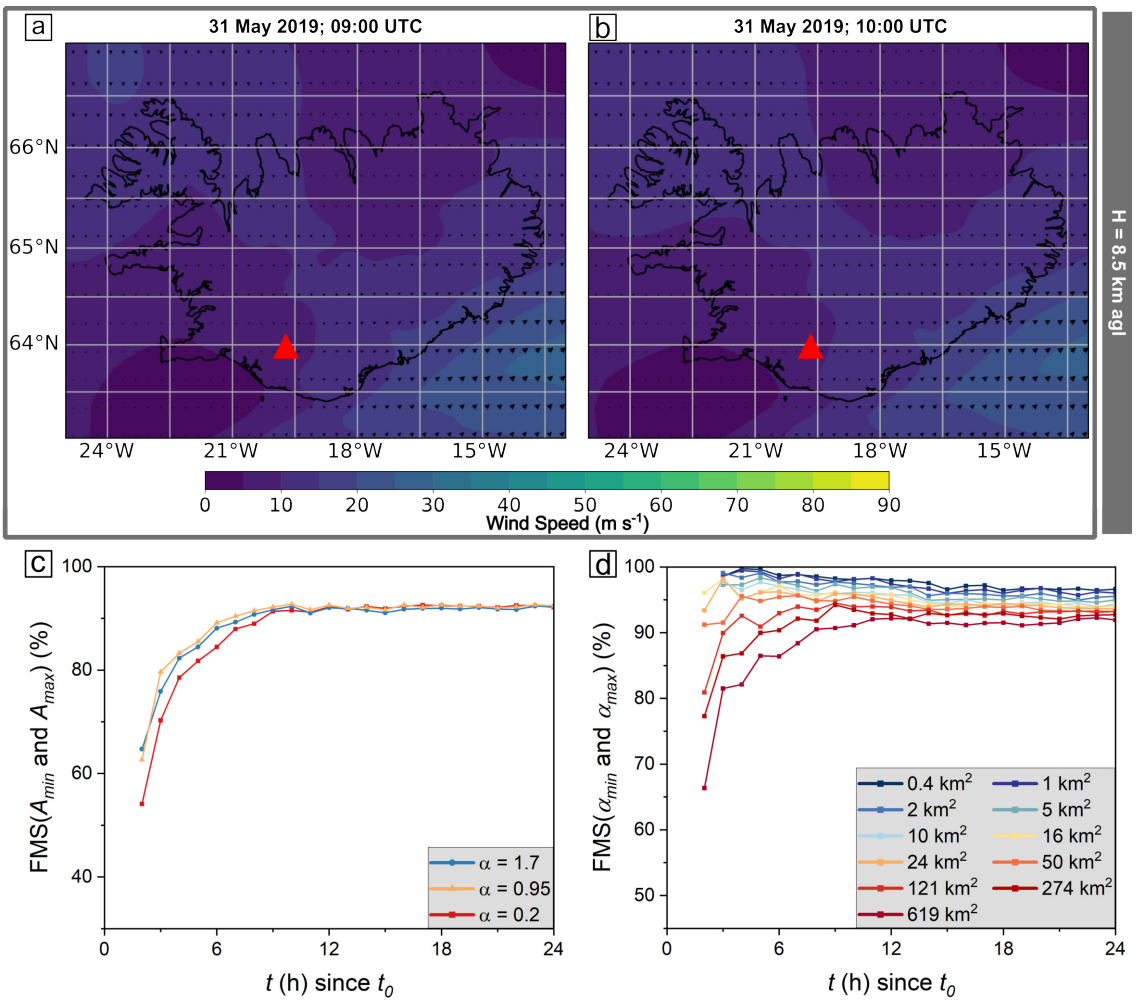


**Fig. S41**: Meteorological data for Iceland for weather pattern 6 at 8.5 km agl elevation at times **(a)** 09:00 UTC and **(b)** 10:00 UTC. The Figure of Merit in space (FMS) determined by Equation 9, shown **(c)** between the plumes generated using the minimum ($A_{min}$) and maximum ($A_{max}$) source area and **(d)** between the minimum ($\alpha_{min}$) and maximum ($\alpha_{max}$) aspect ratio.

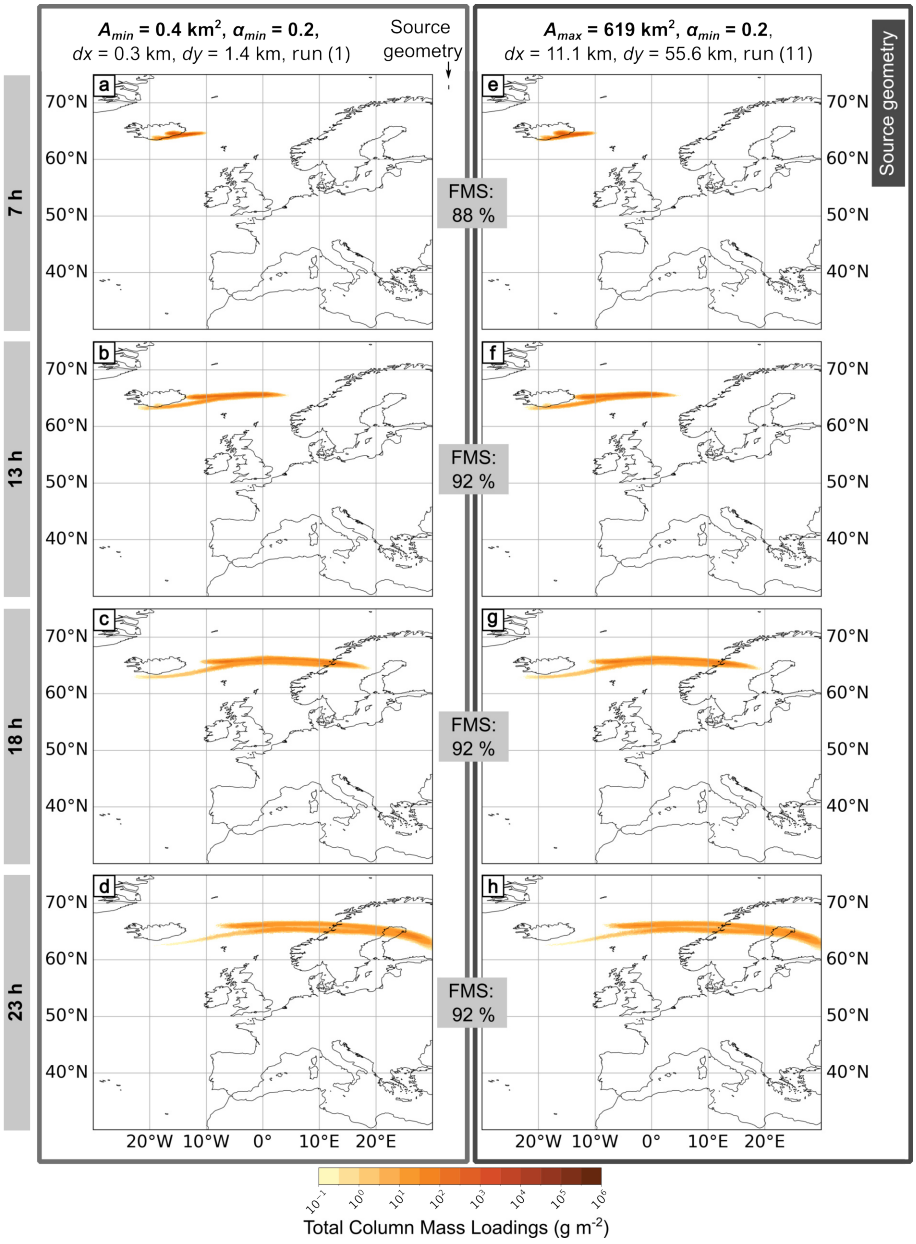


**Fig. S42**: Weather pattern 6. NAME outputs for numerical experiment 1, all using $\alpha_{min} = 0.2$, a 1 h particle release, $z = 8.5$ km, $dz = 3$ km and MER $= 1.06 \times 10^{13}$ g h$^{-1}$. The panels on the left are for the minimum source area, and the panels on the right are for the maximum. The area and orientation of the two source geometries are compared in relation to each other next to the parameter list at the top of the figure. For each area, four outputs are presented at different times after the eruption start $t_0$: **(a & e)** 7 h, **(b & f)** 13 h, **(c & g)** 18 h, and **(d & h)** 23 h. Total column mass loadings are averaged over the previous hour, and we applied a threshold of 0.2 g m$^{-2}$.

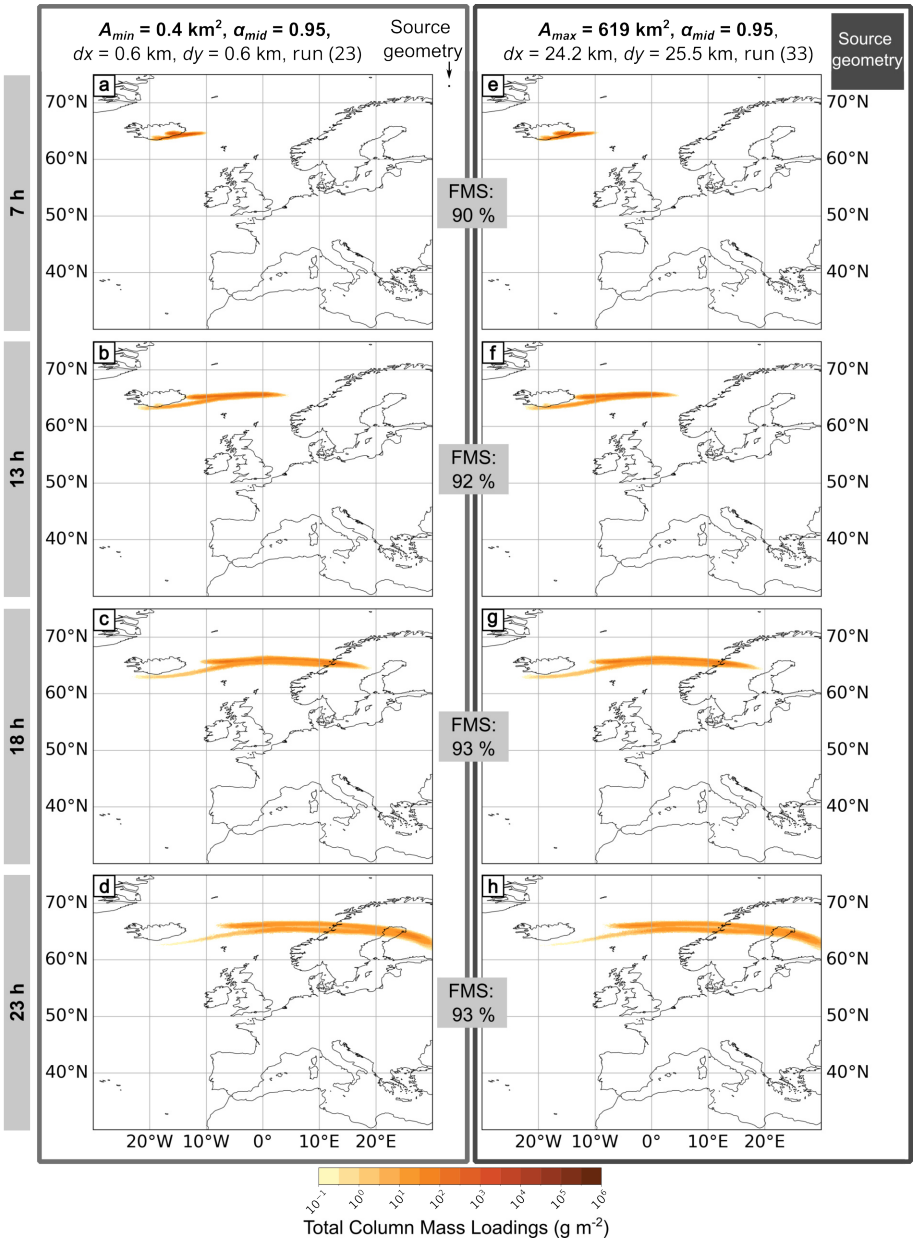


**Fig. S43**: Weather pattern 6. NAME outputs for numerical experiment 1, all using $\alpha_{mid} = 0.95$, a 1 h particle release, $z = 8.5$ km, $dz = 3$ km and MER $= 1.06 \times 10^{13}$ g h$^{-1}$. The panels on the left are for the minimum source area, and the panels on the right are for the maximum. The area and orientation of the two source geometries are compared in relation to each other next to the parameter list at the top of the figure. For each area, four outputs are presented at different times after the eruption start $t_0$: **(a & e)** 7 h, **(b & f)** 13 h, **(c & g)** 18 h, and **(d & h)** 23 h. Total column mass loadings are averaged over the previous hour, and we applied a threshold of 0.2 g m$^{-2}$.

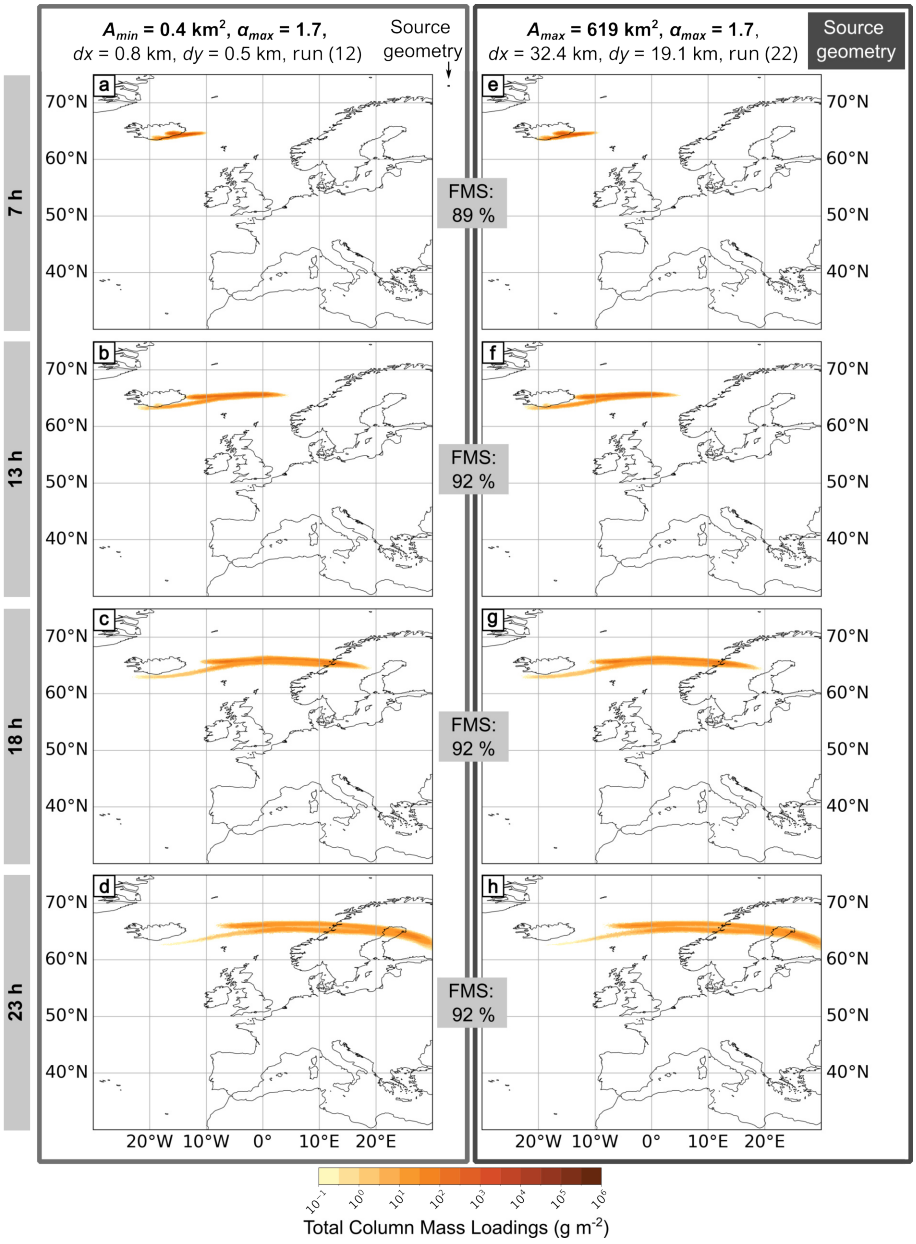


**Fig. S44**: Weather pattern 6. NAME outputs for numerical experiment 1, all using $\alpha_{max} = 1.7$, a 1 h particle release, $z = 8.5$ km, $dz = 3$ km and MER $= 1.06 \times 10^{13}$ g h$^{-1}$. The panels on the left are for the minimum source area, and the panels on the right are for the maximum. The area and orientation of the two source geometries are compared in relation to each other next to the parameter list at the top of the figure. For each area, four outputs are presented at different times after the eruption start $t_0$: **(a & e)** 7 h, **(b & f)** 13 h, **(c & g)** 18 h, and **(d & h)** 23 h. Total column mass loadings are averaged over the previous hour, and we applied a threshold of 0.2 g m$^{-2}$.

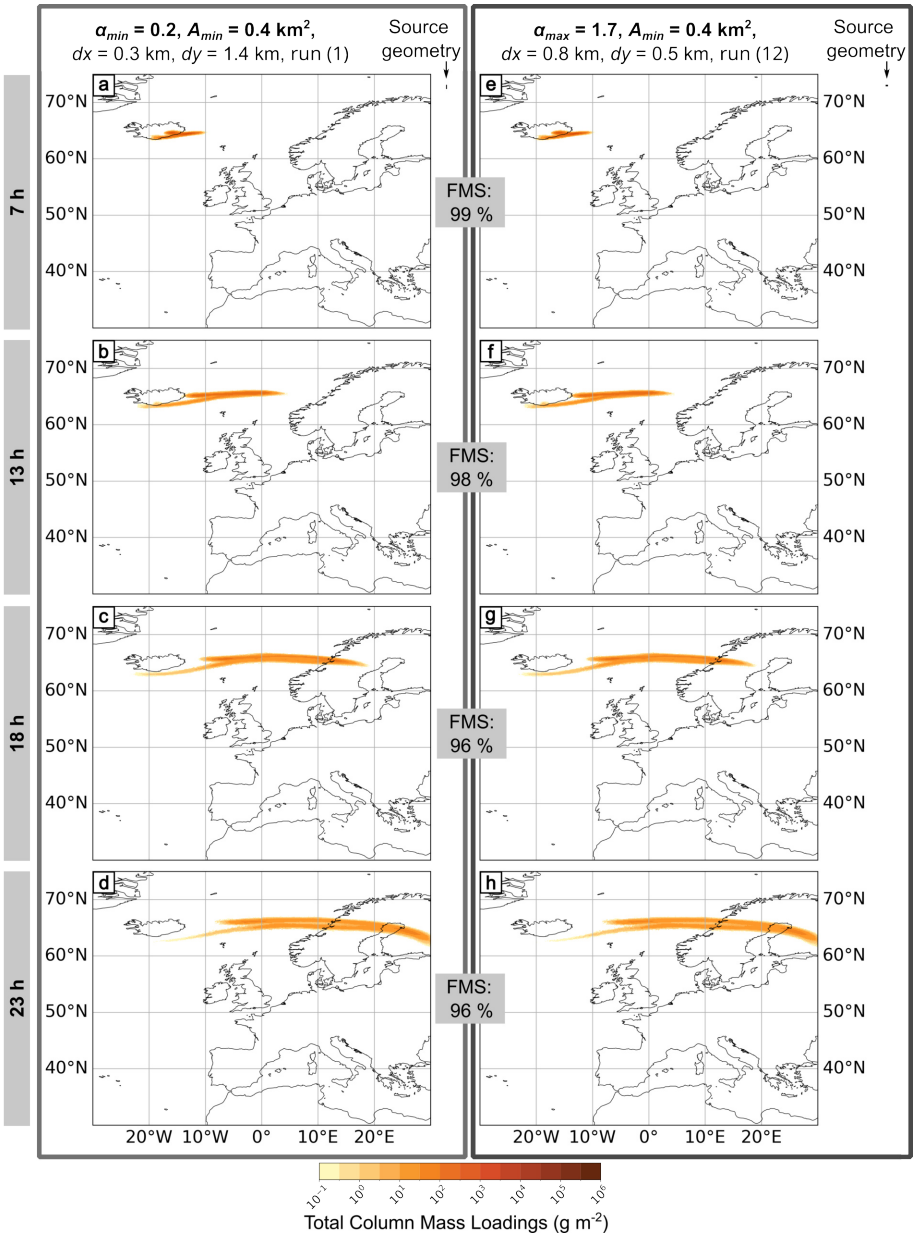


**Fig. S45**: Weather pattern 6. NAME model outputs for numerical experiment 1, all using $A_{min} = 0.4\,\mathrm{km}^2$, a 1 h particle release, $z = 8.5\,\mathrm{km}$, $dz = 3\,\mathrm{km}$ and MER $= 1.06 \times 10^{13}\,\mathrm{g\,h}^{-1}$. The left figure panels **(a-d)** show results from the minimum aspect ratio $\alpha_{min} = 0.2$, and the right panels **(e-h)** show the maximum aspect ratio $\alpha_{max} = 1.7$. The area and orientation of the two source geometries are compared in relation to each other next to the parameter list at the top of the figure. For each aspect ratio, four outputs at different times after eruption start $t_0$ are shown: **(a & e)** 7 h, **(b & f)** 13 h, **(c & g)** 18 h, and **(d & h)** 23 h. Total column mass loadings are averaged over the previous hour, and we applied a threshold of $0.2\,\mathrm{g\,m}^{-2}$.

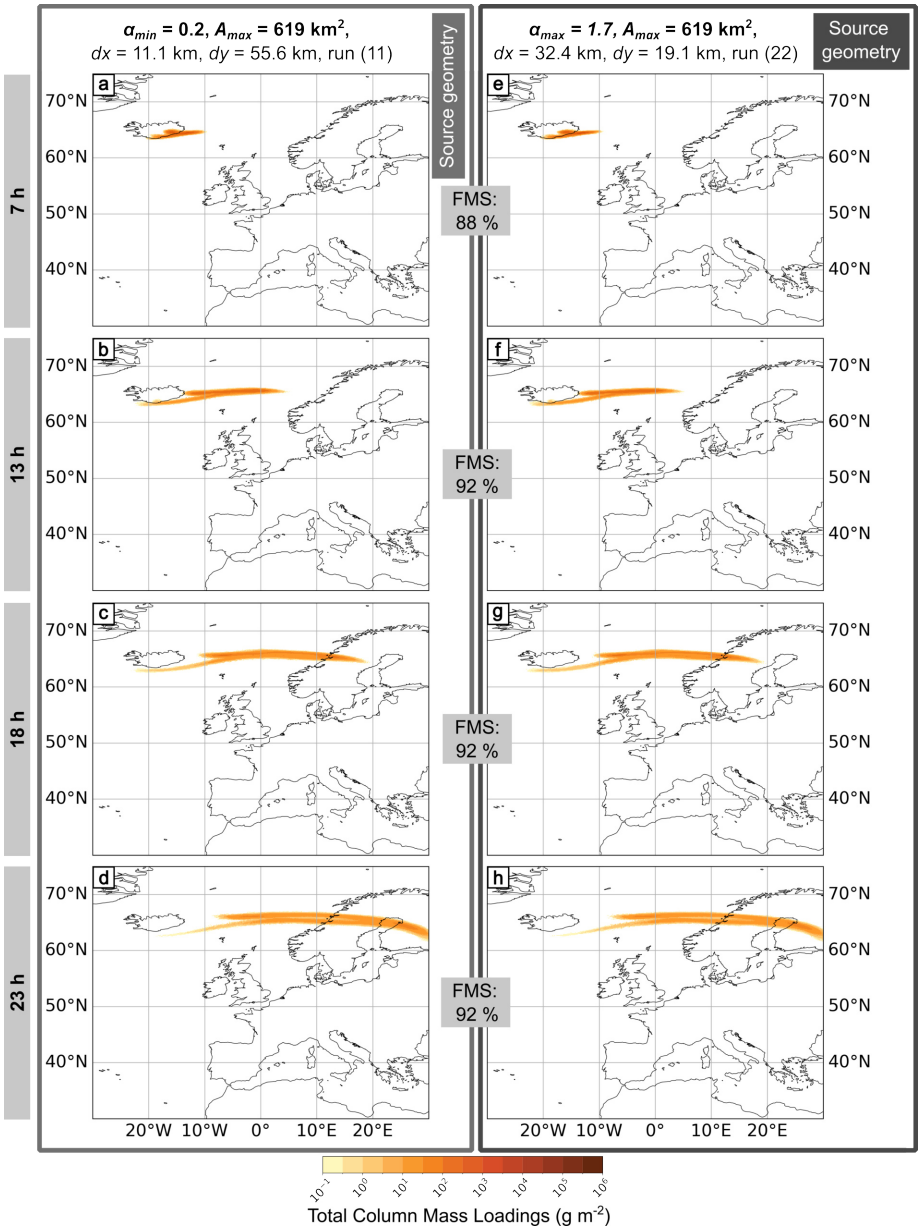


**Fig. S46**: Weather pattern 6. NAME model outputs for numerical experiment 1, all using $A_{max} = 619\,\mathrm{km}^2$, a 1 h particle release, $z = 8.5\,\mathrm{km}$, $dz = 3\,\mathrm{km}$ and MER $= 1.06 \times 10^{13}\,\mathrm{g\,h^{-1}}$. The left figure panels **(a-d)** show results from the minimum aspect ratio $\alpha_{min} = 0.2$, and the right panels **(e-h)** show the maximum aspect ratio $\alpha_{max} = 1.7$. The area and orientation of the two source geometries are compared in relation to each other next to the parameter list at the top of the figure. For each aspect ratio, four outputs at different times after eruption start $t_0$ are shown: **(a & e)** 7 h, **(b & f)** 13 h, **(c & g)** 18 h, and **(d & h)** 23 h. Total column mass loadings are averaged over the previous hour, and we applied a threshold of $0.2\,\mathrm{g\,m^{-2}}$.

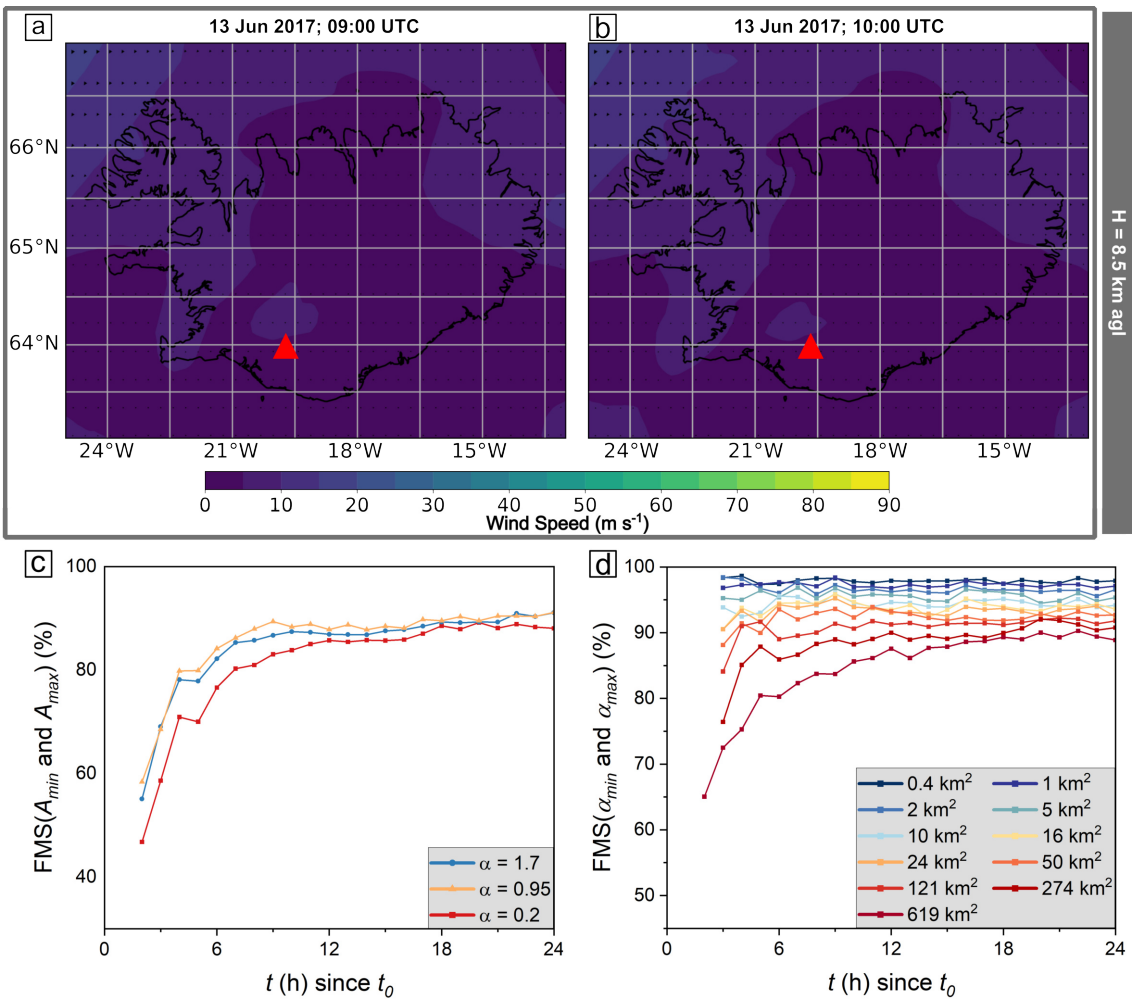


**Fig. S47**: Meteorological data for Iceland for weather pattern 7 at 8.5 km agl elevation at times **(a)** 09:00 UTC and **(b)** 10:00 UTC. The Figure of Merit in space (FMS) determined by Equation 9, shown **(c)** between the plumes generated using the minimum ($A_{min}$) and maximum ($A_{max}$) source area and **(d)** between the minimum ($\alpha_{min}$) and maximum ($\alpha_{max}$) aspect ratio.

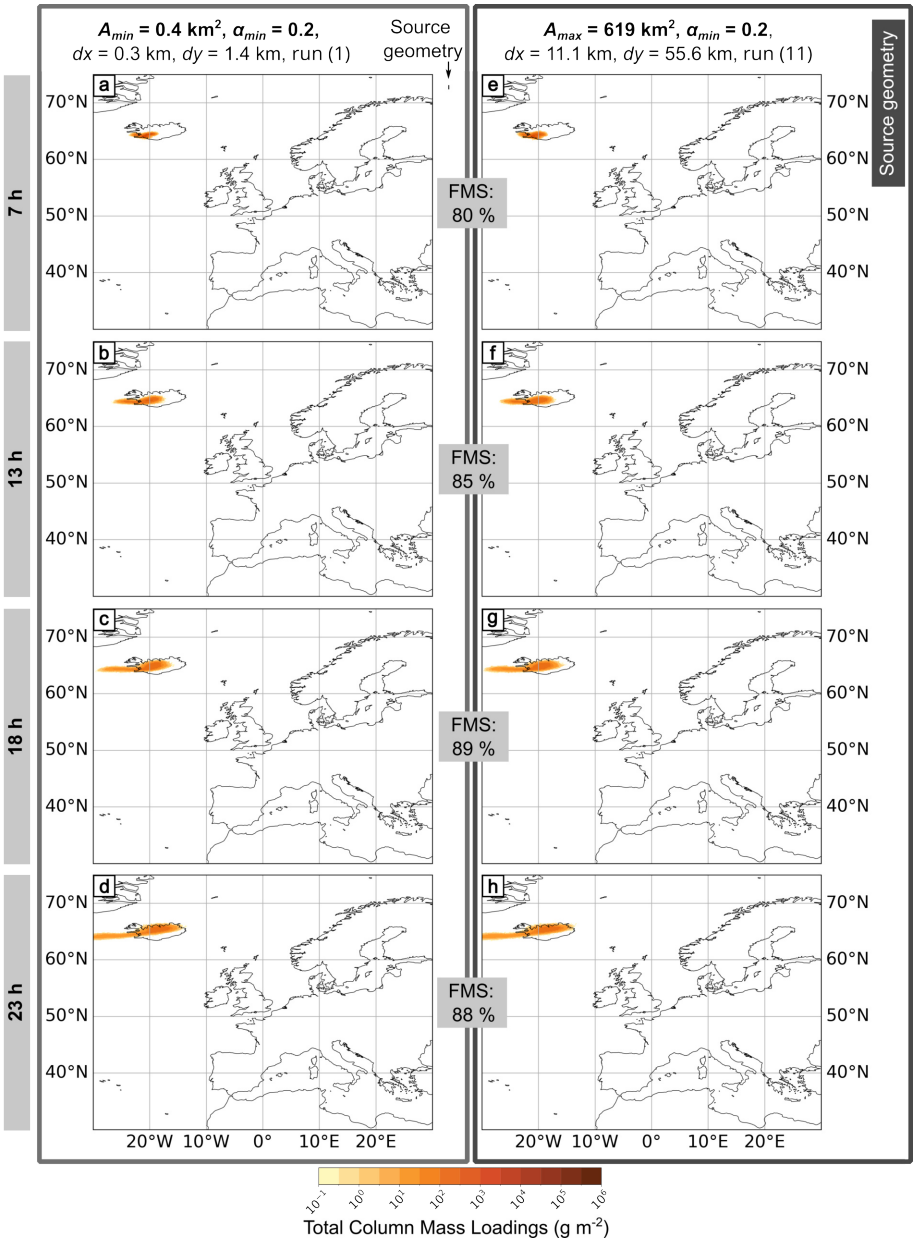


**Fig. S48**: Weather pattern 7. NAME outputs for numerical experiment 1, all using $\alpha_{min} = 0.2$, a 1 h particle release, $z = 8.5$ km, $dz = 3$ km and MER $= 1.06 \times 10^{13}$ g h$^{-1}$. The panels on the left are for the minimum source area, and the panels on the right are for the maximum. The area and orientation of the two source geometries are compared in relation to each other next to the parameter list at the top of the figure. For each area, four outputs are presented at different times after the eruption start $t_0$: **(a & e)** 7 h, **(b & f)** 13 h, **(c & g)** 18 h, and **(d & h)** 23 h. Total column mass loadings are averaged over the previous hour, and we applied a threshold of 0.2 g m$^{-2}$.

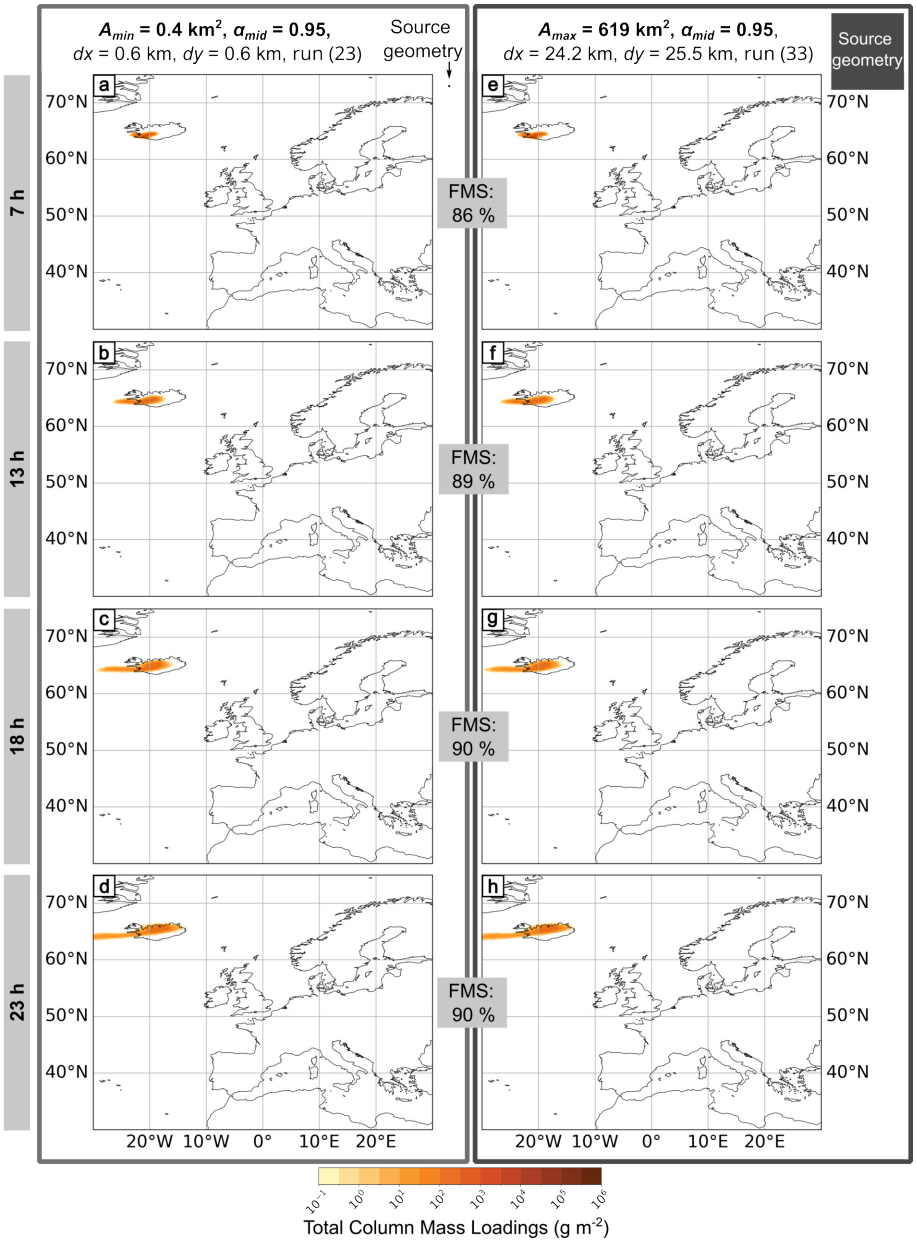


**Fig. S49**: Weather pattern 7. NAME outputs for numerical experiment 1, all using $\alpha_{mid} = 0.95$, a 1 h particle release, $z = 8.5$ km, $dz = 3$ km and MER $= 1.06 \times 10^{13}$ g h$^{-1}$. The panels on the left are for the minimum source area, and the panels on the right are for the maximum. The area and orientation of the two source geometries are compared in relation to each other next to the parameter list at the top of the figure. For each area, four outputs are presented at different times after the eruption start $t_0$: **(a & e)** 7 h, **(b & f)** 13 h, **(c & g)** 18 h, and **(d & h)** 23 h. Total column mass loadings are averaged over the previous hour, and we applied a threshold of 0.2 g m$^{-2}$.

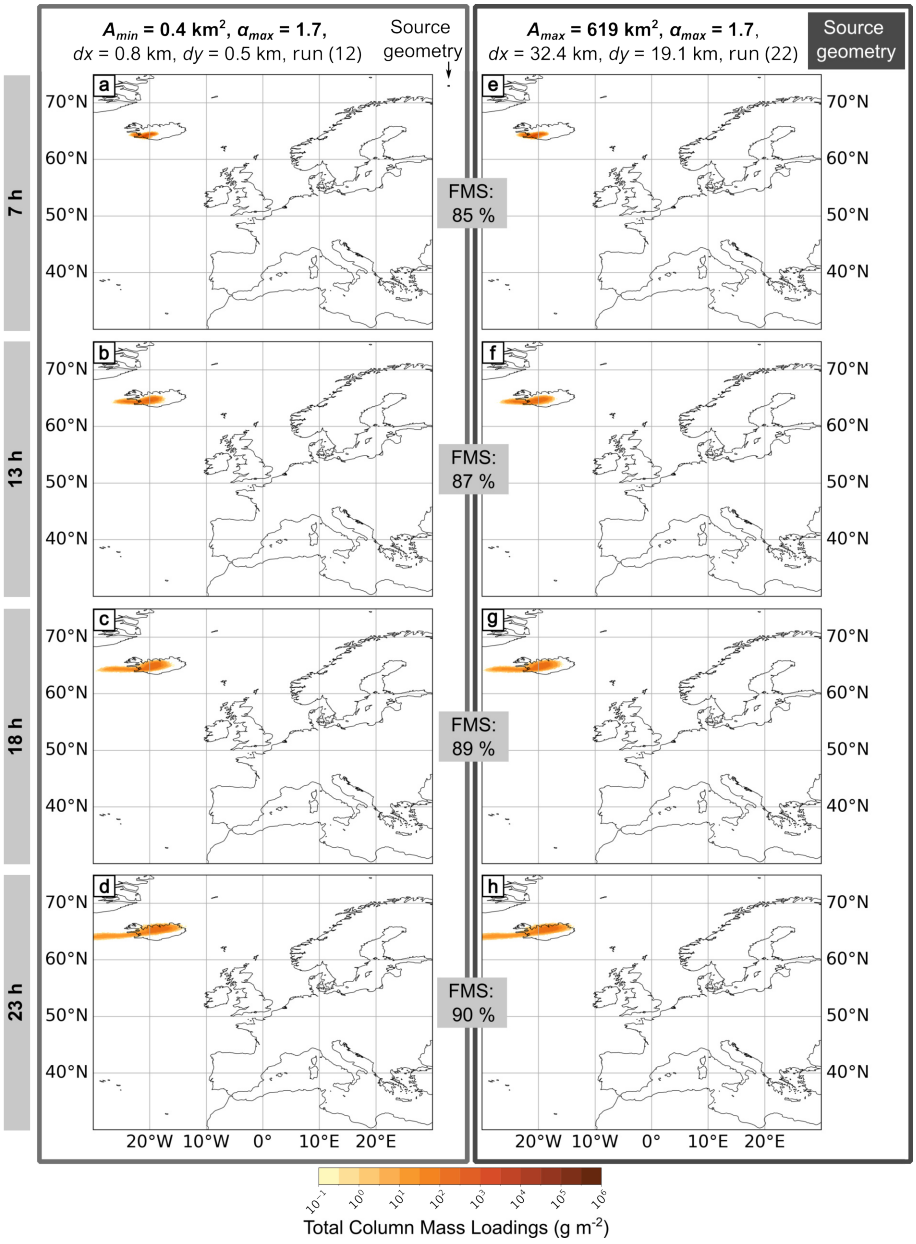


**Fig. S50**: Weather pattern 7. NAME outputs for numerical experiment 1, all using $\alpha_{max} = 1.7$, a 1 h particle release, $z = 8.5$ km, $dz = 3$ km and MER $= 1.06 \times 10^{13}$ g h$^{-1}$. The panels on the left are for the minimum source area, and the panels on the right are for the maximum. The area and orientation of the two source geometries are compared in relation to each other next to the parameter list at the top of the figure. For each area, four outputs are presented at different times after the eruption start $t_0$: **(a & e)** 7 h, **(b & f)** 13 h, **(c & g)** 18 h, and **(d & h)** 23 h. Total column mass loadings are averaged over the previous hour, and we applied a threshold of 0.2 g m$^{-2}$.

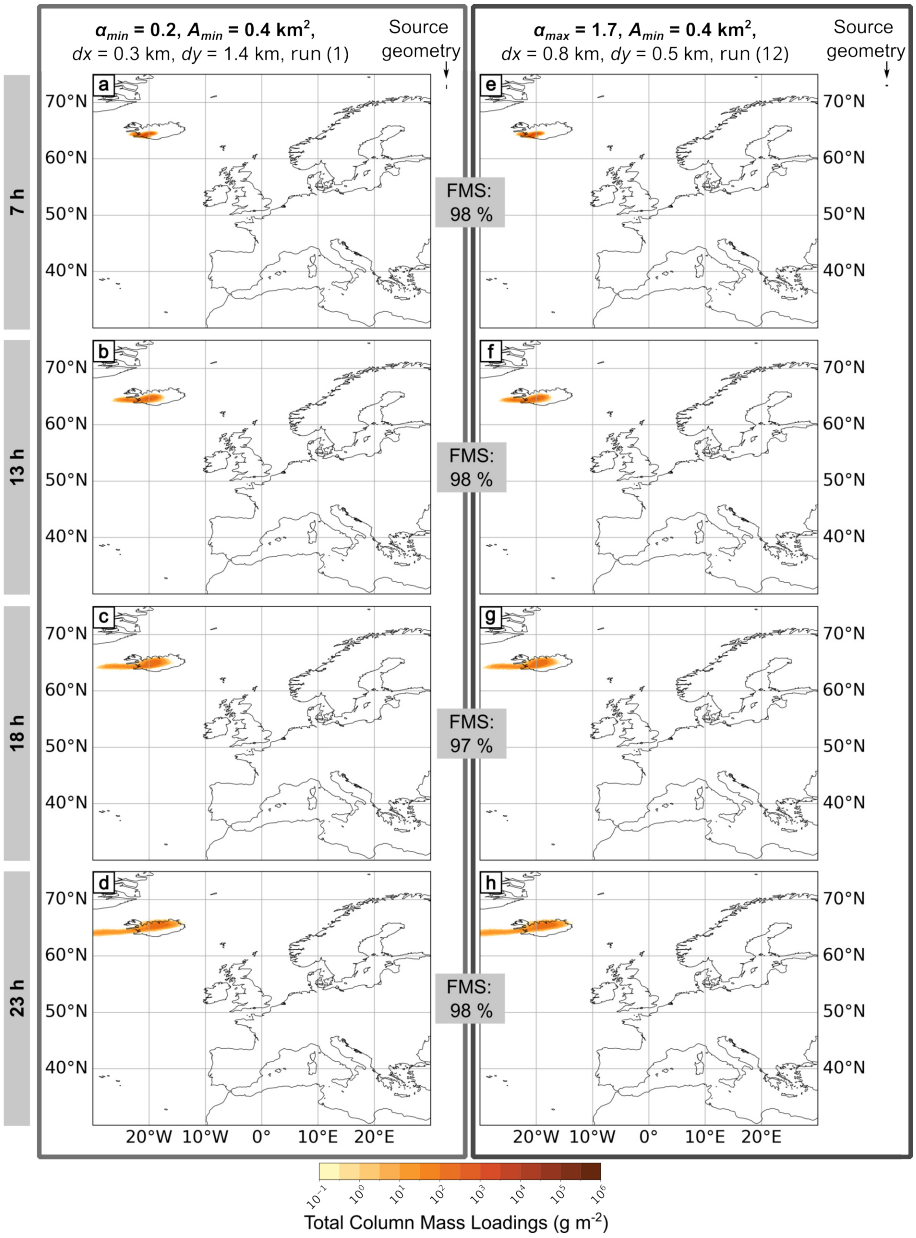


**Fig. S51**: Weather pattern 7. NAME model outputs for numerical experiment 1, all using $A_{min} = 0.4\,\mathrm{km}^2$, a 1 h particle release, $z = 8.5\,\mathrm{km}$, $dz = 3\,\mathrm{km}$ and MER $= 1.06 \times 10^{13}\,\mathrm{g\,h^{-1}}$. The left figure panels **(a-d)** show results from the minimum aspect ratio $\alpha_{min} = 0.2$, and the right panels **(e-h)** show the maximum aspect ratio $\alpha_{max} = 1.7$. The area and orientation of the two source geometries are compared in relation to each other next to the parameter list at the top of the figure. For each aspect ratio, four outputs at different times after eruption start $t_0$ are shown: **(a & e)** 7 h, **(b & f)** 13 h, **(c & g)** 18 h, and **(d & h)** 23 h. Total column mass loadings are averaged over the previous hour, and we applied a threshold of $0.2\,\mathrm{g\,m^{-2}}$.

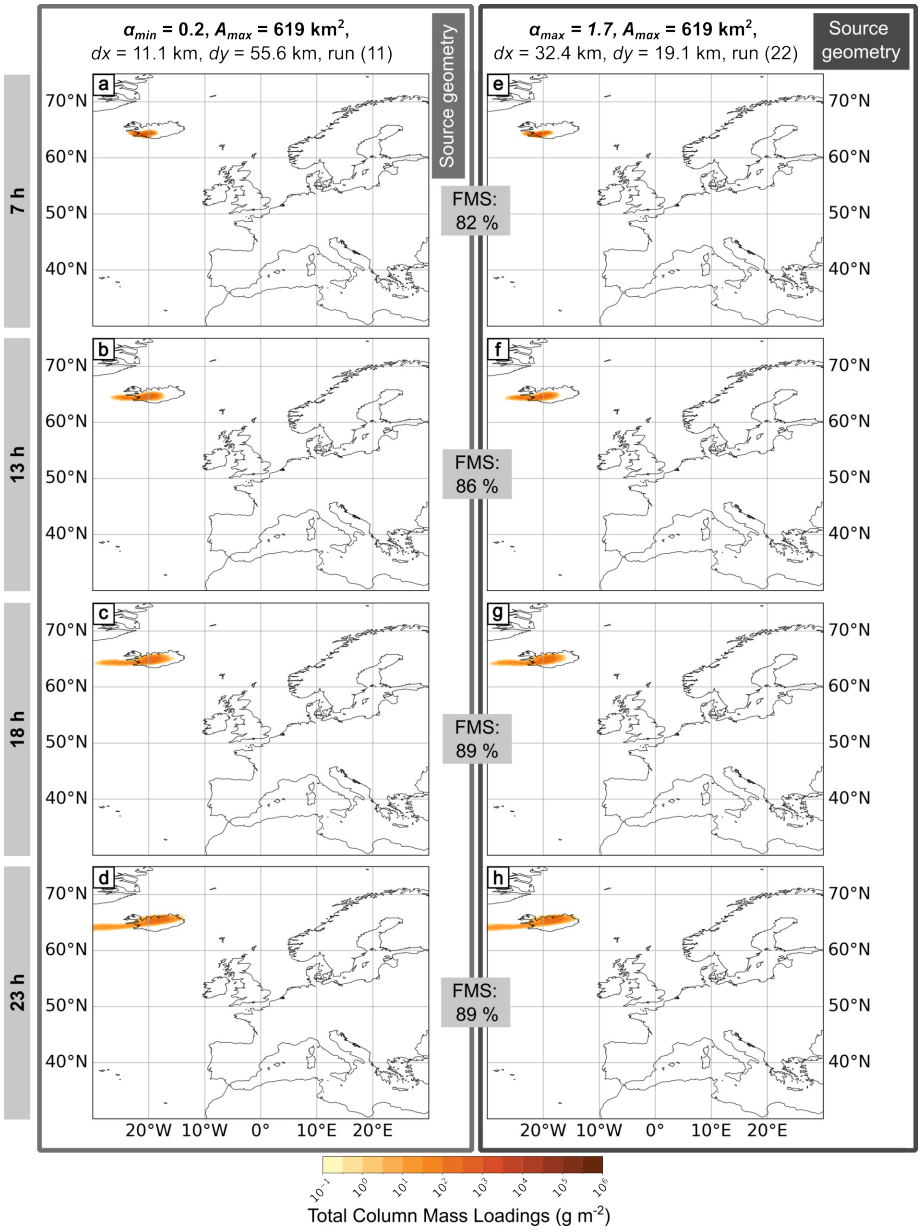


**Fig. S52**: Weather pattern 7. NAME model outputs for numerical experiment 1, all using $A_{max} = 619\,\mathrm{km}^2$, a 1 h particle release, $z = 8.5\,\mathrm{km}$, $dz = 3\,\mathrm{km}$ and MER $= 1.06 \times 10^{13}\,\mathrm{g\,h^{-1}}$. The left figure panels **(a-d)** show results from the minimum aspect ratio $\alpha_{min} = 0.2$, and the right panels **(e-h)** show the maximum aspect ratio $\alpha_{max} = 1.7$. The area and orientation of the two source geometries are compared in relation to each other next to the parameter list at the top of the figure. For each aspect ratio, four outputs at different times after eruption start $t_0$ are shown: **(a & e)** 7 h, **(b & f)** 13 h, **(c & g)** 18 h, and **(d & h)** 23 h. Total column mass loadings are averaged over the previous hour, and we applied a threshold of $0.2\,\mathrm{g\,m^{-2}}$.

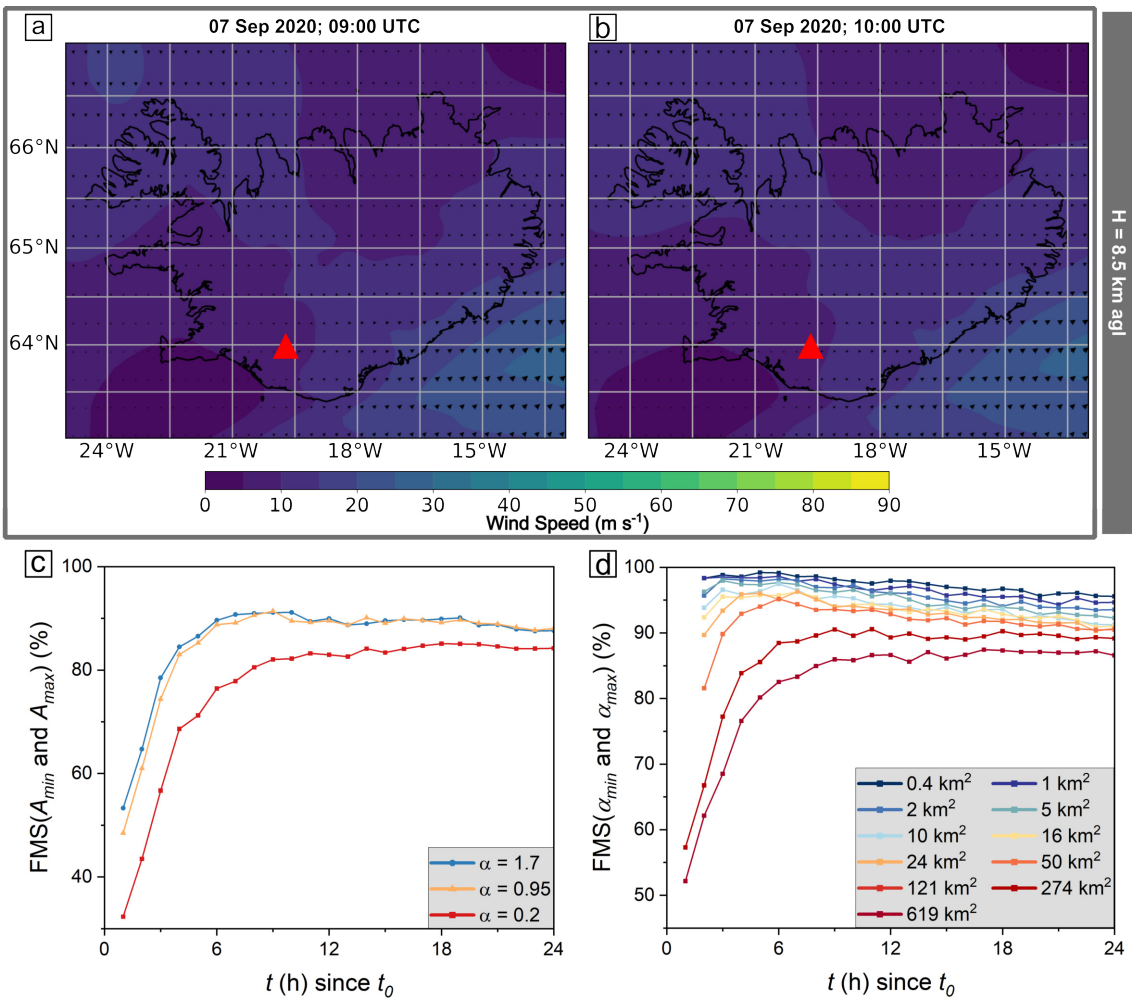


**Fig. S53**: Meteorological data for Iceland for weather pattern 8 at 8.5 km agl elevation at times **(a)** 09:00 UTC and **(b)** 10:00 UTC. The Figure of Merit in space (FMS) determined by Equation 9, shown **(c)** between the plumes generated using the minimum ($A_{min}$) and maximum ($A_{max}$) source area and **(d)** between the minimum ($\alpha_{min}$) and maximum ($\alpha_{max}$) aspect ratio.

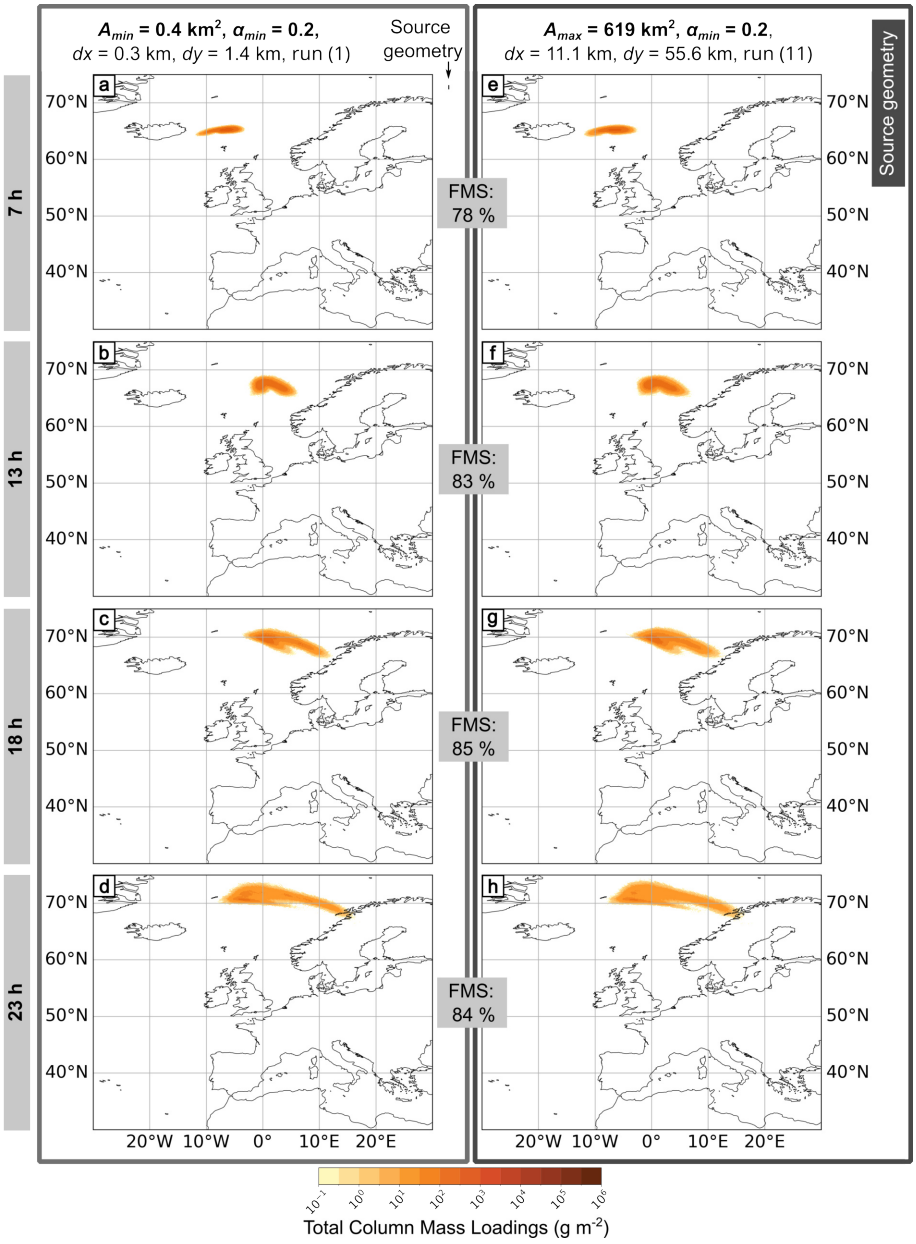


**Fig. S54**: Weather pattern 8. NAME outputs for numerical experiment 1, all using $\alpha_{min} = 0.2$, a 1 h particle release, $z = 8.5$ km, $dz = 3$ km and MER $= 1.06 \times 10^{13}$ g h$^{-1}$. The panels on the left are for the minimum source area, and the panels on the right are for the maximum. The area and orientation of the two source geometries are compared in relation to each other next to the parameter list at the top of the figure. For each area, four outputs are presented at different times after the eruption start $t_0$: **(a & e)** 7 h, **(b & f)** 13 h, **(c & g)** 18 h, and **(d & h)** 23 h. Total column mass loadings are averaged over the previous hour, and we applied a threshold of 0.2 g m$^{-2}$.

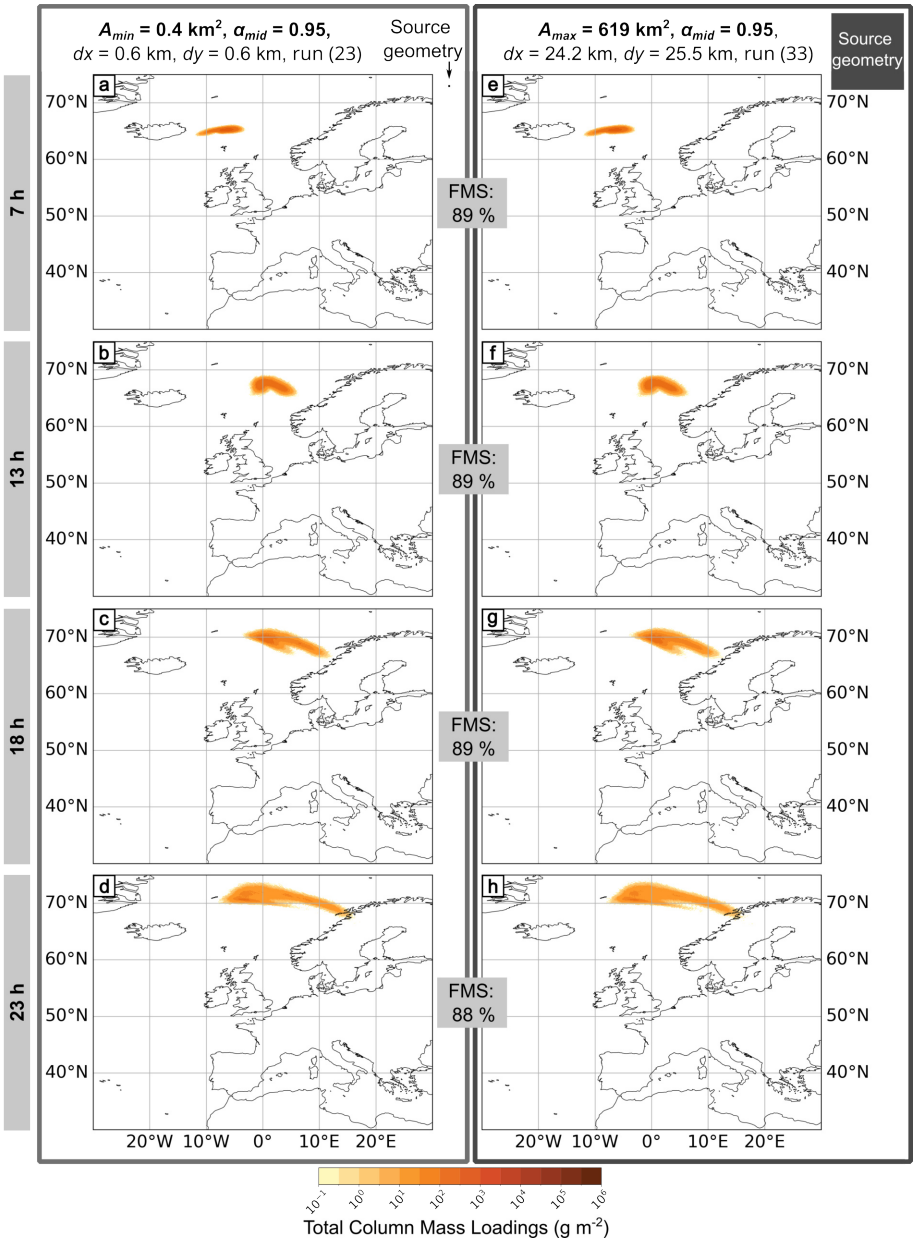


**Fig. S55**: Weather pattern 8. NAME outputs for numerical experiment 1, all using $\alpha_{mid} = 0.95$, a 1 h particle release, $z = 8.5$ km, $dz = 3$ km and MER $= 1.06 \times 10^{13}$ g h$^{-1}$. The panels on the left are for the minimum source area, and the panels on the right are for the maximum. The area and orientation of the two source geometries are compared in relation to each other next to the parameter list at the top of the figure. For each area, four outputs are presented at different times after the eruption start $t_0$: **(a & e)** 7 h, **(b & f)** 13 h, **(c & g)** 18 h, and **(d & h)** 23 h. Total column mass loadings are averaged over the previous hour, and we applied a threshold of 0.2 g m$^{-2}$.

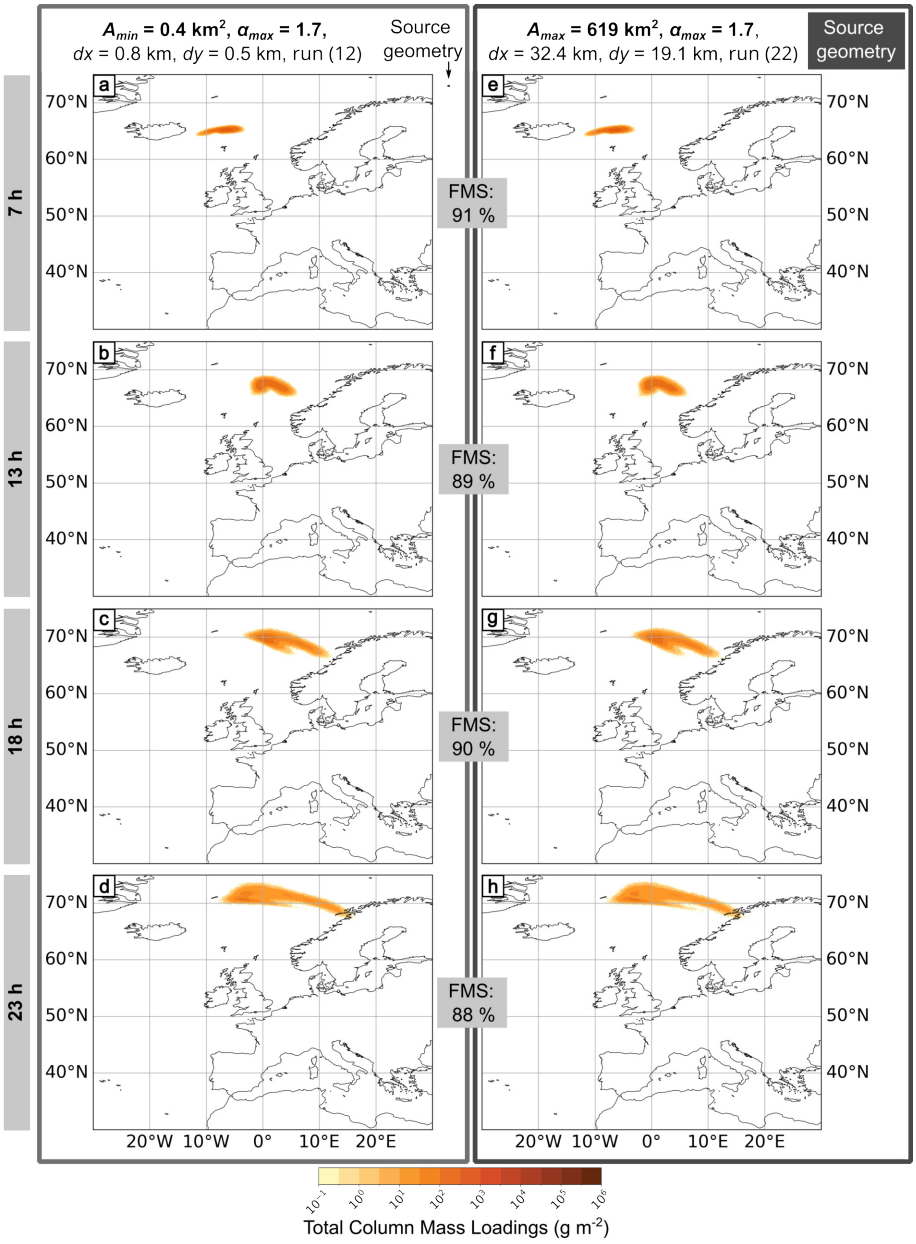


**Fig. S56**: Weather pattern 8. NAME outputs for numerical experiment 1, all using $\alpha_{max} = 1.7$, a 1 h particle release, $z = 8.5$ km, $dz = 3$ km and MER $= 1.06 \times 10^{13}$ g h$^{-1}$. The panels on the left are for the minimum source area, and the panels on the right are for the maximum. The area and orientation of the two source geometries are compared in relation to each other next to the parameter list at the top of the figure. For each area, four outputs are presented at different times after the eruption start $t_0$: **(a & e)** 7 h, **(b & f)** 13 h, **(c & g)** 18 h, and **(d & h)** 23 h. Total column mass loadings are averaged over the previous hour, and we applied a threshold of 0.2 g m$^{-2}$.

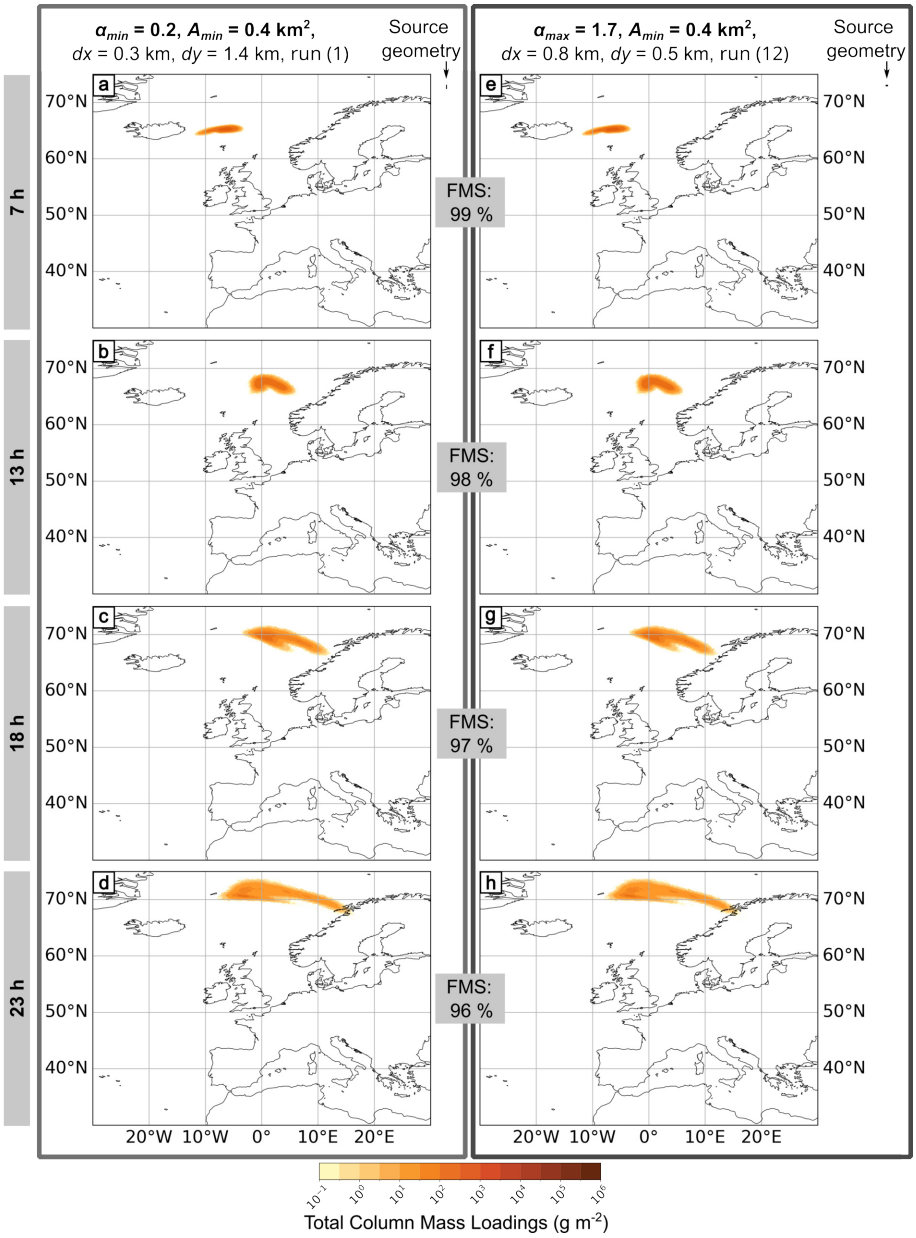


**Fig. S57**: Weather pattern 8. NAME model outputs for numerical experiment 1, all using $A_{min} = 0.4\,\mathrm{km}^2$, a 1 h particle release, $z = 8.5\,\mathrm{km}$, $dz = 3\,\mathrm{km}$ and MER $= 1.06 \times 10^{13}\,\mathrm{g\,h}^{-1}$. The left figure panels **(a-d)** show results from the minimum aspect ratio $\alpha_{min} = 0.2$, and the right panels **(e-h)** show the maximum aspect ratio $\alpha_{max} = 1.7$. The area and orientation of the two source geometries are compared in relation to each other next to the parameter list at the top of the figure. For each aspect ratio, four outputs at different times after eruption start $t_0$ are shown: **(a & e)** 7 h, **(b & f)** 13 h, **(c & g)** 18 h, and **(d & h)** 23 h. Total column mass loadings are averaged over the previous hour, and we applied a threshold of $0.2\,\mathrm{g\,m}^{-2}$.

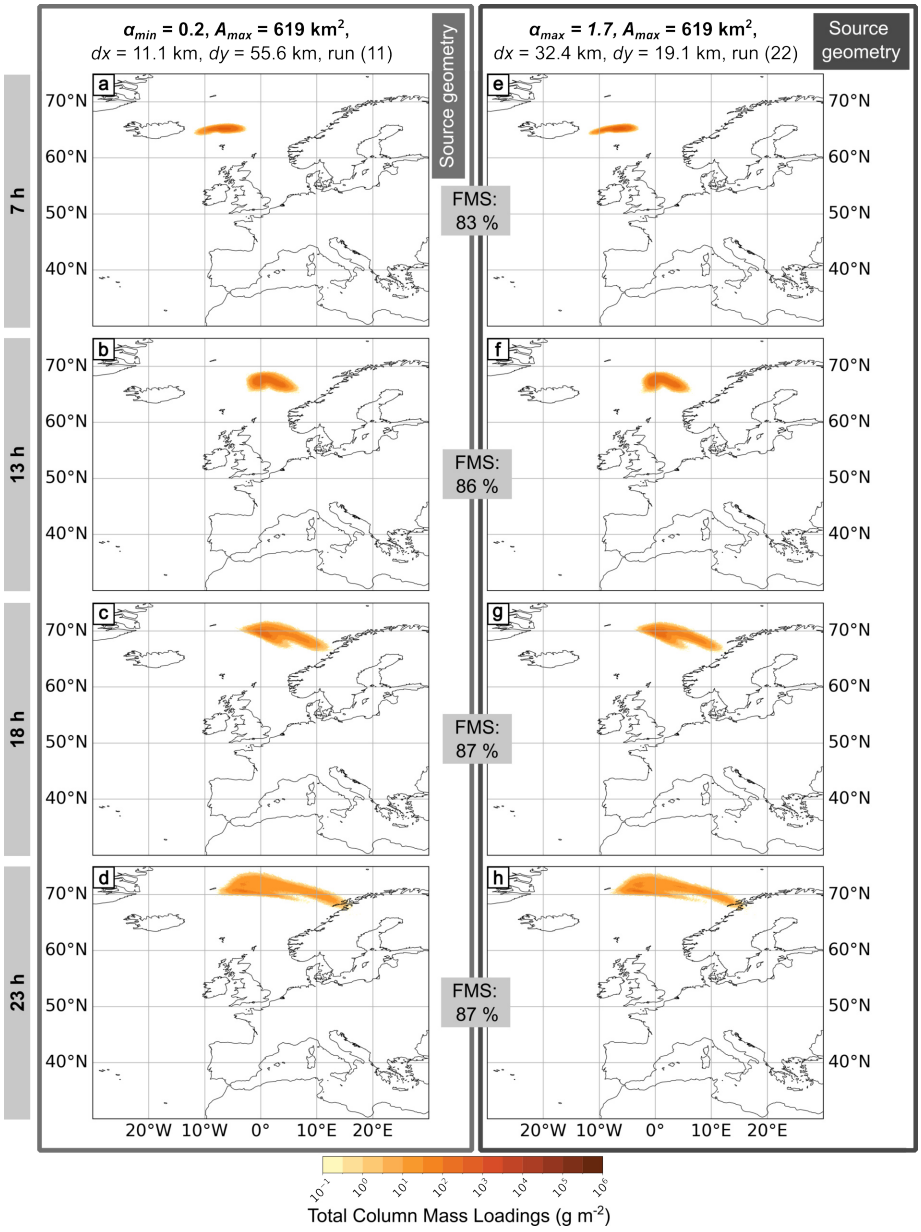


**Fig. S58**: Weather pattern 8. NAME model outputs for numerical experiment 1, all using $A_{max} = 619\,\mathrm{km}^2$, a 1 h particle release, $z = 8.5\,\mathrm{km}$, $dz = 3\,\mathrm{km}$ and MER $= 1.06 \times 10^{13}\,\mathrm{g\,h}^{-1}$. The left figure panels **(a-d)** show results from the minimum aspect ratio $\alpha_{min} = 0.2$, and the right panels **(e-h)** show the maximum aspect ratio $\alpha_{max} = 1.7$. The area and orientation of the two source geometries are compared in relation to each other next to the parameter list at the top of the figure. For each aspect ratio, four outputs at different times after eruption start $t_0$ are shown: **(a & e)** 7 h, **(b & f)** 13 h, **(c & g)** 18 h, and **(d & h)** 23 h. Total column mass loadings are averaged over the previous hour, and we applied a threshold of $0.2\,\mathrm{g\,m}^{-2}$.